AERODYNAMIC DESIGN AND CONTROL OF TANDEM WING UNMANNED AERIAL VEHICLE

A THESIS SUBMITTED TO
THE GRADUATE SCHOOL OF NATURAL AND APPLIED SCIENCES
OF
MIDDLE EAST TECHNICAL UNIVERSITY

BY

TAŞKIN KAYA

IN PARTIAL FULFILLMENT OF THE REQUIREMENTS
FOR
THE DEGREE OF MASTER OF SCIENCE
IN
AEROSPACE ENGINEERING

AUGUST 2019

Approval of the thesis:

AERODYNAMIC DESIGN AND CONTROL OF TANDEM WING UNMANNED AERIAL VEHICLE

submitted by **TAŞKIN KAYA** in partial fulfillment of the requirements for the degree of **Master of Science in Aerospace Engineering Department, Middle East Technical University** by,

Prof. Dr. Halil Kalıpçılar
Dean, Graduate School of **Natural and Applied Sciences**

Prof. Dr. İsmail Hakkı Tuncer
Head of Department, **Aerospace Engineering**

Prof. Dr. Serkan Özgen
Supervisor, **Aerospace Engineering, METU**

Examining Committee Members:

Prof. Dr. Yavuz Yaman
Aerospace Engineering, METU

Prof. Dr. Serkan Özgen
Aerospace Engineering, METU

Prof. Dr. Nafiz Alemdaroğlu
School of Civil Aviation, Atılım University

Assoc. Prof. Dr. Utku Kanoğlu
Aerospace Engineering, METU

Assist. Prof. Dr. Ali Türker Kutay
Aerospace Engineering, METU

Date: 02.08.2019

I hereby declare that all information in this document has been obtained and presented in accordance with academic rules and ethical conduct. I also declare that, as required by these rules and conduct, I have fully cited and referenced all material and results that are not original to this work.

Name, Surname: Taşkın Kaya

Signature:

ABSTRACT

AERODYNAMIC DESIGN AND CONTROL OF TANDEM WING UNMANNED AERIAL VEHICLE

Kaya, Taşkın
Master of Science, Aerospace Engineering
Supervisor: Prof. Dr. Serkan Özgen

August 2019, 118 pages

This thesis presents an approach towards the design methodology of electrical propulsion, tandem wing unmanned aerial vehicle. Due to its possible rewarding features, tandem wing design is investigated as the main subject of this study. The stability and control characteristics of tandem wing aircraft are critical since the interference between the two wings may result in nonlinear aerodynamic characteristics for varying angles of attack. Thus, the design of the controller system requires careful handling, in other words, linear aerodynamics envelope is a relatively constrained region for linear autopilot design. Nondimensional aerodynamic coefficients are determined for various angles of attack and flight speeds with CFD analysis using ANSYS Fluent software. Several airframe configurations are analyzed with CFD in consideration with the slotted wing effect. The airframe configuration with the most suitable aerodynamic characteristics is selected based on the CFD results. Three degrees of freedom flight simulation, which involves nonlinear aerodynamics, is used to test the performance of the attitude hold, acceleration and altitude hold autopilots for the selected tandem design. Finally, uncertainties and biases are randomly assigned and modeled with Monte-Carlo analysis to test the robustness of the autopilot and whether designed controllers are still capable of fulfilling mission requirements. Altogether, this study is a comprehensive one, which incorporates conceptual design, aerodynamic design and autopilot design phases of the tandem wing UAV.

Keywords: Tandem Wing, UAV Conceptual Design, Slotted Wing Effect, Attitude Hold, Altitude Hold, Flight Simulation, Monte Carlo Analysis

ÖZ

TANDEM KANAT İNSANSIZ HAVA ARACININ AERODİNAMİK TASARIMI VE KONTROLÜ

Kaya, Taşkın
Yüksek Lisans, Havacılık ve Uzay Mühendisliği
Tez Danışmanı: Prof. Dr. Serkan Özgen

Ağustos 2019, 118 sayfa

Bu tez elektrik itki sistemine sahip tandem kanatlı bir insansız hava aracı için sistematik bir tasarım yaklaşımı sunmaktadır. Muhtemel faydalı olabilecek özellikleri sebebiyle tandem kanat tasarımı bu tezin ana konusu olarak seçilmiştir. İki kanat arasındaki etkileşimden dolayı tandem kanatlı bir uçağın kararlılık ve kontrol özellikleri kritiktir, çünkü; bu etkileşim yüksek ölçüde doğrusal olmayan bir aerodinamik karakteristiğe sebep olabilmektedir. Bu sebeple, kontrolcü tasarımı dikkatle yapılmalıdır, diğer bir deyişle, doğrusal otopilot tasarımına girdi olan doğrusal aerodinamik zarf göreceli olarak daha kısıtlı bir bölgedir. Boyutsuz aerodinamik parametreler, değişen uçuş hızları ve hucüm açıları için HAD analizleriyle ANSYS Fluent yazılımı kullanılarak elde edilmektedir. Çeşitli uçak konfigürasyonları oluklu kanat etkisi göz önününde bulundurularak HAD ile analiz edilmektedir. En uygun aerodinamik konfigürasyona sahip uçak HAD sonuçları baz alınarak seçilmektedir. Doğrusal olmayan aerodinamik veritabanını içeren, 3 serbestlik dereceli uçuş simülasyonu, yunuslama açısı, ivme ve irtifa tutma kontrolcülerini test etmek için kullanılmaktadır. Son olarak, bazı belirsizlik ve yanlılık değerleri rassal olarak atanarak tasarlanan kontrolcülerin gürbüzlüğü test edilmekte ve bu kontrolcülerin görev gereksinimlerini yerine getirip getiremediği görülmektedir.

Bütünüyle, kavramsal tasarım, aerodinamik tasarım ve kontrolcü tasarımını bir araya getiren bu tez, kapsamlı bir çalışma sunmaktadır.

To people who ever taught me

ACKNOWLEDGEMENTS

I would like to express my gratitude to my supervisor, Prof. Dr. Serkan Özgen, for his expertise and guidance throughout my study. It would have been impossible for me to find my way through the complicated work, without his mentoring.

I am also thankful to my colleagues, especially, Erkut Başkut and Haydar Tolga Avcıoğlu in ROKETSAN Missile Industries Inc. for their understanding and support.

I am grateful to my parents, and also my brother Aşkın, for their endless love and support. They have always been there for me. I took their love and good wishes for granted under all circumstances.

For her kind embracement, for her understanding, and for the inspiration she granted; I am grateful to my love, Sema.

TABLE OF CONTENTS

LIST OF TABLES

TABLES

LIST OF FIGURES

FIGURES

LIST OF SYMBOLS

SYMBOLS

$a_x,\ a_y,\ a_z$	body coordinate axis translational accelerations
AR	wing aspect ratio
b	wing span
c_{mean}	mean aerodynamic chord
$C_X,\ C_Y,\ C_Z$	body coordinate axis non-dimensional force coefficients
$C_l,\ C_m,\ C_n$	body coordinate axis non-dimensional moment coefficients
$C_L,\ C_D$	wind coordinate axis non-dimensional force coefficients
C_f	skin friction coefficient
e	Oswald span efficiency
I_y	mass moment of inertia about longitudinal plane
K	induced drag coefficient
$p,\ q,\ r$	body coordinate axis angular rates (roll, pitch, yaw)
$P_R,\ T_R$	power and thrust required
q_∞	freestream dynamic pressure
ROC	rate of climb
Re	Reynolds number
S	reference area

S_{HT}	horizontal tail volume coefficient
$u,\ v,\ w$	body coordinate axis velocities
V_{∞}	freestream air velocity
W_x	weight of a specific component
y^+	non dimensional distance
α	angle of attack
ω_n	natural frequency
ε	thrust inclination angle
$\phi,\ \theta,\ \psi$	Euler angles
ρ	air density
$\eta_{pr},\ \eta_{mtr}$	efficiency of propeller, efficiency of electric motor
μ	dynamic viscosity
σ	density ratio
μ_T	friction velocity
τ_w	shear wall stress
ξ	damping ratio
δ	control actuator system position deflection

CHAPTER 1

INTRODUCTION

1.1. Background

An unmanned aerial vehicle (UAV) refers to a type of aircraft that flies without a human pilot on board that it is either controlled remotely or flies autonomously having control algorithms and sensors onboard. Uses of UAV systems are expanding in both military and civil applications including reconnaissance, surveillance, target acquisition, convoy support, battle damage assessment, environmental monitoring, agriculture, border patrol, search and rescue. Thanks to advances in microcontrollers, electromechanical components, and sensor technology, large (e.g., Predator, Harfang) and small UAVs (e.g., Raven, Desert Hawk, mini-Bayraktar) have emerged over past several years. On the other hand, many of the previously mentioned applications have not developed to maturity yet. Durability, reliability, ease of use and cost issues are still needed to be overcome (Beard & McLain, 2012).

Unmanned aerial vehicles utilize technologies such as complex airframe configurations for high aerodynamic efficiency, inertial measurement unit and/or GPS for navigation, electrical or fuel propulsion system, communication link, guidance computer, and payload. The aim of a UAV is to fly a payload. The most common types are fixed or gimballed EO/IR cameras and warheads for military operations (Barton, 2012). By a communication link between the ground control station and the UAV, a user can convey flight commands to shape the trajectory and receives flight data and video in turn.

1.2. Objective of the Thesis

This study addresses the domain of conceptual design of a micro UAV, investigating the aerodynamic design, stability and control system design and how these are related in the case of a tandem wing aircraft, in particular. The objective of the thesis is to verify whether the tandem wing understudy meets the requirements of surveillance and reconnaissance air vehicle (such as long endurance, low observability, etc.) and to investigate possible aerodynamic advantages and disadvantages.

Both wings of the tandem layout contribute to the lift with a similar planform area but with a considerably reduced span compared to a monoplane wing configuration. The reason why tandem wing design is the focus of this work is that the airframe to be designed should fit into a launcher or a launch tube. Therefore, the wingspan is the geometric driving requirement that allows wings to be folded inside a tube before launch. Take-off from the launch tube also translates to a high lift requirement. This thesis searches for how the high lift generation is affected by tandem wings under the slotted wing effect. Furthermore, shorter span or wings also provide lower structural weight and moment of inertia which improves the turning performance and allows agile maneuvers. On the other hand, stability may constitute an issue in the tandem wing configuration since high or negative angle attack flight may result in highly nonlinear aerodynamic characteristics due to interference between the two wings. Thus, a computational fluid dynamics tool is used to seek for stability/control characteristics and the slotted wing effect of the tandem wing configuration.

After the reasons why it is worthwhile to investigate the tandem wing, the requirements of UAV are defined that drive the initial layout process. The process starts with defining the mission profile of the proposed UAV and searching the competitor aircraft from the literature. It is a multi-disciplinary process that incorporates several aspects including aerodynamics, electric propulsion system selection, control actuator system, inertial navigation, and control system design.

A typical micro UAV has batteries, motor, and propellers in the propulsion system. The propulsion system of a micro UAV accounts for as much as 60% of its weight (Gur & Rosen, 2009). Thus, the selection of the propulsion system is extremely important and it is one of the main subjects of this study.

The tandem wing design employs the rear wing act like a slotted-flap which may result in complex aerodynamics problems, thus, controller design becomes crucial and must be handled carefully. The interference between the front and rear wing is a potential problem with this configuration. Control surfaces are placed on the rear wing in tandem wing configuration in this study. Therefore, the downwash effect of the forward wing on the rear wing causes degration in control effectiveness or even instability due to the stall of the rear wing at specific angles of attack. An aerodynamic database for each alternative design candidate is obtained using a CFD tool ANSYS FLUENT for a range of angle of attack to investigate the wings in interference. The control system design is one of the most significant steps during the preliminary design phase of a UAV. The linear control system design methods (classical control, modern control methods) are constrained by the aerodynamic characteristics of the aircraft since the linear envelope is the region of interest for these design methods. The control system analysis in this research reveals the stability and flight performance characteristics.

Even though the system model may seem accurate and reliable at the end of the design process, it is also important to illustrate that this statement is still valid when atmospheric disturbances, uncertainties, and biases are present. The Monte-Carlo analysis is conducted by assigning those uncertainties randomly to see whether UAV can still fulfill the mission requirements.

1.3. Scope of the Thesis

Conceptual design process is divided into seven chapters. The methodology of design process is shown in Figure 1.1.

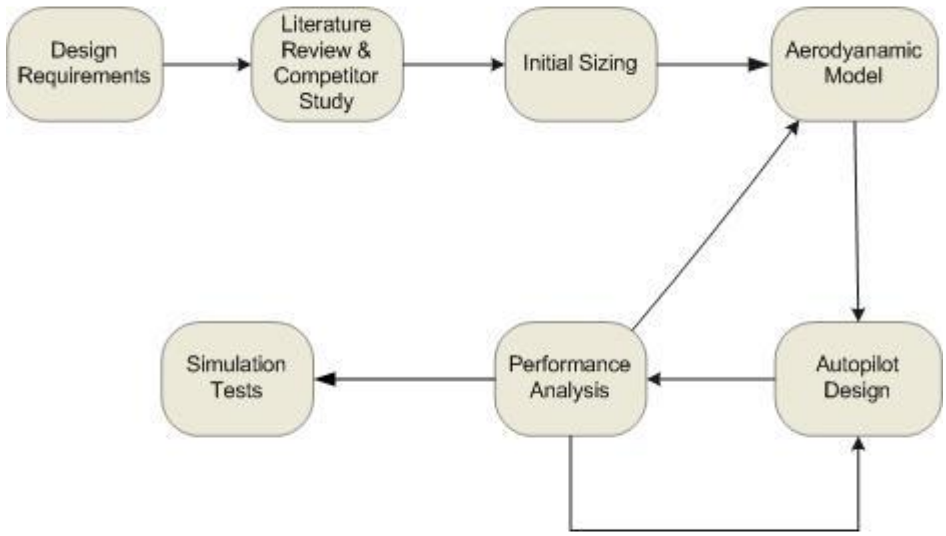

Figure 1.1. Methodology of conceptual design

In Chapter 2, mission and design requirements that drive the conceptual design phase are explained. The proposed geometric characteristics and performance parameters of the design are specified in this section. Based on the current applications of the unmanned systems, the following system requirements are also emphasized in detail; reliability, cost-effectiveness, autonomy, portability, and operational availability.

In Chapter 3, literature review and competitor UAVs are presented. The initial sizing process is described starting from the average weight assumption obtained from previous successful designs. The requirements and mission profile must be well defined to design a man-portable, lightweight, and cost-effective UAV. To begin with first take-off weight estimation; wing geometry sizing and initial performance parameters are determined. Besides, the propulsion system of the UAV is selected involving the combination of battery, electric motor, and propeller.

In Chapter 4, the aerodynamic model of the tandem wing UAV is analyzed with a CFD tool ANSYS Fluent. The aerodynamic model reveals the stability characteristics of aircraft. Before starting CFD analysis of tandem wing UAV, experimental data of 3D finite aspect ratio wing is compared with its CFD simulation results to select a suitable turbulence model for a low Reynolds number and to perform validation study for the CFD methodology applied. Another reason why the CFD analysis is performed is to observe the slotted wing effect on turbulence and stall characteristics in the tandem wing layout. At the end of this section, non-dimensional aerodynamic coefficients are obtained for a range of angle of attack, flight speed and control surface deflection for the final tandem design. If satisfactory stability and aerodynamic characteristics are achieved from CFD analysis, aerodynamic coefficients become the input to controller design.

In Chapter 5, the details of the autopilot design to perform mission requirements is presented. Firstly, the dynamic model of the UAV is generated. The attitude hold, acceleration, altitude hold, and speed control autopilots are designed as the main subjects of this chapter. Poles of the airframe and poles of the control actuator system are placed in a manner that desired performance characteristics are achieved. The robustness of the controller design is ensured considering frequency domain analysis. In the end, gain scheduled controller coefficients are embedded in 3 degrees of freedom flight simulation having a nonlinear aerodynamic database.

In Chapter 6, Monte-Carlo analysis is conducted. Random uncertainties, bias values, and environmental conditions are modeled in Monte-Carlo simulation to show that autopilot still satisfies mission requirements under disturbances.

In Chapter 7, general conclusions are made about the study. Besides, recommendations for future work are stated.

CHAPTER 2

DESIGN REQUIREMENTS

2.1. Overview

UAV system to be designed should fulfill the following:

- A low structural weight that allows the user to transport it anywhere for reconnaissance and surveillance missions
- Real-time operation, remote monitoring
- Operation at different user-defined altitudes
- Line of sight operations
- Low observability and low noise

2.2. Requirements

1. Takeoff weight < 5 kilograms
2. Maximum wing span < 1 meter
3. Endurance > 10 minutes
4. Range > 15 kilometers
5. Cruise speed > 25 m/s
6. Operating altitude = 150 meters (AGL)
7. Capability of flying with different payload (EO/IR camera, strap down camera or warhead)
8. Launch from a pneumatic tube

2.3. System Specifications

Based on the current applications of unmanned systems, each air vehicle should satisfy several requirements. Ideally, aircraft design is directed by specifications and requirements from the customer. In this research, system specifications are listed and explained in the following subsections (Torun, 1999).

2.3.1.1. Reliability

System reliability constitutes the maturity of both hardware and software for a UAV. Hardware insufficiencies and software bugs are expected during the development phase and have a direct impact on the final design. Since UAV systems carry significant data obtained during the mission and advanced, expensive subsystems, it is critical that they can perform various missions without any type of failure occurrence. Monte Carlo simulations or multiple batch runs that involve various flight scenarios are precautions to be taken to enhance the reliability of the aircraft.

2.3.2. Low Observability and Reduced Noise

It is essential that UAV’s reconnaissance mission is intended for low observability and quiet operations. In other words, designs must allow the mission to be completed in hostile territory without being detected. An electrical propulsion system is preferable since it provides both less noise and low thermal signature compared to an internal combustion engine.

2.3.3. Maintainability

Maintainability is a key of a UAV system to be retained in operation condition. It assures that there are no faults during the operation condition. Repairing defects instantly results in improved safety and efficiency of the UAV system.

2.3.4. Mobility

Mobility means that the system can be transported to any place in the mission field. Both UAV and the communication unit should be portable by the user. Furthermore, a minimal period of deployment is necessary, thus, air vehicle should also be assembled quickly.

2.3.5. Autonomy

The autonomous mission is performed with existing data-link onboard and ground control station. Data-link is two-way communication. Uplink conveys navigation inputs/flight path shaping and payload commands. Based on the navigation commands, UAV performs the mission without remote pilot control. Downlink transmits status data regarding UAV and the data from the payload, for instance, real-time imagery.

2.3.6. Performance

Tandem wing configuration is a multiple lifting surface design. This wing configuration is useful in the case when the wingspan is restricted and multiple wings are needed to generate lift. Thus, one purpose of this study is to investigate the performance advantages/disadvantages of multiple lifting surface concepts and to analyze whether the requirements of the mission are fulfilled. The typical mission profile of reconnaissance and surveillance UAV is shown in Figure 2.1. The ultimate aim of this type of UAV is to loiter around the target zone.

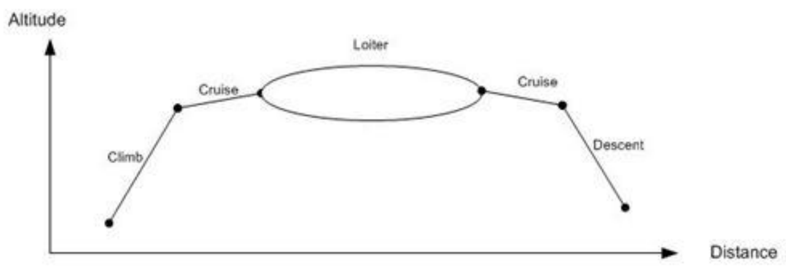

Figure 2.1 Classical mission profile of reconnaissance and surveillance UAV

CHAPTER 3

LITERATURE REVIEW & INITIAL SIZING

3.1. Literature Review

3.1.1. Background

The interest in UAV’s has dramatically increased over the past several decades until the present. They first emerged in the 1930s, especially in World War II thanks to the development of small internal combustion engines and radio transmitters/receivers. Even though UAV’s were originally motivated by military operations, the use of them has spread to civilian applications including agriculture, atmospheric/environmental events monitoring, and even firefighting due to improvements and availability of microelectronic sensors (Skrzypietz, 2012).

UAVs can be classified according to many criteria. Table 3.1 represents the five UAV categories defined by the Unmanned Air Vehicles-International based on several performance characteristics (Eisenbeiss, 2004). This thesis focuses on the class ‘Micro’; however, definitions of Micro and Mini classes are very similar.

Table 3.1 Classification by UAV’s International

Category name	**Mass [kg]**	**Range [km]**	**Flight Altitude [m]**	**Endurance [hours]**
Micro	<5	<10	250	1
Mini	<25	<10	150/250/300	<2
Close Range	25-150	10-30	3000	2-4
Medium Range	50-250	30-70	3000	3-6
High Altitude & Long Endurance	>250	>70	>3000	>6

Tandem wing configuration, as mentioned previously, can achieve a high lift force without flaps. This property is especially desired for UAVs with no landing gear that perform “belly-landing” and take-off at low speeds. Nevertheless, the tandem wing is not a new idea. Louis Peyret, a French engineer, designed a glider with almost identical wings in 1907. This design could be considered as the first successful tandem wing design since Peyret won the competition organized by Royal Aero Club with the pilot Alexis Maneyrol. After several flights and even breaking the record of the longest glide and the distance, a tragedy took place. Maneyrol got killed caused by broken wings when the Peyret Aircraft reached very high elevation (Slater, 1962).

Figure 3.1 Peyret Tandem Aircraft (no date, Retrieved from https://tr.pinterest.com)

Another enthusiast of the tandem wing design was George Miles. He designed and built the M 35 and carrier-borne aircraft in 1942 and later the M 39 to prove the advantages of tandem wings without support from the Ministry of Aircraft Production. The aircraft was unstable and the first flight was unsuccessful. He preferred to use different control surfaces on both wings; ailerons on the rear wing, elevators on the front wing, and rudders at the wingtips. However, Miles' aircrafts were not considered as satisfactory due to bad stall characteristics and downwash effects at the time (Brinkworh, 2016).

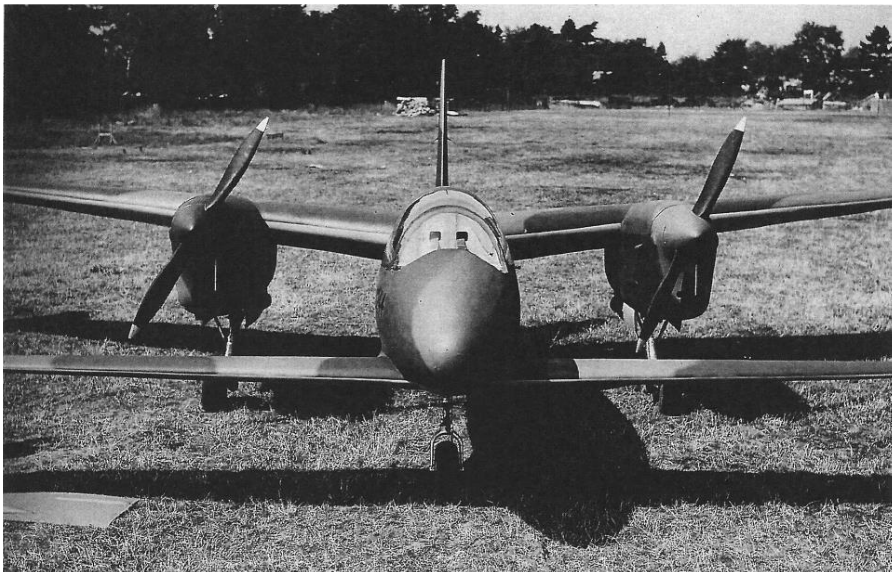

Figure 3.2 M39B Libellula on roll-out, (Brinkworh, 2016)

Tandem wing configuration has gained popularity again over the last two decades in modern warfare with numerous countries employing armed drones such as Switchblade and Orbiter UAV systems. As the UAV's are becoming more inexpensive and versatile, they are more likely to play a more crucial role in future uses.

3.1.2. Non Planar Wing Configurations

Tandem wing is a nonplanar wing configuration as other existing nonplanar concepts like a biplane, ring wing, and winglets. The reasons why unconventional, nonplanar wing concepts are preferred are high lift demand, geometric restrictions and vortex drag. High lift requirement comes from UAV having no landing gears and low take-off speed. Furthermore, nonplanar wing concepts that reduce vortex drag might have a significant influence on fuel efficiency especially for commercial aircraft since vortex drag constitutes a great amount of total drag. Other than aerodynamic features, some aircraft use nonplanar wings to take advantage of their structural characteristics. Designs, which benefit from structural efficiencies, not only reduce takeoff weight but also might gain the ability to accommodate larger wingspan resulting in lower induced drag without increasing structural weight of the aircraft. This translates to the fact that some designs exploit the nonplanar concepts to improve different aspects of the flight performance including high lift, stability and structural utilities (Kroo, 2005). Some nonplanar wing configurations are explained based on Kroo's studies in the following sections.

3.1.2.1. Multiple-Wing Configurations

One of the most common nonplanar wing configurations is a multi-wing. Some examples are biplanes, tandem wings, and other nonplanar formations. Early in the aircraft design history, Wright Brothers took advantage of the biplanes. Due to flight at low Reynolds numbers, high lift is required, which is satisfied by biplane configuration. As an example from Kroo's research, the comparison of fully laminar flow on monoplane and multiple wings of the same planform area is shown in Figure 3.3. While the two-pieces wing can provide an overall lift coefficient of 0.75, the monoplane can give a 0.4 lift coefficient. This design exploits the formed boundary layer on the downstream wing by decreasing the effective angle of attack and velocity lower than freestream velocity at the trailing edge of the forward wing by the delay of the flow separation.

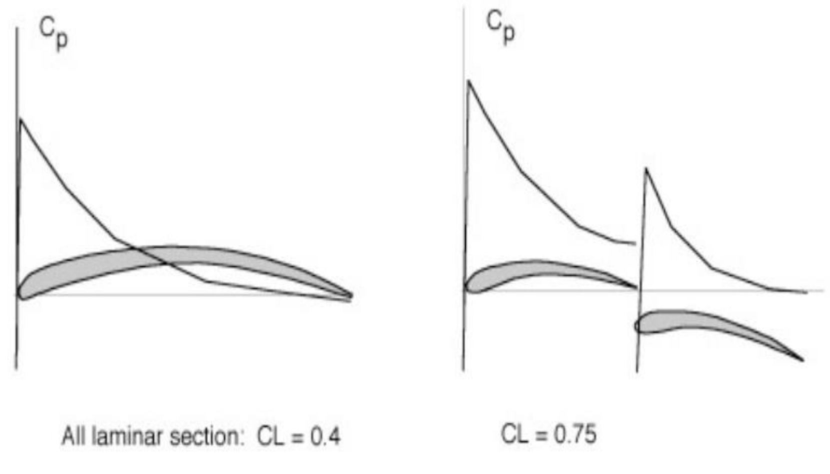

Figure 3.3 Lift coefficient comparison of multiplane wing with monoplane (Kroo, 2005)

Apart from the previously mentioned benefits of vortex drag and lift improvement, the interference between the wings could be turned into an advantage, for instance in the tandem wings: If the forward wing's position is raised relative to the rear wing, interference between the two wings can be favorable. The slotted wing effect comes into the role when two wings are placed near to each other. The stall is a phenomenon that airflow over the upper surface of the wing is no longer attaches to surface under a high angle of attack or low-speed conditions. In Figure 3.4, the stall condition of the front wing is illustrated. Under normal conditions, there is a high-pressure zone beneath wings and low-pressure above wings. In this fashion, air current runs from the lower side of the front wing with high pressure to the upper side of the rear wing with low pressure (Mignet, 1934).

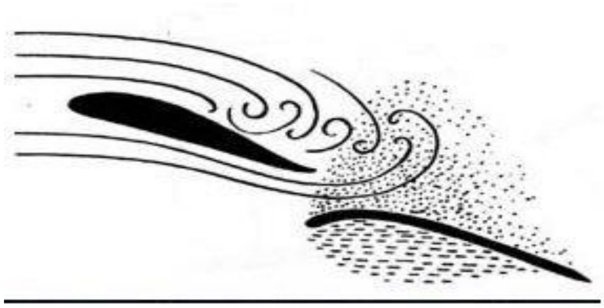

Figure 3.4 Early stage representation of stall effect in tandem wing configuration (Mignet, 1934)

Now considering Figure 3.5, the air current towards the rear wing enhances the turbulence related with high angle of attack and delays flow separation and the stall on the front wing. This phenomenon is also expressed as the slotted wing effect. Besides, airflow over the second wing is also altered both in magnitude and direction due to the existence of the front wing. This is called the downwash effect and it decreases the effective angle of attack on the rear wing. Thus, having control surfaces on the rear wing is beneficial because even if the front wing stalls at a high angle of attack, the pilot/operator will still have control authority thanks to reduced effective angle of attack on the rear wing. For this reason, control surfaces aileron and elevator or so-called "elevons" are placed on the rear wing for the tandem wing design later on this study.

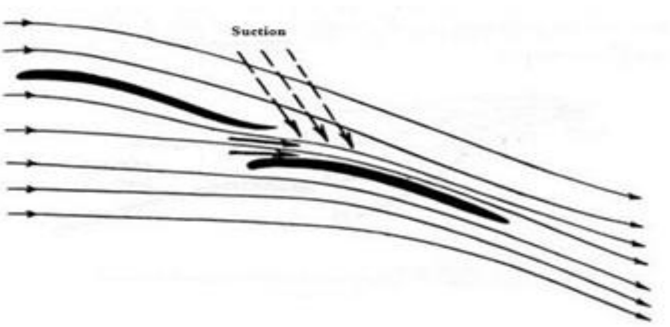

Figure 3.5 Slotted wing effect (Mignet, 1934)

3.1.2.2. Winglets-Wingtip Modifications

Vortex generation around the wing tip occurs due to the finite wing theory. Wingtip devices redistribute and mitigate or prevent wing tip vorticity resulting in less induced drag. The reduction in the drag is connected to the shape of the vortex wake. Besides, bending moment characteristics should be considered when wingtips are loaded. The type of winglets depends on the wing structure and the mission profile. It can be reshaped depending on whether the maneuver or the wind disturbance (gust) is critical for the aircraft. The design of the winglet is unique for each type of aircraft and it is a multidisciplinary task that incorporates aeroelasticity, flutter, stability, and control of aircraft.

3.1.2.3. Closed Systems: Box planes, Joined wings

It is possible to eliminate wingtips by closing the wing all around. Even though the concept of closed systems is rare, they have some remarkable properties. Boxwing, for a specified lift, provides the minimum induced drag and span resulting in fuel efficiency and structural benefits, such an example is shown in Figure 3.6.

Figure 3.6 Example of box wing configuration, an impression of Lockheed Boxwing jet (Aviation Blog, 2016)

Joined wing can also give span efficiency factor more than one. Another interesting feature is that load distribution can be reshaped. Therefore, it provides the designer a flexibility provided that same vortex circulation results in same drag and lift.

3.1.3. Competitor Aircraft

Previous successful designs are tabulated in this section by looking at the similarities of proposed UAV design. Successful competitors are selected in consideration with size, cruise speed, range, and endurance. The design properties of competitor aircraft are shown in Table 3.2 (Data are accessed through online sources of manufacturers). Table 3.2 involves both tandem wing and monoplane configurations. The monoplane configurations are assumed to have similar takeoff weight and wing planform area to tandem wing design. Even though competitor aircrafts in Table 3.2 could also be expanded by adding more UAVs (Coyote, Predix etc.), it is sufficient for the initial sizing process to have six UAV systems.

Table 3.2 Competitor aircraft system characteristics

	Puma	**Switchblade**	**Orbiter**	**Trident TL**	**Bayraktar B**	**Dragon Eye**
Span (m)	2.8	0.7	2.2	0.92	2	1.14
MTOW (kg)	5.9	2.5	5.5	2.3	4.5	2.7
Range (km)	15	10	15	-	55	5
Payload Weight (kg)	0.85	0.8	0.95	0.9	1.1	0.5
Endurance (min)	120	15	90	25	60	45
Stall Speed (m/s)	9.2	-	12.8	20.6	-	8.9
Operating Altitude (m)	152 (AGL)	<152 (AGL)	<4500 (ASL)	-	<1219 (ASL)	90-150 (AGL)
Aspect Ratio	9	-	7.6	-	-	3.33
Propulsion	Electric	Electric	Electric	Electric	Electric	Electric
Launch Type	Hand-launched	Tube-launch	Catapult, bungee	Canister	Hand-launched	Hand-launched
MTOW/Payload Weight	6.94	3.16	5.79	2.55	4.09	5.4

3.2. Initial Sizing

The initial sizing of the tandem wing design starts as if it is a monoplane design. There are two fundamental reasons for this procedure. Firstly, it is beneficial to assess whether the monoplane configuration can meet the design requirements in Section 2.2. The second reason is that there are no straightforward design methodologies regarding tandem wing design in literature. The approach in this thesis is to utilize the calculated wing planform area of monoplane design in tandem wing airframe alternatives in Chapter 4.

3.2.1. Weight Fractions

The first estimate of the takeoff weight of the UAV is calculated in Eqn. (3.1) based on averaging the takeoff weight to payload weight fractions of competitor aircraft given in Table 3.2:

$$\frac{W_{TO}}{W_P} = 4.650 \tag{3.1}$$

Payload selection is a driving criterion in the initial sizing process. The nose geometry, wing planform area, and fuselage geometry are highly affected by the type and geometry of the payload selected. Literature research suggests that typical mini EO/IR camera weight, which can work in real-time and convey imagery to control station, can be estimated as:

$$W_P = 0.9 \text{ kg} \tag{3.2}$$

Hence, from Eqn. (3.1) takeoff weight is calculated as:

$$W_{TO} = 4.185 \text{ kg} \tag{3.3}$$

3.2.2. Wing Geometry Sizing

3.2.2.1. Aspect Ratio

The first to investigate in wing sizing is the aspect ratio. Escaping air around the wingtips lowers the pressure difference between upper and lower wing surfaces, so the lift produced near the tips reduces as well. Moreover, circular flow patterns (wingtip vortices) are generated due to the pressure difference, which constitutes undesired vortex drag. A high aspect ratio wing has a larger span compared to a low aspect ratio wing with the same planform area. Therefore, the proportion of the wing influenced by tip vortex is less (Raymer, 1992). For the initial layout of propeller driven aircraft, Raymer suggests the values in Table 3.3.

Table 3.3 Historical Aspect Ratio (Raymer, 1992)

Propeller aircraft type	Equivalent aspect ratio
Homebuilt	6.0
General aviation-single engine	7.6
General aviation- twin engine	7.8
Agricultural aircraft	7.5
Twin turboprop	9.2
Flying boat	8.0

The homebuilt type is considered as similar to the micro tandem wing UAV, therefore, the aspect ratio is selected as $AR = 6$.

3.2.2.2. Wing Planform Area

Takeoff and landing at low speeds require high lift. It is, therefore, not surprising that the wing planform area of the UAV is calculated at the takeoff condition. The maximum lift coefficient of the UAV without using high lift devices can be estimated as a $C_{Lmax} = 1.3$ for Reynolds numbers around 400,000 (Landolfo, 2008). The stall velocity is expected to be around 15 m/s. Then, wing planform area, wingspan, mean aerodynamic chord length, and wing loading are calculated at 150 m above sea level as:

$$S = \frac{W_{to}}{0.5 * \rho * V_{stall}^2 * C_{L\max}} = 0.267\ m^2 \tag{3.4}$$

$$AR = \frac{b^2}{S} \quad \rightarrow \quad \text{b}=\sqrt{AR * S} = 1.265 \text{ m} \qquad c_{mean} = 0.211 \text{ m} \tag{3.5}$$

$$\frac{W}{S} = 153.8 \text{ N/m}^2 \tag{3.6}$$

However, following conventional monoplane design, the wingspan restriction of 1 meter is not satisfied according to Eqn. (3.5). This will be handled later in this study. Furthermore, high lift is essential for the tandem UAV at low speeds in order to ease launcher design, therefore, there is no need for a sweep angle and twist for the wings.

The sweep angle is used to decrease the unfavorable effects of transonic and supersonic flows; it reduces the freestream velocity in normal direction over the wing causing lower lift. Similarly, twist angle lowers the effective angle of attack resulting in lower lift. Untapered wing is preferred to get wing planform area as large as possible for a specified wing span and the ease of manufacturing.

3.2.2.3. Operating Lift and Drag Coefficient

Important performance parameters, which should be determined and necessary to construct further design analysis, are the aircraft operating lift and drag coefficient. Even though the aircraft is not aerodynamically designed yet, there are still reliable assumptions to estimate aerodynamic coefficients.

Zero lift drag or parasite drag coefficient C_{d_0}value is typically estimated between 0.025 and 0.04 for homebuilt airplanes (Sadraey, 2013). For initial design analysis, $C_{\mathrm{d}_0} = 0.035$ is used. Moreover, additional drag due to non-elliptical lift distribution and flow separation can be accounted by using Oswald span efficiency $'e'$. The value of Oswald span efficiency is typically between 0.7 and 0.95 (Sadraey, 2013). The value is selected as $e = 0.8$ for preliminary design analysis. Firstly, the design lift coefficient can be calculated as follow:

$$W = L = \frac{1}{2}\rho V_{cruise}^{2} S C_L \;\rightarrow\; \mathrm{C}_L = \frac{2W}{\rho V_{cruise}^{2} S} = 0.208 \tag{3.7}$$

With the air density and cruise speed values used as; $\rho = 1.2075\ kg/m^3$ and $V_{cruise} = 35\ m/s$.

Design drag coefficient is calculated with two components: parasite drag coefficient and induced drag coefficient through Eqn. (3.8) and Eqn. (3.9).

$$K = \frac{1}{\pi e A R} = 0.0663 \tag{3.8}$$

$$C_D = C_{D_0} + KCl^2 = 0.0379 \tag{3.9}$$

3.2.2.4. Airfoil Selection

High lift airfoil is significant for a small UAV operating at low Reynolds numbers. However, high lift generation is not solely the desired feature of an airfoil. Pitching moment, stall characteristics, ease of manufacture and thickness ratio should all be assessed when selecting an airfoil.

A significant aspect of airfoil selection is the intended Reynolds number. Reynolds number is calculated for the designed UAV at stall speed as:

$$\mathrm{Re} = \frac{\rho V_{stall} c_{mean}}{\mu} = 210466 \tag{3.10}$$

Six different airfoils that are offered for the low Reynolds number operations in the literature are considered and 2D analyses are performed to select the airfoil with the most suitable characteristics. The results are illustrated in Table 3.4:

Table 3.4 Aerodynamic characteristics of high lift airfoils

Airfoil	C_{l_0}	C_{d_0}	C_{m_0}	$C_{l_{max}}$	Stall Angle (°)	$L/$D
s1210	1.047	0.014	-0.244	1.934	11.4	72.3
s1223	1.168	0.017	-0.267	2.250	13.5	67.1
CH10	1.188	0.017	-0.274	2.006	10.7	69.4
e423	1.099	0.017	-0.238	1.955	12.0	64.2
FX74_CL_140	1.181	0.019	-0.249	2.144	10.5	63.5
cr001sm	1.168	0.020	-0.247	2.079	11.6	58.2

Among the candidates, S1223 airfoil is a well-studied airfoil and offered for small reconnaissance UAV applications in the literature (Selig & Guglielmo, 1997). It offers a high L/D with the highest stall angle and $C_{l_{max}}$ as shown in Table 3.4. Hence, it can be used in tandem design as it also provides acceptable pitching moment and stall characteristics with the highest $C_{l_{max}}$.

3.3. Propulsion

Small tactical reconnaissance and surveillance UAVs are equipped with an electrical propulsion system that yields simple operational use, reduced noise, and low thermal signature. Internal combustion engine is not considered here since explosive material in the backpack of a soldier is highly hazardous. The electrical propulsion system is composed of the electric motor, battery, gearbox (optional), electronic speed control (ESC), propellers, cooling system (optional), wirings and connectors (Gur & Rosen, 2009). In this section, the selection of the battery, electric motor and propeller combination is investigated because the influence of the three on aircraft performance is highly critical.

3.3.1. Battery and Electric Motor Types

UAV design is expected to be lightweight as possible and yet has long endurance. Hence, the selection of the battery type constitutes great importance. There are several battery types available that can be used in an electrical propulsion system. These are nickel-cadmium (NiCad), nickel-metal hydride (NiMH), lithium-ion (Li-ion) and lithium-polymer (Li-Po). When making a battery decision, the parameters, which the designer should look at, are battery's volts, life cycle, weight, run time, capacity and current related properties. The comparison of several battery types is given in Ta*ble* 3.5 (Linden & Reddy, 2002).

Ta*ble* 3.5 Comparison of different battery kinds

	NiCad	**Lead-acid**	**NiMH**	**Li-ion**
Nominal cell Voltage (V)	1.2	2.0	1.2	4.1
Specific energy (Wh/kg)	35	35	75	150
Life	4-6 years	3-8 years	4-6 years	5+ years
Cycle life	400-500	200-250	400-500	1000
Operating Temperature (C^{o})	-20 to 45	-40 to 60	-20 to 45	-20 to 60
Relative cost	3	2	5	9

Li-ion batteries, which have become popular around 1990's thanks to embracement by major electronics companies, have considerably higher specific energy, life cycle and nominal cell voltage compared to others. Moreover, they are exclusively preferred in portable vehicles as they offer high specific energy and cost reduction still improves. Hence, it is decided that lithium based battery is suitable for the propulsion system of the UAV.

There is also a choice needed to be made between Li-ion and Li-Po batteries. They are similar battery types in terms of voltage. The most significant difference between them is the chemical electrolyte among the electrodes. In Li-Po batteries , the electrolyte is gel-like medium, while it is liquid in Li-ion. In terms of performance, Li-Po batteries offer slightly higher specific energy, lower profile section, robust to aging and have safer usage. Li-ion batteries, on the other hand, are cost-effective but less tolerant to aging. Besides, the maximum discharge rate of the Li-ion battery mostly is not sufficient for the need of a UAV or quadrator during take-off condition. Considering the pros and cons, Li-Po battery is chosen for further design analysis since jel like medium electrolyte offers safer usage for military operations, higher specific energy and higher maximum discharge rate.

The electrical motor of propulsion system is selected in consideration with the weight and power requirement of the UAV. There are mainly two types considered here for UAV systems; brushless and brushed electric motors.

Brushless motors, which do not benefit from brushes for commutation, instead, they are commuted electronically. Brushless motors have superiority over the brushed ones, some of these are high dynamic response, a higher ratio of torque delivered to the size of the motor, higher speed, high efficiency, noiseless operation, and longer operational life (Padmaraja, 2003). Hence, brushless motors having high torque delivery makes them preferable where volume and weight restrictions are present such as aerospace and automotive applications. The brushless direct current motor will be used for tandem UAV design.

Brushless direct current motors can also be divided into two classes as out runner and in runner brushless motors. Typically, a brushless out runner motor has a rotating outer shell and stationary core and windings. However, an in runner brushless motor is the opposite having a rotating core and stationary shell. Though two systems have similar physical structures, the significant working principle distinction stems from the positioning of the magnets inside. In the case of in runner brushless motors, as the name implies, magnets are placed inside the shell, which allows the motor to make very fast turning. The gearbox is required to control the high speed and deliver efficient torque. They also operate noisier compared to out runner brushless motors. The out runner, however, has the magnets positioned outside, which yields low rpm but high torque. Therefore, it eliminates the requirement of the gearbox and reduces the weight of the electric motor. The drawback of out runner motor is that the rotating external part makes integration and cooling processes compelling and it operates less efficient than in runner brushless motor (Imam & Bicker, 2014). Nevertheless, the out runner brushless motors are silent, lightweight and provide sufficient rpm levels and highly preferred for direct propeller drive UAV applications, thus, it is chosen for tandem wing UAV design.

3.3.2. Battery Electric Motor and Propeller Combination

3.3.2.1. Electric Motor Selection

In the previous section, it is decided to use lithium polymer battery and out runner brushless direct-drive electric motor. It is time to select a battery-electric motor-propeller combination, which will allow UAV to perform mission requirements. The power rather than thrust is more germane for the propeller driven aircraft (Anderson, 1999). Power required is calculated as:

$$P_R = T_R V \tag{3.11}$$

For the steady climbing flight, equation of motion parallel to the flight direction is given as:

$$0 = T\cos(\varepsilon) - D - W\sin(\theta) \quad (3.12)$$

Where:

P_R = Power required, T_R = Thurst reqired, V = Velocity, $L =$ Lift,
$\varepsilon =$ Thrust incidence angle, W = Instantenous weight, θ = Climb angle

Since thrust inclination to the freestream direction is usually zero or very close to zero, it can be neglected:

$$T = D + W\sin\theta \quad (3.13)$$

Power required equation given in Eqn. (3.11) can be expressed in terms of aerodynamic coefficients and weight with substituting Eqn. (3.13) as following:

$$P_R = (D + W\sin\theta)V \quad (3.14)$$

$$P_R = (D + W\sin\theta)\frac{W}{W}V \quad (3.15)$$

For the steady climbing flight, weight is expressed in terms of lift as:

$$W = L / \cos\theta \quad (3.16)$$

Substituting Eqn. (3.16) into Eqn. (3.15) and rearranging the equation yields:

$$P_R = \frac{W}{\dfrac{C_L / C_D \dfrac{1}{\cos\theta}}{1 + C_L / C_D \tan\theta}} V \quad (3.17)$$

Velocity term in Eqn. (3.17) can also be expressed as:

$$L = W\cos\theta = \frac{1}{2}\rho_\infty V_{c\lim b}^2 S C_{L_{c\lim b}} \quad (3.18)$$

$$V_{c\lim b} = \sqrt{\frac{2W\cos\theta}{\rho_\infty S C_{L_{c\lim b}}}} = \sqrt{\frac{W}{S}\frac{2\cos\theta}{\rho_\infty C_{L_{c\lim b}}}} \quad (3.19)$$

Then, substituting Eqn. (3.19) for velocity into Eqn. (3.17) yields the final form of power required in terms of aerodynamic coefficients as:

$$P_R = \frac{W}{\dfrac{C_L / C_D \dfrac{1}{\cos\theta}}{1 + C_L / C_D \tan\theta}} \sqrt{\frac{W}{S} \frac{2\cos\theta}{\rho_\infty C_{L_{\mathrm{climb}}}}} \tag{3.20}$$

The aircraft's lift and drag coefficients for operating a steady, level flight were calculated in section 3.2.2.3. In Eqn. (3.20), C_L/C_D is required to be calculated in steady climbing flight as well. Eqn. (3.18) is also repeated here with 12 degrees of climb angle and 25 m/s climb speed:

$$C_{L_{\mathrm{climb}}} = \frac{2W\cos\theta}{\rho_\infty V_{\mathrm{climb}}^2 S} = 0.344 \tag{3.21}$$

For the calculation of $C_{D_{climb}}$, it is assumed that induced drag factor (K) and C_{D_0} of the stedy level flight will still remain same:

$$C_{D_{\mathrm{Climb}}} \approx C_{D_0} + KCl_{\mathrm{climb}}^2 = 0.043 \tag{3.22}$$

Lift to drag ratio is found as:

$$C_{L\mathrm{climb}} / C_{D\mathrm{climb}} = 8.03 \tag{3.23}$$

The power required, then, is calculated using Eqn. (3.20) with corresponding values:

$$P_R = \frac{W}{\dfrac{C_L / C_D \dfrac{1}{\cos\theta}}{1 + C_L / C_D \tan\theta}} \sqrt{\frac{W}{S} \frac{2\cos\theta}{\rho_\infty C_{L_{\mathrm{climb}}}}} = 365.4 \text{ Watts} \tag{3.24}$$

The power required calculated as 365.4 W is the power required from electric motor/propeller combination and it is always less than the shaft power delivered to the propeller through the motor shaft (Anderson, 1999). The propeller converts shaft power to thrust by accelerating air through itself. The effectiveness of this conversion is the propeller efficiency. Since the propeller of tandem UAV can operate in high rpm values, the propeller efficiency is taken as $\eta_{pr} = 0.7$ for the homebuilt type aircraft. Also, there is always an energy loss between electrical power supplied to the motor and mechanical power converted to the shaft. The ratio of input power to the output shaft power is called electric motor efficiency. It is taken as a typical value as $\eta_{motor} = 0.85$. Then, the power required from the shaft and battery is calculated as:

$$P_{shaft} = \frac{1}{\eta_{pr}} P_R = 520.5 \text{ W} \tag{3.25}$$

$$P_{battery} = \frac{1}{\eta_{motor}} \frac{1}{\eta_{pr}} P_R = 619.7 \text{ W} \tag{3.26}$$

The same procedure is also repeated for the steady level flight with zero climb angle and 35 m/s flight speed. Related power required values are found as:

$$P_R = 261.6 \text{ W} \tag{3.27}$$

$$P_{shaft} = \frac{1}{\eta_{pr}} P_R = 373.7 \text{ W} \tag{3.28}$$

$$P_{battery} = \frac{1}{\eta_{motor}} \frac{1}{\eta_{pr}} P_R = 444.9 \text{ W} \tag{3.29}$$

It is obvious from the power required values found in Eqn. (3.26) and Eqn. (3.29) that the most stringent mission is the climbing flight. Based on this climbing flight requirement, AXI 4130-20 v2 Gold Series Out Runner Electric Motor with 14x10 dual-blade propellers is chosen. The specification from the motor manufacturer is provided as follows:

Table 3.6 Specifications of AXI 4130-20 v2

Specification	
Number of cells	6 – 8 Li-Po
RPM/V	305 RPM/V
Max efficiency	88%
No load current/10 V	1,2 A
Current capacity	55A/60 s
Internal resistance	99 mohm
Dimensions (diameter x length)	49.8 * 65.5 mm
Weight with cables	409 g

It is provided in the manufacturer's data that AXI 4130-20 v2 motor with 14x10 propeller has the following performance parameters:

Table 3.7 The use of 4130/20 v2 with 14x10 propeller

Motor	Propeller	Battery	RPM	I/A	P-Out (W)	P-In (W)	Efficiency (%)
4130/20	14x10	24xRC 1700	7010	29.6	649	767	86

It is given in Table 3.7 that power transmitted to the shaft from the electric motor is 649 W at full throttle and the requirement for the climb with 12 degrees, calculated in Eq. 3.27, is 520.5 W. This translates that electric motor is chosen with a safety margin of 20% higher than the requirement considering the voltage drop of the battery during flight.

3.3.3. Battery Selection

The lithium-polymer battery was found to be the most suitable for the tandem wing UAV design previously. In this section, the performance properties of lithium-polymer battery are determined in consideration with AXI 4130 v2 motor whose specifications are given in Table 3.6 and Table 3.7. The battery should be able to provide the electrical power for the flight computer, electric motor and other electronic subsystems to perform mission requirements of a minimum range of 5 kilometers and 10 minutes endurance.

In Table 3.7, the 24 Volts battery is suggested to achieve 649 W shaft power. Also, the suggested number of cells for this electric motor is between 6S-8S. Thus, 6S battery which would provide 25.2 V at full charge is used. The instantaneous power requirement during cruise and climb are calculated in the previous section. Maximum power consumption for 12 degrees climb angle with 25 m/s freestream climb velocity corresponds to:

$$ROC = 5.2 \text{ m/s} \tag{3.30}$$

The time to climb 150 m altitude:

$$\frac{Desired\ Altitude}{ROC} = 28.9 \text{ s} \tag{3.31}$$

Considering other maneuvers that will consume high power, such as stiff turns and gust corrections, the maximum power consumption time is estimated approximately 1.5 minutes. Total cruise time is also considered as 8.5 minutes. Thus, the flight time ratio at maximum capacity is 0.15 and the flight time ratio of cruise condition is 0.85. In Table 3.8, corresponding power required, ampere, flight time and capacity values are illustrated.

Table 3.8 Determination of battery capacity

	Battery Power Required (W)	**Voltage (V)**	**Instantaneous Ampere (A)**	**Flight Time (s)**	**Required Capacity (mAh)**
Climb- other maneuvers	619.7	24	25.8	90	646
Cruise	449.9	24	18.5	510	2626
Total	-	-	-	600	3272

It is also a recommended practice not to consume all the capacity of battery during flight since it reduces the lifetime and even damages battery irreversibly. Hence, using a safety factor of 0.15, 6S 3700 mAh battery is selected whose specifications are given in Table 3.9

Table 3.9 GENS ACE liPo battery pack specifications

Specification	
Number of cells	6S
Capacity (mAh)	3700
Max continuous discharge	35 C
Max burst discharge	70 C
Weight (g)	597
Dimensions (mm)	138.7*43*48.2

Another significant parameter in battery selection is the maximum continuous discharge. In Table 3.9, it is given as 35 C, which implies that with 3700 mAh battery capacity it can discharge 129.5 A. Hence, the selected battery is expected to operate safely in given the flight regime.

Furthermore, between the electric motor and the battery, the electronic speed control (ESC) is needed. ESC is an electronic circuit that regulates the rotation speed of the electric motor by adjusting the discharge rate from the battery. The ESC generally is driven by pulse with modulus (PWM) signals by adjusting the duty cycle. Hence, flight computer must have PWM output pins in order to drive brushless electric motor. Advance Pro Opto, which allows maximum discharge rate 90 A, is selected whose specifications are given in Table 3.10.

Table 3.10 Advance 90 Pro Opto ESC specifications

Specification	
Continous Max Amp (A)	90 A
Cells liPo	4-10 S
Voltage (V)	12-42
Dimensions (mm)	65* 55*17
Weight (g)	90

3.4. Matching Diagram

A matching diagram, which shows the relationship between the wing loading and the power loading, is constructed here to illustrate where the design point falls into the design space in terms of various performance aspects of the aircraft. The ratio between the aircraft weight and engine power is referred as power loading, which is a more germane term for propeller-driven aircraft. Several performance requirement equations are already developed in reference (Sadraey, 2013) and only repeated here.

One performance requirement of the aircraft is stall speed. This requirement is independent of power loading and related to aerodynamics of the aircraft. Hence, the graph of power loading will be a vertical line for all circumstances as shown by the purple line in Figure 3.7. The stall speed constraint equation is given in Eqn. (3.32):

$$\left(\frac{W}{S}\right)_{stall} = \frac{1}{2}\rho V_s^2 C_{L_{\max}} \tag{3.32}$$

The second performance requirement is the maximum speed. Aircraft weight, wing size, and engine power are major factors for the maximum speed. Since there is no specific maximum speed requirement for the tandem wing UAV, the maximum speed is derived from the cruise speed of the UAV. It is suggested by Sadraey that the maximum speed is 20-30% higher than the cruise speed. The maximum speed constraint equation is given for propeller-driven aircraft in Eqn. (3.33):

$$\left(\frac{W}{P}\right)_{MaxSpeed} = \frac{\eta_{pr}}{\frac{1}{2}\rho V_{\max}^3 C_{D_0}\frac{1}{W/S} + \frac{2K}{\rho\sigma} V_{\max}\frac{W}{S}} \tag{3.33}$$

In Eqn. (3.33), σ stands for the density ratio of flight altitude and sea level.

Another important performance requirement is the rate of climb. It represents the how fast aircraft can climb to higher altitudes for a given flight condition. The ROC requirement equation for propeller driven aircraft is given in Eqn. (3.34).

$$\left(\frac{W}{P}\right)_{ROC} = \frac{1}{\frac{ROC}{\eta_{pr}} + \sqrt{\frac{2}{\rho\sqrt{\frac{3C_{D_0}}{K}}}\frac{W}{S}}\left(\frac{1.155}{(L/D)\eta_{pr}}\right)} \tag{3.34}$$

The last performance requirement considered in this study is the ceiling. The word ceiling stands for the highest altitude which an aircraft can perform a straight level flight. There are various types of the ceiling: Absolute ceiling, service ceiling, cruise ceiling, and combat ceiling. The highest ceiling type, as the name implies, is absolute ceiling and the lowest one is combat. Since there is no specific requirement for the absolute ceiling or service ceiling, the cruise ceiling is taken into consideration where the requirement is that aircraft can climb at a rate of 1.5 m/s. The equation for the ceiling requirement is similar to the ROC constraint equation, given in Eqn. (3.34):

$$\left(\frac{W}{P}\right)_{C} = \frac{\sigma_c}{\frac{ROC_c}{\eta_{pr}} + \sqrt{\frac{2}{\rho_c\sqrt{\frac{3C_{D_0}}{K}}}\frac{W}{S}}\left(\frac{1.155}{(L/D)\eta_{pr}}\right)} \tag{3.35}$$

Equations from (3.32) to (3.35) are sketched in one plot for changing wing loading values called the matching diagram. The Figure 3.7 shows the variation of the power loading with respect to the wing loading.

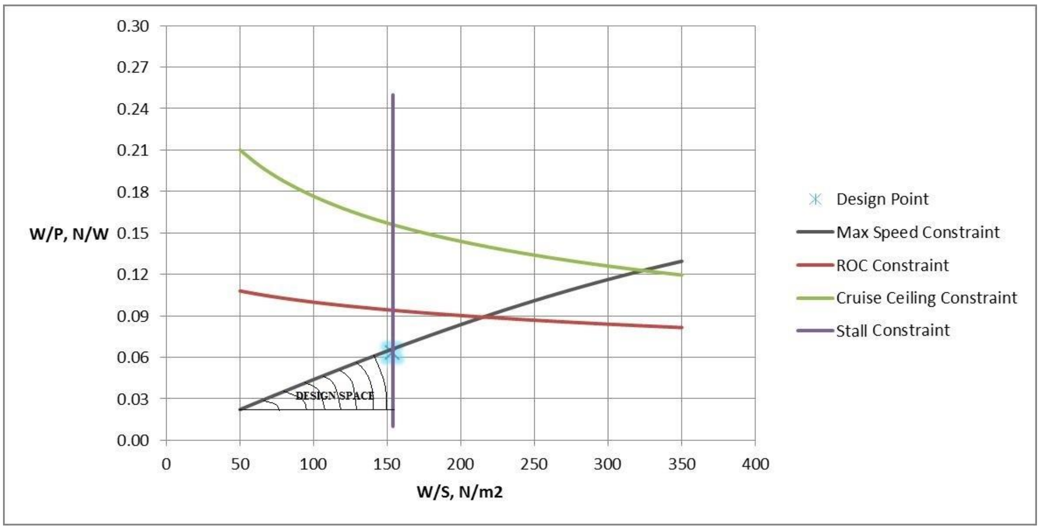

Figure 3.7 Matching diagram for the tandem wing design

In Figure 3.7, previously selected/calculated electrical engine and wing configuration is plotted. It is proven that the selected design falls into the design space proposed by the performance requirements according to the matching diagram.

3.5. Flight Control System

3.5.1. Micro Controller

The microcontroller is fundamentally the computer board, which controls and coordinates subsystems onboard (Imam & Bicker, 2014). The primary functions of the microcontroller can be stated as processing flight control law based on flight information provided by other sensors, communication with a ground control station and logging the flight data onboard or transferring to telemetry. In the selection of microcontroller, there are several factors affecting the choice, such as processing speed, weight, size and input/output communication pins. These and more other factors are taken into consideration in Imam & Bickers research to select microcontroller from available products. The comparison result is repeated here in Table 3.11.

Table 3.11 Micro controller selection (1: Worst 5: Best)

Criterion	Beagle	Explorer 16	Atmel AT9	Arduino
Dimension	1	1	2	5
Weight	2	2	2	5
Power consumption	2	3	4	4
Process speed	5	5	4	3
Number of I/O pins	4	4	4	4
Number of PWM pins	3	4	3	4
Cost	1	2	2	3
Total Score	18	21	21	28

Arduino Mega board is a lightweight microcontroller whose specifications are given in Table 3.12. Hence, Arduino Mega is selected as flight computer for the tandem wing design.

Table 3.12 Arduino Mega specifications

Specification	
Weight (g)	40
Dimensions (mm)	65x40x10
Processing speed (MHz)	16
I/O pins	54
Power consumption (W)	20

3.5.2. Navigation Sensors

Navigation sensors are used to acquire measures of aircraft attitude, acceleration, velocity and position. The navigation system for the tandem wing UAV is considered as an inertial navigation system (INS) complemented by a GPS as suggested in the work of Imam and Bicker. In this study, GPS is considered optional since antennas alter the airframe design. Nevertheless, the framework of INS/GPS subcomponents are selected as InvenSense MPU-6050 inertial measurement unit (IMU) and Mediatek MT3329 GPS receiver.

MPU 6050 is a device that combines a 3-axis gyroscope and a 3-axis accelerometer. Its gyro scale range is ± 2000 °/s, gyro rate noise 0.005 dps/$\sqrt{Hz}$, sensitivity of 16.4 LSB/ °/s, acceleration scale range is ± 16, 16.4 LSB/g sensitivity and IMU operating supply voltage is 2.375-3-46V with 4x4x0.9 mm dimensions and 2 grams in weight. This IMU has a built-in digital low pass filter with selectable cut-off frequency.

Mediatek MT3329 is a 10 Hz GPS module that can be easily integrated into aircraft. There is a ready to use library model provided by Mediatek. Its position accuracy is stated as <3m, sensitivity up to -165dBm tracking, the power consumption rate of 48mA and weight of 9.45 grams with 38x38x7.8 mm dimensions. Typically**,** the weight of antennas is 20 grams for this class of UAV, resulting in total weight of GPS module approximately 30 grams.

Radio frequency (RF) communication technology is widely used in aerospace applications. The data-link onboard and ground control station is type of two-way communication. Uplink delivers flight command, trajectory shaping, and payload commands. Downlink transmits inflight data of the UAV and the data from the payload, for instance, video imagery. Following the study of Imam and Bicker, a pair of RFD900 (30 g) involving the receiver and transmitter modules RF modem is selected to inflight data delivery and trajectory uploading. It features up to 20 km of distance communication with suitable antennas. Mini COFDM UAV Video Transmitter is also used to deliver video imagery to the ground station. It is a long range wireless video transmitter that can operate up to 15 km with 110 g in weight and 74x23x65mm dimensions.

It is decided that elevon and a rudder are used in the control actuator system of the UAV. Hence, three pieces of Ditex TD0606M are used. TD0606M is a servo full metal gear, with a digital position encoder instead of an analog potentiometer. This servo is also driven by the same type of PWM signal as a brushless electric motor chosen previously. This servo is capable of providing 58 Ncm torque under 8.4V applied having only 23g in weight.

3.6. Weight Build-Up

Upon the selection of subsystems of the UAV, the weight estimation proposed in section 3.2.1 can be examined again. Even though there are still parts of the aircraft which could not be weighed accurately without having CAD model or being built, the allocated empty weight (fuselage, wing, and tail) can still be estimated by using historical data and statistics. This type of calculation relies on the past aircraft data with similar configuration.

The general technique offered in the book of Sadraey states maximum takeoff weight calculation can be broken down into several elements:

$$W_{TO} = W_{PL} + W_{FCS} + W_{Prop} + W_E \tag{3.36}$$

The right hand side weight components in Eqn. (3.36) are payload, flight control system, propulsion and empty weights. In order to simplify calculation Eqn. (3.36) can be rewritten as:

$$W_{TO} = \frac{W_{PL} + W_{FCS}}{1 - \frac{W_E}{W_{TO}} - \frac{W_{Prop}}{W_{TO}}} \tag{3.37}$$

Eqn. (3.37) can be used to estimate takeoff weight by substitution of appropriate weight fractions. The payload, flight control system and the propulsion system are determined accurately before, however, the empty weight fraction is estimated from statistics.

Empty weight fraction is empirically estimated based on the empty weight fraction of similar aircraft. The empirical equation for empty weight fraction for the microlight type of aircraft is given in Eqn. (3.38):

$$\frac{W_E}{W_{TO}} = -7.22 * 10^{-5} W_{TO} + 0.481 \tag{3.38}$$

Note that Eqn. (3.38) is given in British Unit System. Then, substituting the corresponding takeoff weight estimated in Eqn. (3.3) yields empty weight fraction and empty weight of the aircraft:

$$\frac{W_E}{W_{TO}} = 0.48 \tag{3.39}$$

$$W_E = 2.01\ \text{kg} \tag{3.40}$$

In order to calculate overall weight, weigh build-up components are added up; propulsion system, flight control system, payload and empty weights are tabulated in Table 3.13.

Table 3.13 Weight build-up

System	**Components**	**Weights (g)**
Propulsion	Electric motor	409
	Propeller	18
	Battery	597
	ESC	90
Total Propulsion		**1114**
Flight Control System	Micro controller	40
	IMU	2
	GPS + antennas	29.5
	Data link	30
	Video transmitter	110
	Servos	69
Total FCS		**281.5**
Payload		**900**
Empty Weight		**2010**
Cumulative total takeoff weight		**4305**

The design of the aircraft is an iterative process by nature. The calculation in Eqn. (3.3) is solely dependent on the 6 similar aircraft data. Thus, the accuracy of the results largely depends on them. There is a 3% error in the estimation of the takeoff weight of the UAV according to Table 3.13. The takeoff weight found in Table 3.13 is used in Eqn. (3.38) iteratively as illustrated in Table 3.14.

Table 3.14 Weight iteration process

Iteration	**Empty Weight Fraction**	**Empty Weight (kg)**	**Takeoff Weight (kg)**
IT #1	0.48	2.01	4.30
IT #2	0.48	2.07	4.36
IT #3	0.48	2.10	4.39
IT #4	0.48	2.11	4.40
IT #5	0.48	2.11	4.40

After 5 iterations the takeoff weight has converged to the value of $W_{TO} = 4.40$. Hence, the takeoff weight estimation is slightly increased than the initial estimation. The initial sizing process explained in this chapter is repeated from the start to get more reliable aircraft parameters with new takeoff weight estimation. Only the results are illustrated in Table 3.15:

Table 3.15 Second calculation of the performance parameters

Performance Parameters	
Take off weight, kg	4.40
Wing planform area, m^2	0.281
Wing span, m	1.299
Chord length, m	0.216
K	0.066
Wing loading, N/m2	153.8
C_L operation	0.208
C_D operation	0.038
L/D climb	8.029
Thrust required cruise, N	7.875
P_R climb, Watt	383.9
P_R cruise, Watt	275.6
P_{shaft} climb, Watt	548.4
$P_{battery}$ climb, Watt	652.9
P_{shaft} cruise, Watt	393.7
$P_{battery}$ climb, Watt	468.7

Previously selected electric motor, battery and propeller combination still satisfies the mission requirement with approximately 15% safety coefficient. Hence, it is decided to continue with the same combination.

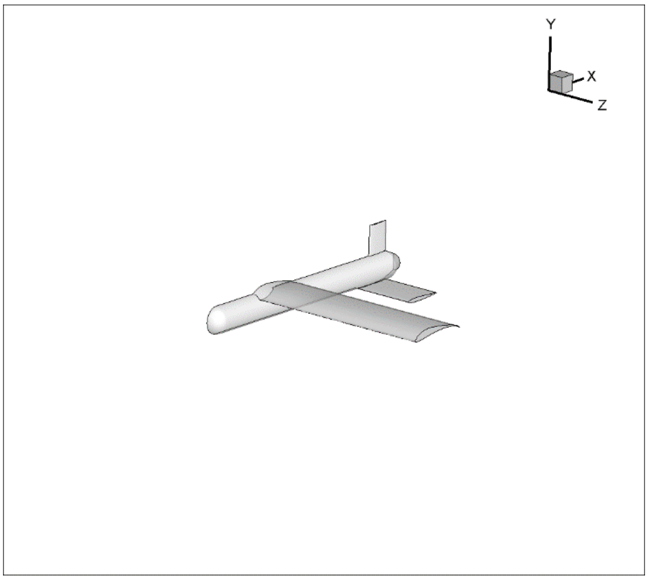

Figure 3.8 Monoplane design illustration

On the other hand, the wingspan requirement of 1 meter is yet to be satisfied with calculated wingspan $b \approx 1.3m$, as the schematic illustration of monoplane design is shown in Figure 3.8. The wingspan restriction will drive the design process towards the tandem wing design, which is the topic of the next chapter of this thesis.

CHAPTER 4

AERODYNAMIC DESIGN OF THE TANDEM WING

4.1. The Tandem Wing Configuration

The initial sizing process in previous chapter reveals that the wing span restriction is not fulfilled. The tandem wing configuration is selected due its rewarding features; one is to provide the lift requirement of the UAV. The tandem wing is a configuration of two wings, one in front and the other one in back. Both wings contribute to the generation of lift with a reduced span.

The slotted wing effect is observed in tandem wing configuration. The idea is similar to slotted flap shown in Figure 4.1 (Raymer, 1992). There is a slot between the wing and the flap. The slot allows high pressured air from beneath wing to flow over the top of the flap, which tends to delay flow separation while increasing lift and reducing drag.

Figure 4.1 Slotted flap

When the two wings of the tandem configuration are placed close enough, the flow separation is also delayed similar to the slotted flap due to the pressure difference between the wings. However, there is no rule of thumb on how the wings should be placed relative to each other for tandem wing aircraft in the literature. In this chapter, the effect of the relative position of the wings is analyzed by CFD analysis using ANSYS Fluent CFD Solver. The linearity of moment coefficient (C_M)versus angle of attack (α) curve, the stall angle of attack (α_{stall}) and the maximum lift coefficient

$C_{L_{max}}$ are analyzed for various wing locations. Besides, the effect of rear wing existence on the front wing's turbulence characteristics are investigated in detail.

The CFD results are evaluated in order to reach the aircraft configuration having the most favorable aerodynamic properties. The effect of wings relative position become more obvious on aerodynamic properties of the UAV through CFD analysis.

4.2. Tandem Wing Sizing

The initial sizing of the tandem wing configuration starts as if it is a monoplane configuration. The previously calculated planform wing area of monoplane design is distributed among the wings of tandem design. In order to satisfy the wingspan requirement of 1 meter and still avoid the induced drag effects, the aspect ratio of the front wing is kept same with 1-meter wingspan. The remaining wing area is allocated with a 5% safety factor increment to the rear wing with varying aspect ratio values. The safety factor is utilized due to reduced effective angle of attack on the rear wing caused by the forward wing downwash. The first step is to pack all the subsystems into the fuselage. The leading edge of the front wing of the aircraft is allowed to be placed minimum of 170 mm distance from the nose of the aircraft in order to avoid interference with the onboard payload.

The design space of the tandem wing, which is analyzed through CFD analysis, is illustrated in Table 4.1 and also in Figure 4.2 as a series of airframe configurations. It is good practice to have two wings to have a similar aspect ratio. Thus, the rear wing aspect ratio is selected similar to that of the forward wing. The location of the trailing edge of the rear wing is fixed to the end of the fuselage to increase the control surface effectiveness of the UAV.

Table 4.1 Design space

The leading edge location of the front wing, mm	$X_{frontLE}$ = [170 220 270 320 370 420]
The aspect ratio of the front wing	AR_{front} = [6]
The leading edge location of the rear wing, mm	X_{rearLE} = [dependent on AR_{rear}]
The aspect ratio of the rear wing	AR_{rear} = [5 6 7]

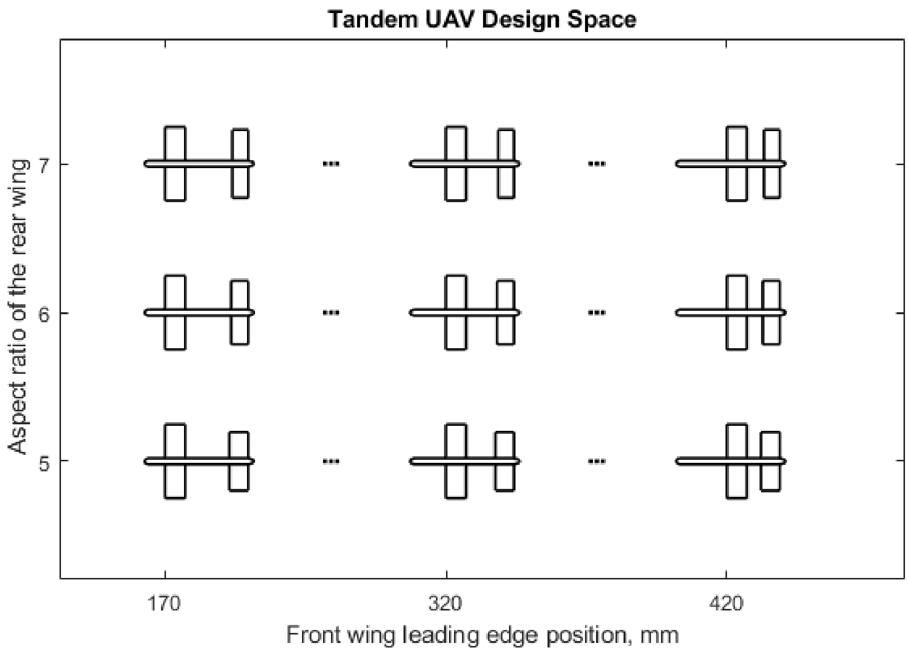

Figure 4.2 Tandem wing UAV design space representation

The wing planform area is calculated previously as $S = 0.281\ m^2$ for the monoplane configuration. This area is allocated between the two wings with a safety factor in the following manner:

$$S_{front} = b^2_{front} AR_{front} = 0.167\ \mathrm{m}^2 \quad (4.1)$$

$$S_{rear} = (S - S_{front})*1.05 = 0.120\ \mathrm{m}^2 \quad (4.2)$$

$$\begin{aligned} b_{rear} &= \sqrt{AR_{rear} * S_{rear}} = 0.775\ \mathrm{m} \\ \mathrm{c}_{rear} &= b_{rear} * AR = 0.155\ \mathrm{m} \end{aligned} \quad (4.3)$$

Even though there is no tail in the tandem wing configuration, it is interesting to calculate the horizontal tail volume coefficient considering the rear wing as if it is a tail. The horizontal tail volume coefficient typically varies between the values 0.5 to 1 for the conventional aircraft designs from sailplane to military cargo aircraft (Raymer, 1992). The horizontal tail volume coefficient is calculated as:

$$S_{HT} = \frac{c_{HT} C_w S_w}{L_{HT}} = 2.22 \tag{4.4}$$

It is understood from Eqn. (4.4) that empiric methods of horizontal tail volume coefficient calculation are not applicable since the tandem wing design does not fall into the conventional aircraft design category.

Table 4.1 reveals that there are 18 different airframe configurations to be analyzed. The corresponding geometric properties of 18 UAV configurations, i.e. center of gravity and moment of inertia about the longitudinal axis, are illustrated in Table 4.2. The geometric properties are utilized for pitching moment characteristics and autopilot design.

Table 4.2 The geometric properties of airframe alternatives

Tail AR=5	C.G Location (mm)	Iyy (kgm^2)
cfg #1	327	0.372
cfg #2	341	0.364
cfg #3	355	0.36
cfg #4	369	0.361
cfg #5	383	0.366
cfg #6	397	0.375
Tail AR=6		
cfg #7	327	0.375
cfg #8	341	0.367
cfg #9	355	0.363
cfg #10	369	0.363
cfg #11	383	0.368
cfg #12	397	0.377
Tail AR=7		
cfg #13	328	0.376
cfg #14	342	0.368
cfg #15	355	0.364
cfg #16	369	0.364
cfg #17	384	0.369
cfg #18	398	0.378

4.3. CFD Analysis

4.3.1. CFD Validation and Turbulence Model Selection

One major aspect of CFD analysis is to select a turbulence model for the simulation. One turbulence model cannot be considered as a final solution to different flow problems or even Reynolds numbers. Working with the low Reynolds number flow poses a challenge in simulations. Before starting to analyze tandem wing configuration, it is essential to select a suitable turbulence model and to validate the CFD methodology (Aftab, Rafie, Razak, & Ahmad, 2016). Numerical analysis is carried out by four different turbulence models commonly used: Spalart Allmaras (S-A), two-equation K-ω, two-equation K-ε and four-equation transition SST

(Doosttalab, Mohammadi, Doostalab, & Ali., 2012) (Aftab, Rafie, Razak, & Ahmad, 2016). Then, results are compared with experimental wing data for NACA 4415 airfoil section provided by Ostowari and Naik (Ostowari & Naik, 1985). The purpose of the validation is to observe if computational results agree with real-world experimentation. The experimental data provided by Ostowari and Naik is used for the CFD validation studies since the data is provided for a finite aspect ratio wing with cambered airfoil at a low Reynolds number which is consistent with both flight speed and wing aspect ratio of the tandem wing UAV. Besides, this wind tunnel data is open source and well documented which makes it useful since there are few studies in the open literature at such low Reynolds number.

The experimental data itself also has random measurement errors and bias, which should be quantified. Considering the application, CFD validation shall be permissible for some level of accuracy.

4.3.1.1. Near Wall Treatment

Regions close to the airfoil surface have fine mesh density and gradually become coarse while moving away from the surface of the wing in order to improve the efficiency of the simulation runs. There is a compromise between the desired accuracy and the cost of the solution since the finer mesh resolution results in a highly time consuming process.

The presence of the wall affects the degree of turbulence, where large gradients in the viscous regions exist (Song, Zhang, & Lin, 2017). The usage of 'y^+' is a recommended strategy to deal with wall-bounded turbulent flows. Non-dimensional distance y^+ is the ratio of turbulence and laminar influences in a cell, which is defined as:

$$y^+ = \frac{y\mu_T}{\upsilon} \tag{4.5}$$

$$\mu_\tau = \sqrt{\frac{\tau_w}{\rho}} \tag{4.6}$$

In the Eqn. (4.5) and Eqn.(4.6), y is the height of the first cell to be determined, μ_τ represents the friction velocity, ϑ is the kinematic viscosity and τ_w is the shear wall stress. The wall shear stress and skin friction coefficient can be calculated empirically as (Song, Zhang, & Lin, 2017):

$$\tau_w = \frac{1}{2}\rho V_\infty^2 C_f \tag{4.7}$$

$$C_f = 0.058 * \mathrm{Re}^{-0.2} \tag{4.8}$$

The wall y^+ must be selected carefully since near wall regions have large gradients in solution variables. Figure 4.3 shows the viscosity-affected region with 3 zones named:

- Viscous laminar sublayer ($y^+<5$)
- Buffer layer ($5<y^+<30$)
- Log-law region ($y^+>30$ to 60)

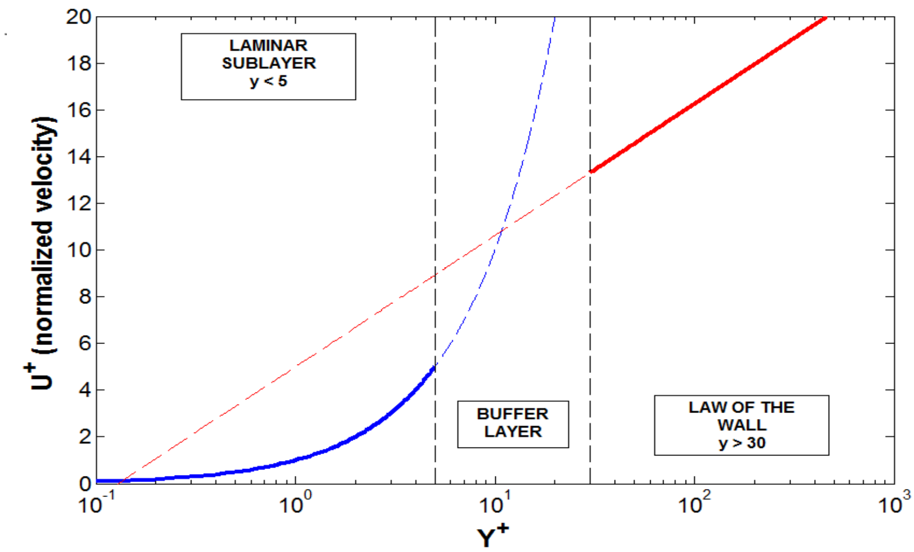

Figure 4.3 Subdivisions of the near wall

Choosing y^+ is significant to capture transition behavior. To resolve the boundary layer flow, i.e. viscous sublayer, and to capture gradients in the solution variables, y^+ value is kept as $y^+<1$ around the wing in the first validation analysis of NACA 4415 wing. After, the analysis will be performed with $y^+<40$ for comparison purposes.

4.3.2. NACA 4415 Wing Numerical Analysis

i) $y^{+}<1$

A wing with NACA 4415 airfoil section, chord length 0.305 m and aspect ratio of 6 is modeled in ANSYS Design Modeler and imported to FLUENT for meshing and numerical analysis. The test conditions are provided as:

Table 4.3 NACA 4415 wing test condition

	Reynolds Number	Mach Number
Test Condition	500,000	0.09

The first cell height is determined through Eqns. (4.9) and (4.12) as follows:

$$C_f = 0.058 * \mathrm{Re}^{-0.2} = 0.0042 \tag{4.9}$$

$$\tau_w = \frac{1}{2}\rho V_\infty^2 C_f = 1.771 \text{ Pa/m}^2 \tag{4.10}$$

$$\mu_\tau = \sqrt{\frac{\tau_w}{\rho}} = 1.363 \text{ m/s} \tag{4.11}$$

$$y = \frac{y^+ \upsilon}{\mu_T} = 1.330 * 10^{-2} mm \tag{4.12}$$

The resulting mesh resolution around the NACA 4415 wing is shown in Figure 4.4.

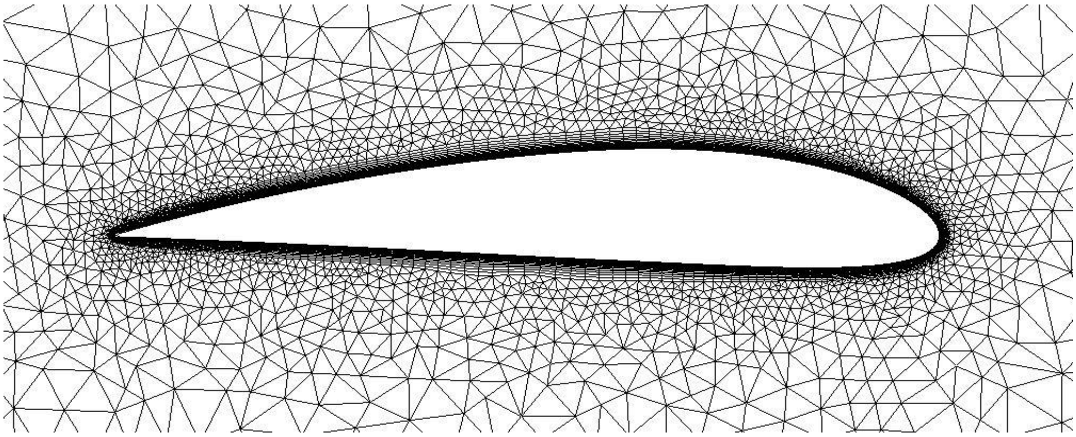

Figure 4.4 Solution domain

Input velocity for the various angle of attack cases is adjusted to match experimental condition with Reynolds number of 500,000 and Mach number 0.09. Pressure based solver is implemented. The double precision calculation method is used to prevent calculation errors and convergence creation is set based on the convergence of lift and drag. First 1000 iterations are ignored in terms of convergence criterion, then, lift and drag coefficients are converged if and only if the last 150 iterations are all in the change interval of $1x10^{-3}$.

The grid independency test is carried out by increasing the mesh and node numbers iteratively to identify accurate mesh resolution. The finer mesh is used around the leading and trailing edges and a higher number of cells is employed close to the surface at each test. The Standard K-ω turbulence model is used at 6^o angle of attack. The mesh size is enhanced until the new mesh size results in no considerable difference in C_D. The test results are illustrated in Table 4.4 and in Figure 4.5 as how increment in the mesh resolution results in a convergence in drag coefficent.

Table 4.4 Grid independency test $y^+<1$

	Number of nodes	**Mesh cells**	C_D
Test #1	720452	2209106	0.03624
Test #2	809140	2632610	0.03674
Test #3	969057	2900577	0.03658
Test #4	1129318	3170766	0.03656
Test #5	1290298	3445074	0.03655
Test #6	1451617	3721562	0.03645
Test #7	1613600	4001600	0.03645

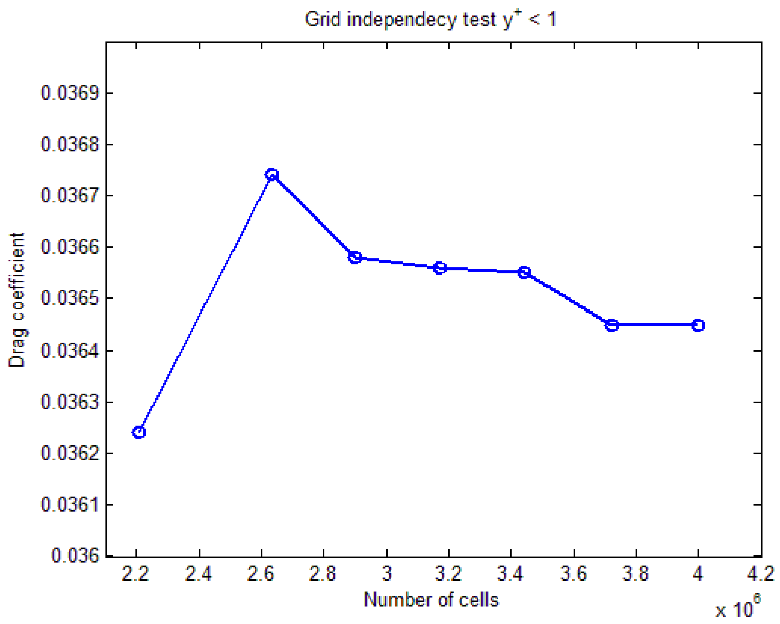

Figure 4.5 Grid independency test $y^+<1$

According to Table 4.4, it is decided to use the mesh resolution in Test #6, which corresponds to 3.7 million mesh cells.

Then, numerical analysis is performed for each turbulence model and various angles of attack. The comparison plots of drag coefficient, lift coefficient and pitching moment coefficient with experimental data are shown in Figure 4.6, Figure 4.7 and Figure 4.8, respectively.

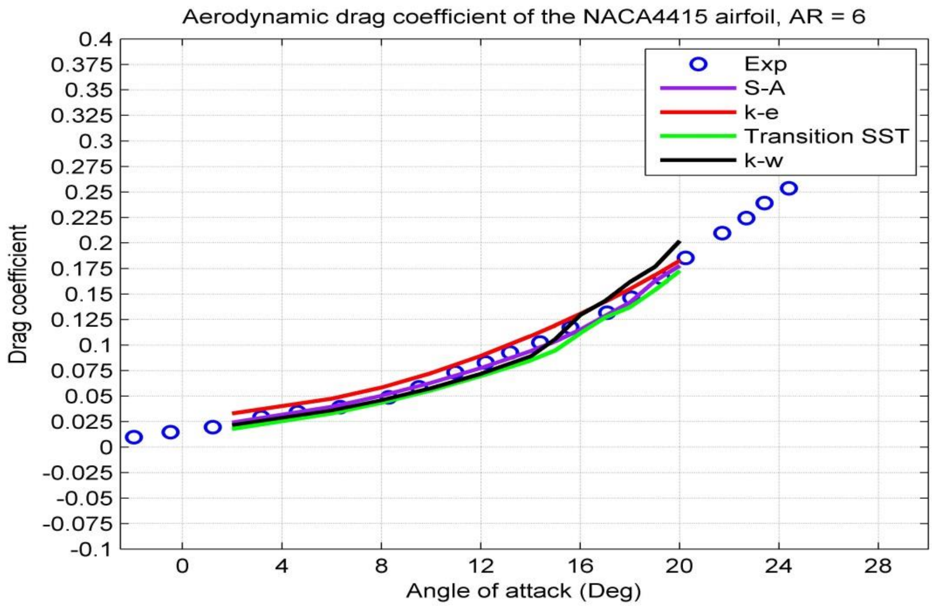

Figure 4.6 Comparison of drag coefficients with experimental data ($y^+<1$)

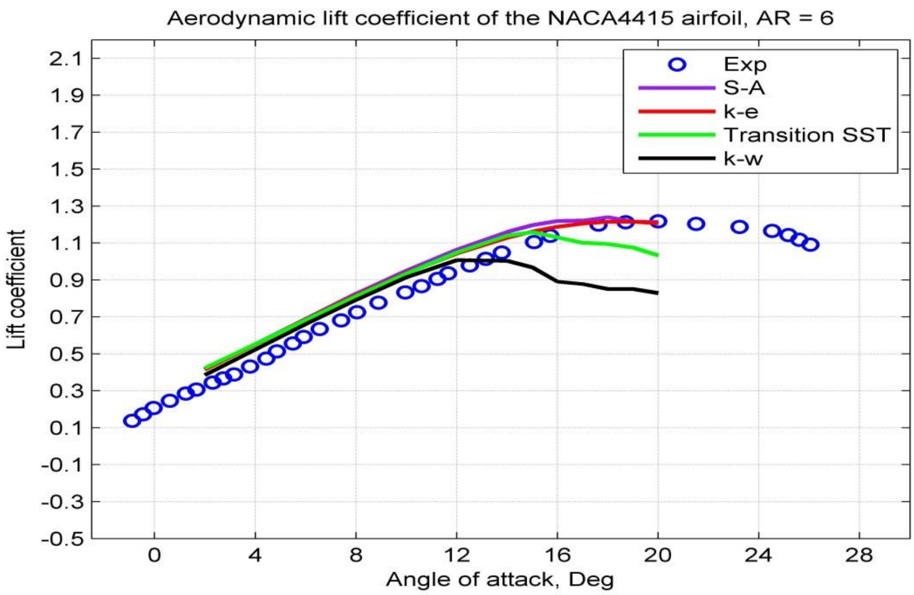

Figure 4.7 Comparison of lift coefficients with experimental data ($y^+<1$)

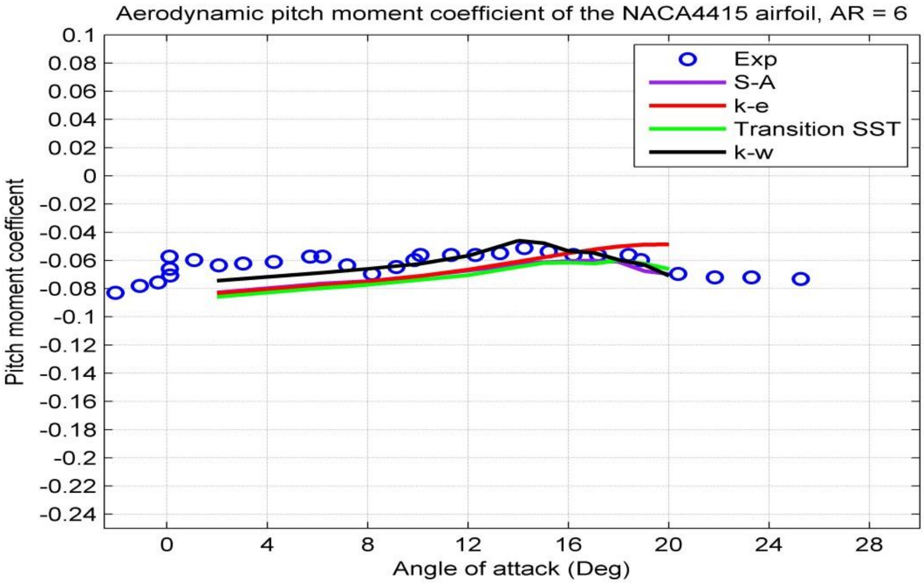

Figure 4.8 Comparison of moment coefficients with experimental data ($y^+<1$)

Figure 4.6 illustrates that almost all models give very accurate results of C_D estimation up to stall angle. However, there is a slight overestimation of C_L for all turbulence models for low angles attack, which also might stem from the bias of the experimental data. The stall angle prediction of K-ω and Transition SST models are very poor, while S-A and K-ε models give fairly accurate results in Figure 4.7. Nevertheless, the results are acceptable, especially, K-ε and S-A models capture the experimental data trend for all angle of attack values. The pitch moment coefficient results in Figure 4.8 reveal that the accuracy of all turbulence models in capturing flow behavior is a bit poor this time. Even though results are in agreement with experimental data for moderate angles of attack, they fail to capture nonlinearities of experimental data for most of the time. Besides, it is mentioned before that the y^+ value is to be kept around $y^+<1$ for capturing turbulent flow effects. The change of y^+ over the 0.305 m chord length for every mesh cross-section is shown in Figure 4.9 for 2^o angle of attack.

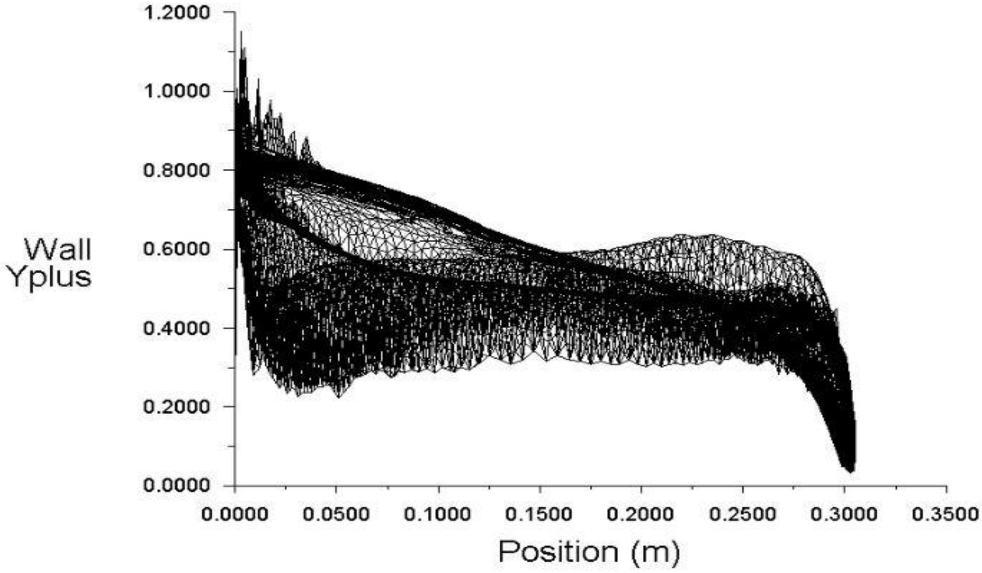

Figure 4.9 The change of y^+ over the chord of NACA 4415 wing

The pressure distribution at a slice around the midspan the NACA 4415 wing is illustrated in Figure 4.10.

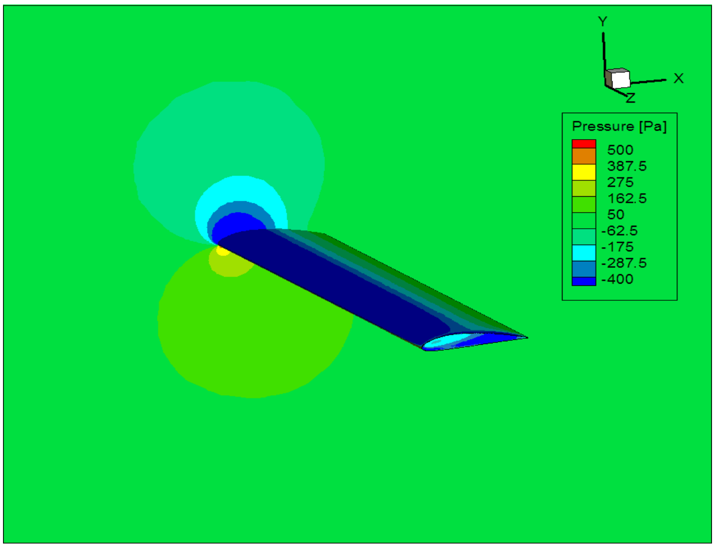

Figure 4.10 NACA 4415 wing and pressure distribution around midspan y^+<1

Furthermore, the total simulation time needed by each turbulence model to converge is given in Figure 4.11. K-ω model is the least demanding and Transition SST model is the most demanding as it is a 4-equation turbulence model. Even though S-A is a one-equation model, the simulation time is higher compared to 2-equation turbulence models. This is due to the fact that S-A model required a higher number of iteration number to converge.

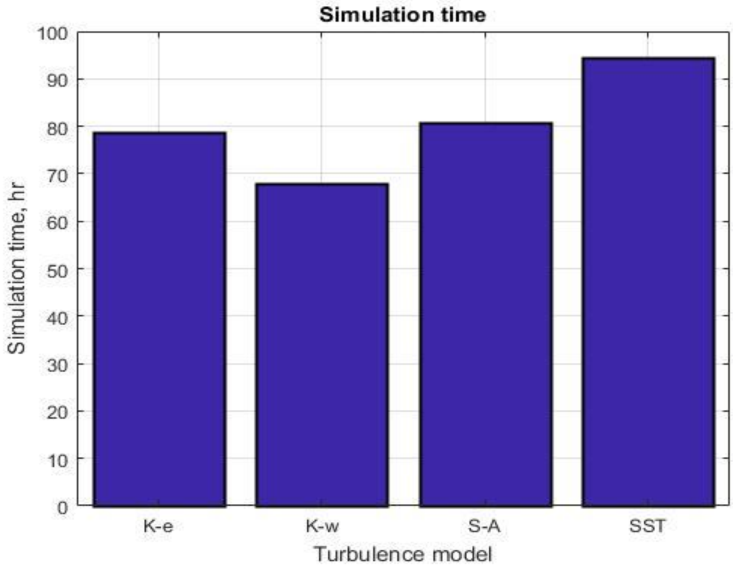

Figure 4.11 The comparison of simulation time for turbulence models

The numerical analysis is performed on 32 core process 128 GB RAM computer with 2.90 GHz processor speed. It is now clear that CFD analysis requires very high computational time for a simple wing configuration. Since tandem wing UAV has a relatively more complex airframe than a NACA4415 wing, the same analysis is repeated for $y^+<40$. The purpose is to reduce computational time and yet obtained similar accuracy such that tandem wing UAV CFD analysis will not result in enormous simulation time. In this way, more design configurations and more angle of attack values could be analyzed in the later design process.

i) $y^+<40$

Under the same test conditions given in Table 4.3, the analysis is repeated but using the wall functions this time. The first cell height is determined through Eqn. (4.13) and Eqn. (4.16).

$$C_f = 0.058 * \mathrm{Re}^{-0.2} = 0.0042 \tag{4.13}$$

$$\tau_w = \frac{1}{2}\rho V_\infty^2 C_f = 1.771 \text{ Pa/m}^2 \quad (4.14)$$

$$\mu_\tau = \sqrt{\frac{\tau_w}{\rho}} = 1.363 \text{ m/s} \quad (4.15)$$

$$y = \frac{y^+ \upsilon}{\mu_T} = 53.21866 * 10^{-2} mm \quad (4.16)$$

The grid independency test is carried out again by increasing the mesh and node numbers iteratively to identify accurate mesh resolution. The Standard k-ω turbulence model is used at 6^o angle of attack. The mesh size is enhanced until the new mesh size results in no considerable difference in drag coefficient. The test results are illustrated in Table 4.5 and in Figure 4.12 as how increment in the mesh resolution results in a convergence in drag coefficent.

Table 4.5 Grid independency test y^+<40

	Number of nodes	**Mesh cells**	C_D
Test #1	665230	1879119	0.03878
Test #2	775775	2042971	0.03889
Test #3	863934	2245133	0.03929
Test #4	992251	2452199	0.03907
Test #5	1201132	2911474	0.03936
Test #6	1362640	3188577	0.03911
Test #7	1525867	3475552	0.03890
Test #8	1690544	3771133	0.03890

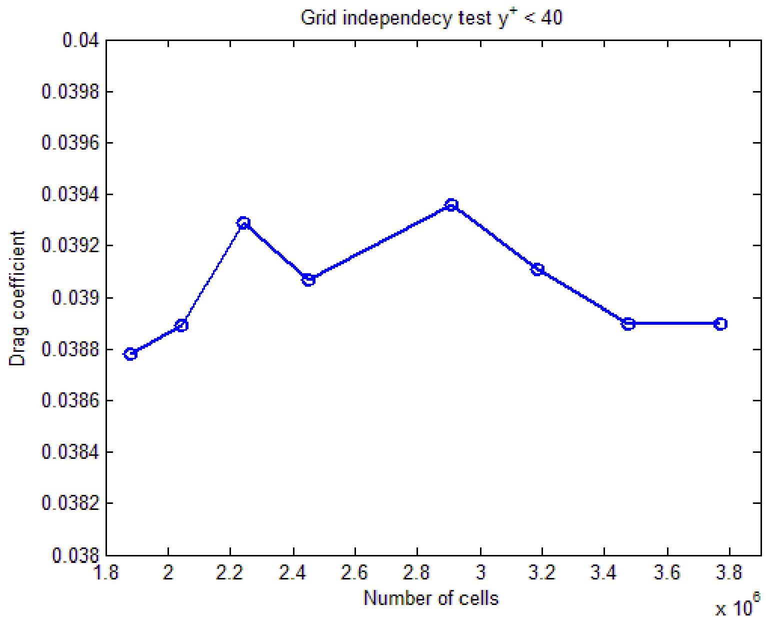

Figure 4.12 Grid independency test $y^+<40$

According to Table 4.5, it is decided to use the mesh resolution in Test #7, which corresponds to approximately 3.5 million mesh cells.

Similar to the previous case, numerical analysis is performed for each turbulence model and various angles of attack. The comparison plots of drag coefficient, lift coefficient and pitching moment coefficient with experimental data are shown in Figure 4.13, Figure 4.14 and Figure 4.15, respectively.

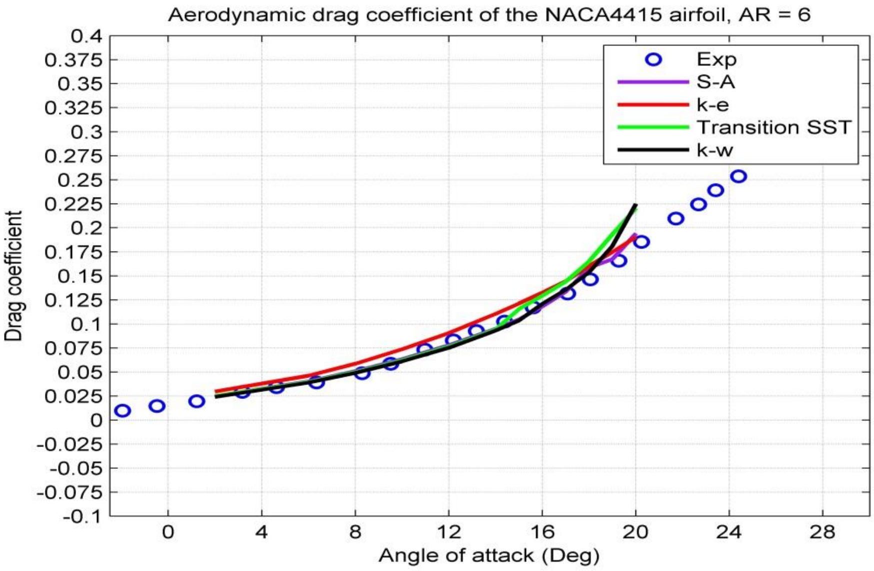

Figure 4.13 Comparison of drag coefficients with experimental data (y^+<40)

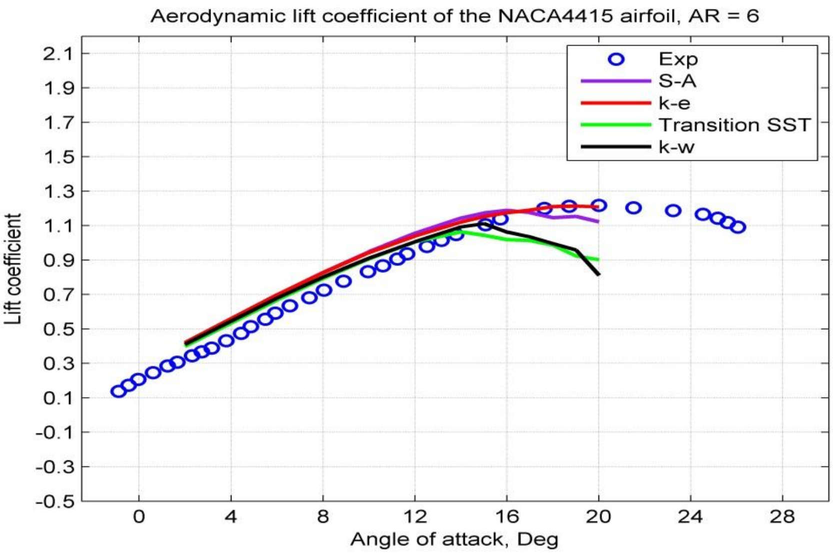

Figure 4.14 Comparison of lift coefficients with experimental data (y^+<40)

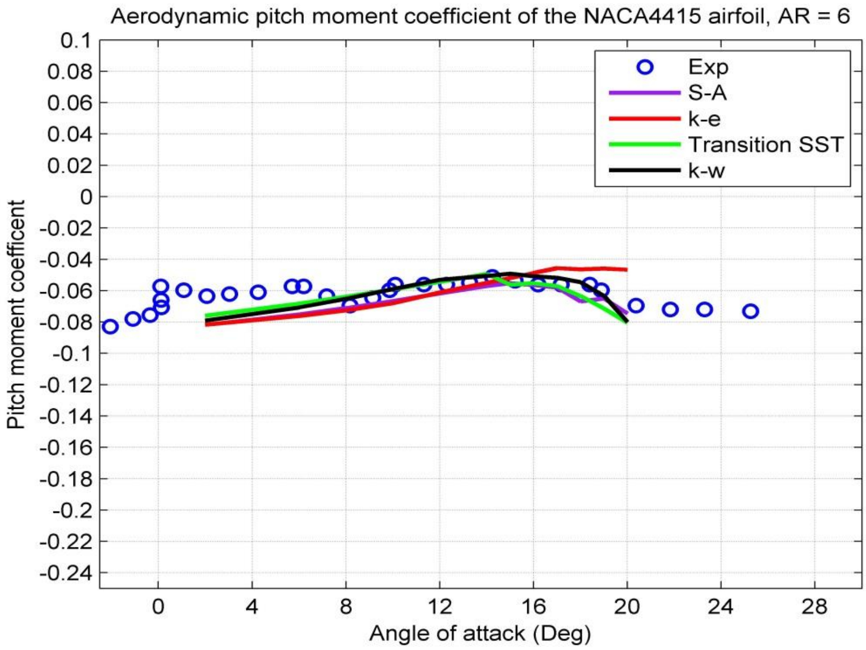

Figure 4.15 Comparison of moment coefficients with experimental data ($y^+<40$)

The results are very similar to the case where $y^+<1$. Figure 4.13 shows that almost all models give very accurate results of C_D estimation up to stall angle. A slight overestimation of C_L for all turbulence models for low angle attack values still exists. Similarly, the stall angle estimation for K-ω and Transition SST models are very poor, while S-A and K-ε models give fairly accurate results in Figure 4.14. The pitch moment comparison in Figure 4.15 reveals that moment coefficients for different turbulence models are still parallel to $y^+ <1$ case in terms of capturing flow behavior. Besides, the y^+ value is to be kept around $y^+<40$ in order to use standard wall functions. The change of y^+ over the 0.305 m chord length for every mesh cross-section is shown in Figure 4.16 for 2^o angle of attack for the consistency of analysis.

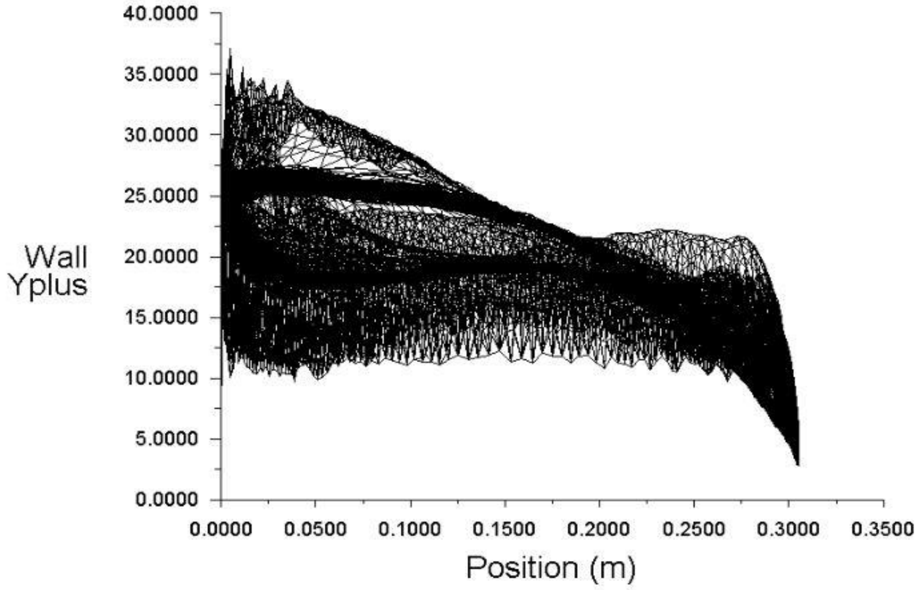

Figure 4.16 The change of y^+ over the chord of NACA 4415 wing

The pressure distribution at a slice around the midspan the NACA 4415 wing is illustrated in Figure 4.17.

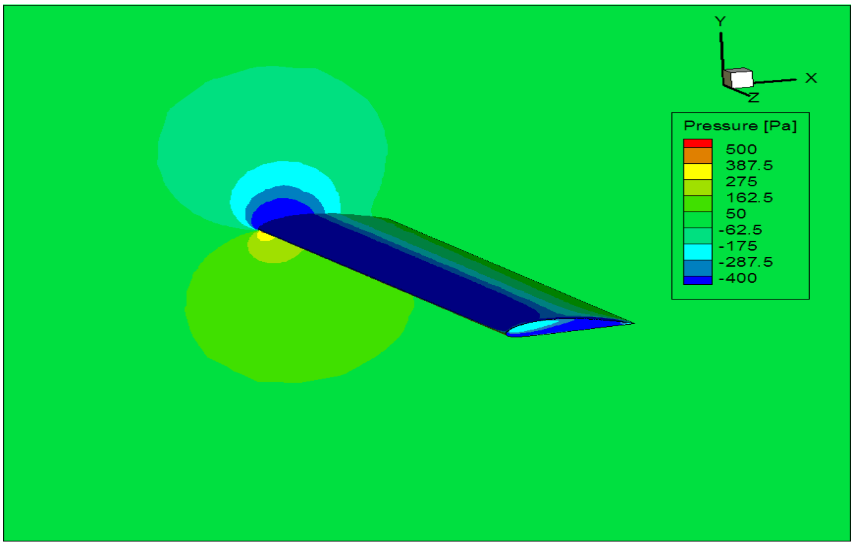

Figure 4.17 NACA 4415 wing and pressure distribution around midspan y^+<40

Finally, the total simulation time needed by each turbulence model is plotted on to Figure 4.11 for comparison as shown in Figure 4.18.

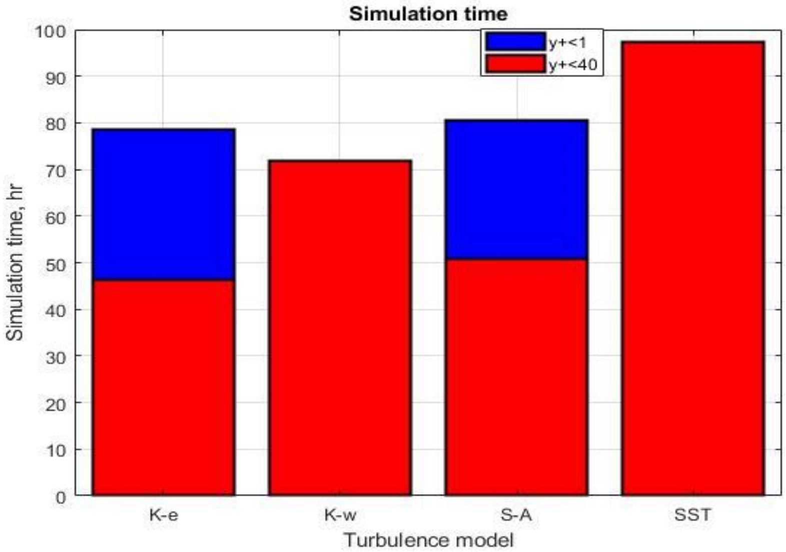

Figure 4.18 The comparison of simulation time for the cases $y^+<1$ (blue) and $y^+<40$ (red)

From Figure 4.18, there is a 41% reduction in time for K-ε turbulence model. There is also a reduction in simulation time for S-A model, however, it is not the case for the other turbulence models. This stems from the fact that K-ω and SST turbulence models are not able to predict stall angle well. The analysis around the stall angle takes too many iterations which results in very high computational time to achieve convergence.

The concept of coefficient of determination denoted by R^2or RMS error methods can be used to test how accurate the CFD results are for the cases $y^+<1$ and $y^+<40$. In statistics, the R^2 is used to determine how well a model fits a data set of observations/predictions, especially when comparing models (Devore, 1995). The values of R^2 is between $0 \leq R^2 \leq 1$ and it is calculated as shown in Eqn. (4.17):

$$R^2 = 1 - \frac{\sum(y-\hat{y})^2}{\sum(y-\bar{y})^2} \tag{4.17}$$

Another parameter that shows the error between the true data and the estimation value is Root Mean Square Error (RMSE):

$$RMSE = \sqrt{\frac{\sum (y-\hat{y})^2}{N}} \qquad (4.18)$$

The Eqn. (4.17) and Eqn.(4.18) are used to calculate the degree of accuracy of K-ε turbulence model for the cases $y^+<1$ and $y^+<40$. The accuracy of the lift and drag coefficient estimations are as shown in Table 4.6

Table 4.6 Accuracy comparison of lift and drag coefficients

Lift	R^2	*RMSE*
Lift coefficient $y^+<1$	0.940	0.067
Lift coefficient $y^+<40$	0.937	0.069
Drag	R^2	*RMSE*
Drag coefficient $y^+<1$	0.965	0.009
Drag coefficient $y^+<40$	0.946	0.011

Table 4.6 illustrates that the increase in y^+ value does not cause substantial erroneous results. Considering the accuracy and the computational time for the cases $y^+<1$ and $y^+<40$, The K-ε model with $y^+<40$ is a reasonable selection for the further CFD analysis of tandem wing UAV.

4.3.3. Tandem Wing UAV Numerical Analysis

4.3.3.1. Tandem wing UAV Mesh Studies

Tandem wing UAV design space, which has been determined previously, is also repeated here in Table 4.7. The wing configurations in Table 4.7 are generated parametrically in ANSYS Design Modeler and imported to FLUENT for meshing and CFD analysis.

Table 4.7 Tandem wing design space

The leading edge location of the front wing, mm	$X_{frontLE}$ = [170 220 270 320 370 420]
The aspect ratio of the front wing	AR_{rear} = [6]
The leading edge location of the rear wing, mm	X_{rearLE} = [dependent on AR_{rear}]
The aspect ratio of the rear wing	AR_{rear} = [5 6 7]

The numerical analyses are performed in the cruise condition. The corresponding flight condition characteristics during the cruise are shown in Table 4.8.

Table 4.8 Tandem wing cruise flight condition

	Reynolds Number	Velocity (m/s)
Flight Condition	390,000	34

In order to resolve the boundary layer flow, i.e. viscous sublayer, and to capture gradients in the solution variables, y^+ value is kept as $y^+<1$ around the surface of the UAV as in the case of NACA 4415 wing in Section 4.3.2. The first cell height is calculated as:

$$C_f = 0.058 * \mathrm{Re}^{-0.2} = 0.0044 \tag{4.19}$$

$$\tau_w = \frac{1}{2}\rho V_\infty^2 C_f = 3.266 \text{ Pa/m}^2 \tag{4.20}$$

$$\mu_\tau = \sqrt{\frac{\tau_w}{\rho}} = 1.645 \text{ m/s} \tag{4.21}$$

$$y = \frac{y^+ \upsilon}{\mu_T} = 0.91 * 10^{-2}\, mm \tag{4.22}$$

The grid independency test is carried out by increasing the mesh and node numbers iteratively to identify accurate mesh resolution. In the tandem wing CFD analysis, only half of the UAV is modeled in the design modeler and the XY plane is defined as a symmetry plane. The finer mesh is used around the leading and trailing edges of the wings and higher number of cells is employed close to the surface at each test. The Standard K-ε turbulence model is used. The mesh size is enhanced until the new mesh size results in no considerable difference in the drag coefficient. The test results are illustrated in Table 4.9 and in Figure 4.19.

Table 4.9 The Grid independency test for tandem wing UAV

	Number of nodes	**Mesh cells**	C_D
Test #1	445435	1386557	0.148511
Test #2	591233	1670279	0.147971
Test #3	732345	1936801	0.147944
Test #4	840797	2143771	0.148268
Test #5	944259	2351002	0.147771
Test #6	1140465	2762519	0.147783
Test #7	1320326	3130753	0.147544

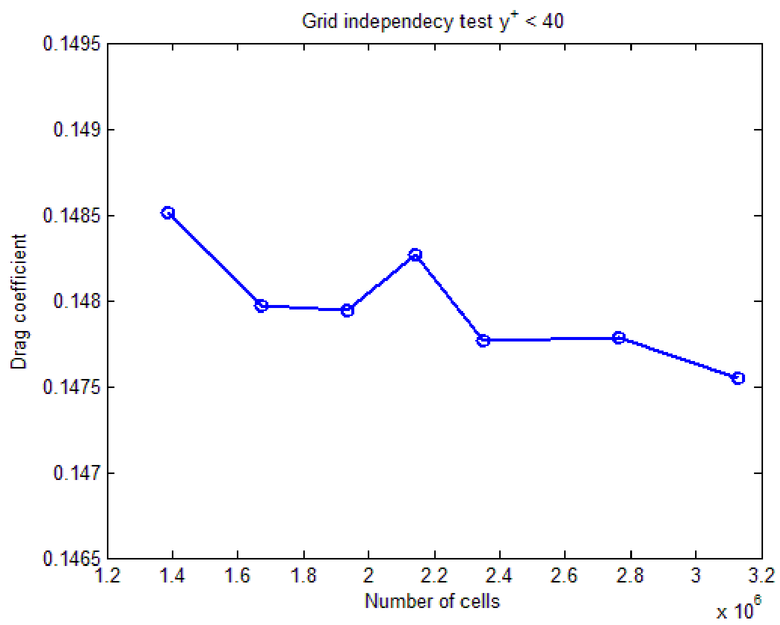

Figure 4.19 The Grid independency test for tandem wing UAV

From the Table 4.9, it is reasonable to use mesh resolution in Test #5 for further tandem wing analysis. The resulting tandem wing UAV model and detailed mesh resolution is illustrated through Figure 4.20 to Figure 4.24

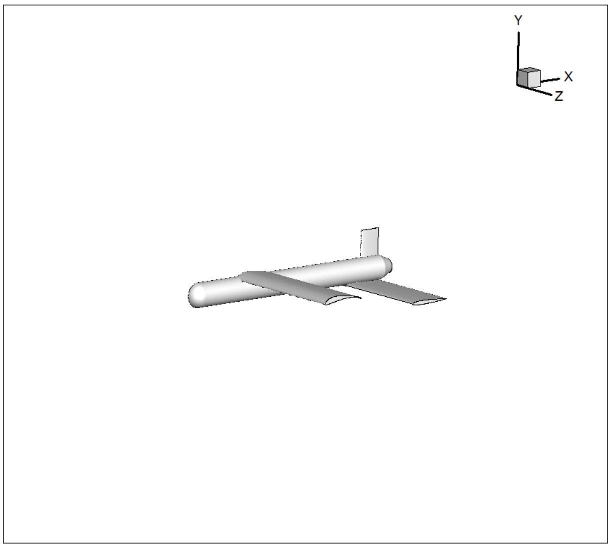

Figure 4.20 Proposed tandem wing UAV drawings

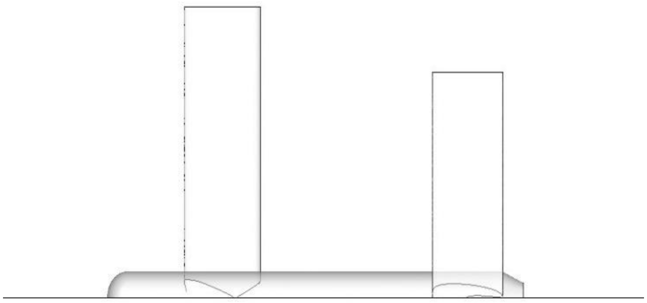

Figure 4.21 Proposed tandem wing UAV drawings

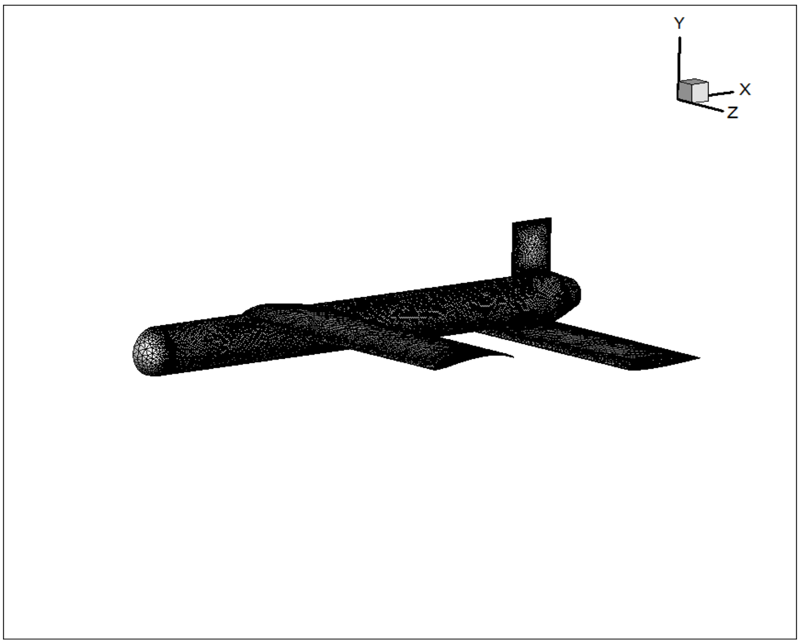

Figure 4.22 Mesh domain on the Tandem Wing UAV

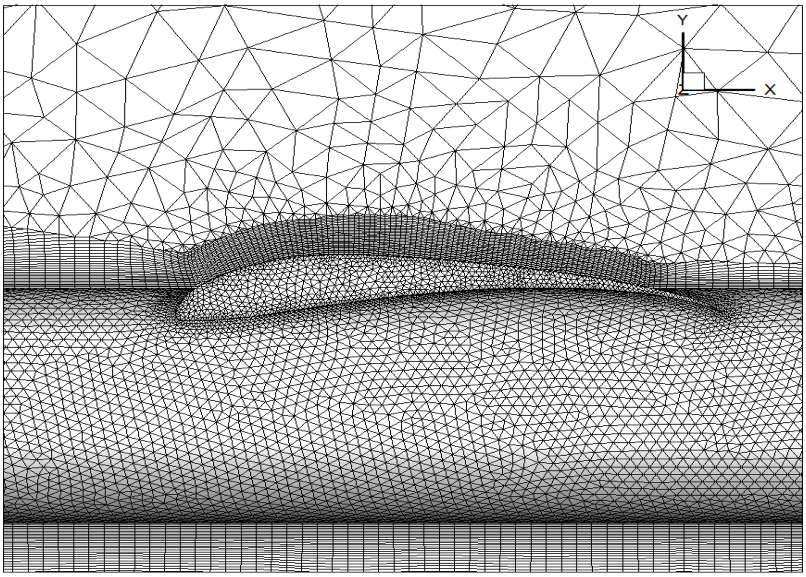

Figure 4.23 A closer look at the mesh around the front wing

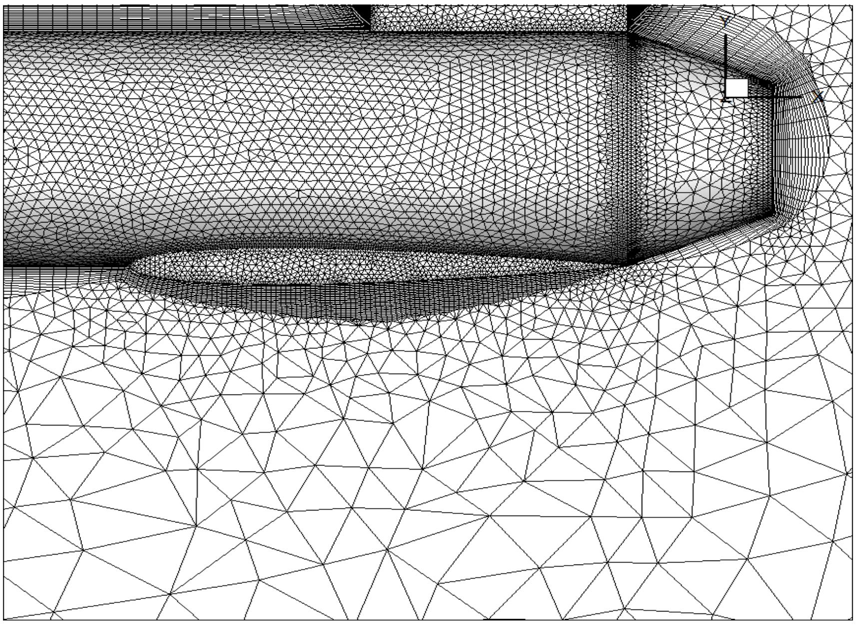

Figure 4.24 A closer look at the mesh around the rear wing

4.3.3.2. CFD Results of Alternative Tandem Wing Configurations

Firstly, numerical analysis is performed for the UAV having the rear wing $A\mathrm{R} = 5$ for various angles of attack. The plots of drag coefficient, lift coefficient and pitching moment coefficient at the center of gravity of the aircraft for six different aircraft configurations are shown in Figure 4.25, Figure 4.26, and Figure 4.27, respectively.

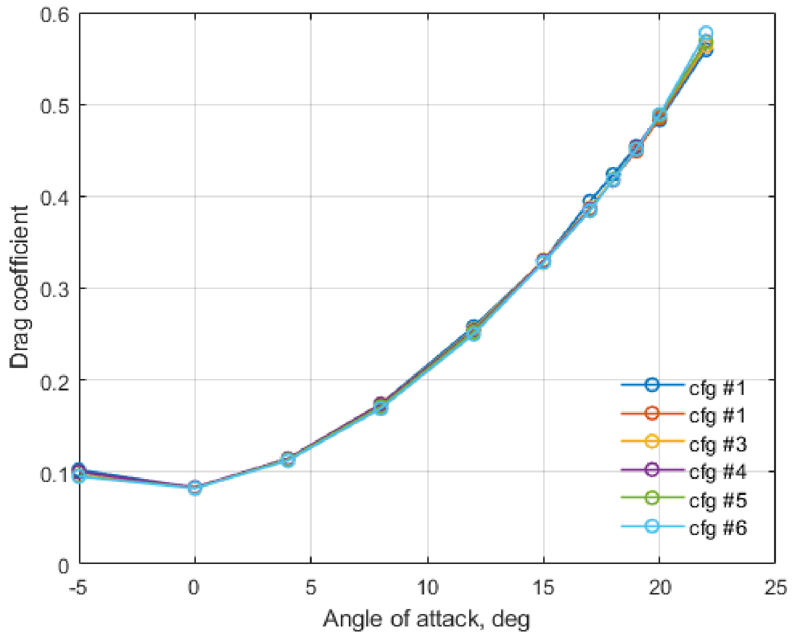

Figure 4.25 Drag coefficients for 6 different UAVs having rear wing AR = 5

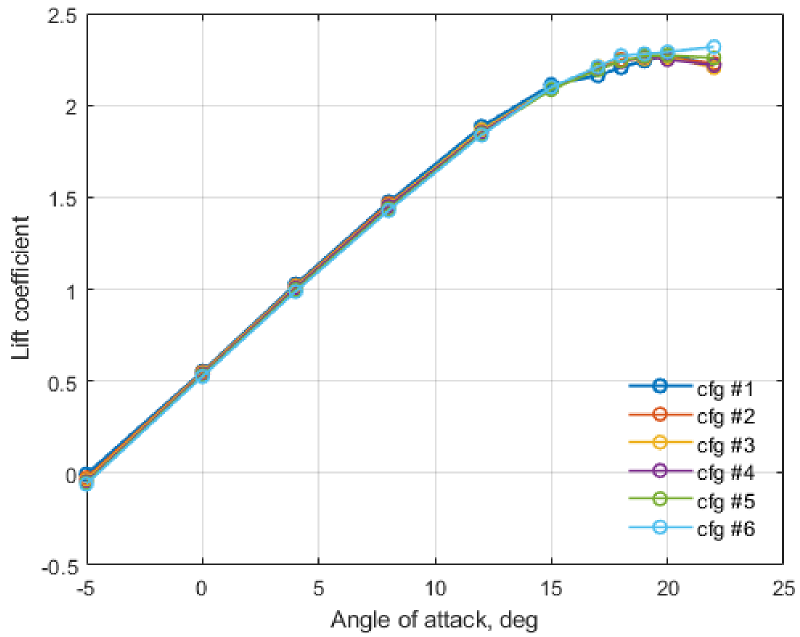

Figure 4.26 Lift coefficients for 6 different UAVs having rear wing AR = 5

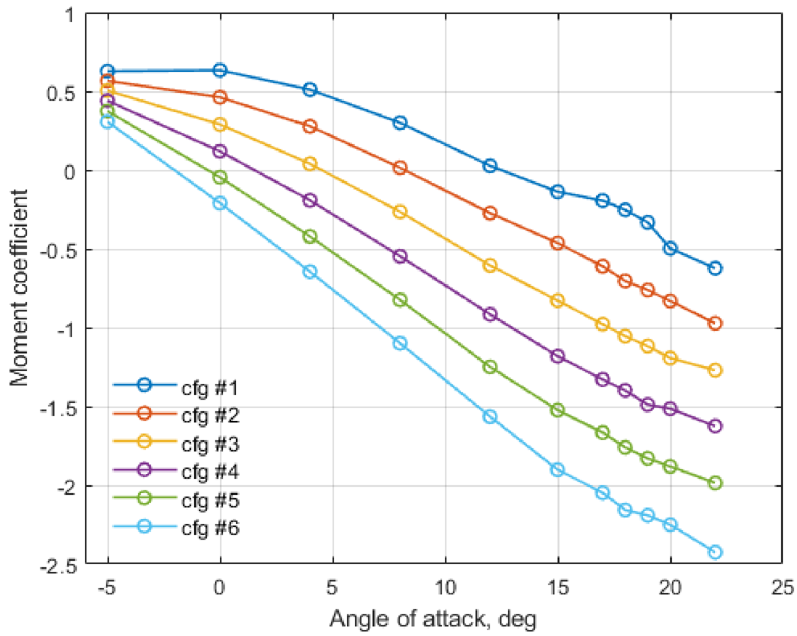

Figure 4.27 Moment coefficient at center of gravity for 6 different UAVs having rear wing AR = 5

From Figure 4.25 and Figure 4.26, it is deduced that there is no obvious improvement in lift to drag ratio with changing forward wing position. The tandem wing configurations having rear wing $AR = 6$ and $AR = 7$, whose data have been shown in Appendix A, also yield the same conclusion that there is no significant alteration in terms of lift and drag coefficients with changing front wing position. Moreover, the wake of the front wing starts to affect the rear wing as the front wing moves forward in Figure 4.27. Figure 4.27shows the pitching moment characteristics at the center of gravity of UAV calculated with respect to Table 4.2. This phenomenon results in nonlinear pitching moment characteristics as the front wing gets closer to the nose of the UAV.

Furthermore, the stability characteristics of each UAV design are analyzed with respect to the rear wing aspect ratio in Figure 4.28. It is observed that slenderer rear wing shifts aerodynamic center aft, which results in higher static margin values.

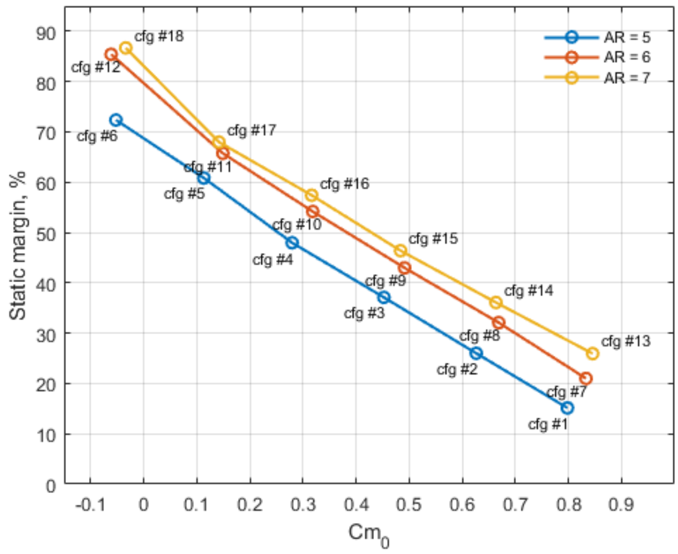

Figure 4.28 Stability characteristics of UAV design space

On the other hand, highly stable aircraft in the longitudinal plane requires a larger control surface (i.e., elevator) or longer control surface moment arm in order to perform the desired maneuver. In other words, while the stability features of an aircraft are improved, its controllability features are degraded. It is also desirable to trim aircraft at cruise or perform a maneuver with small control surface deflections. Considering that the trim C_L at cruise condition is obtained around zero degrees angle of attack and launching from the tube will require high elevator deflections that will cause highly turbulent flow around the rear wing, configuration #4 is selected to be the optimum aircraft configuration for the mission profile of the tandem wing UAV. In this configuration, the aircraft could be trimmed with very small elevator deflection at the cruise angle of attack and is trimmable at higher or lower angles of attack with reasonable elevator deflections.

In order to seek for the slotted wing effect, additional CFD analysis is carried out with/without the rear wing. Then, the slotted wing effect will be more obvious. Figure 4.29 shows the mentioned UAV configurations. The first pair illustrates the configuration where the leading edge of the front wing is placed 270 mm aft the nose, while, the second pair shows the leading edge is placed 547 mm aft the nose.

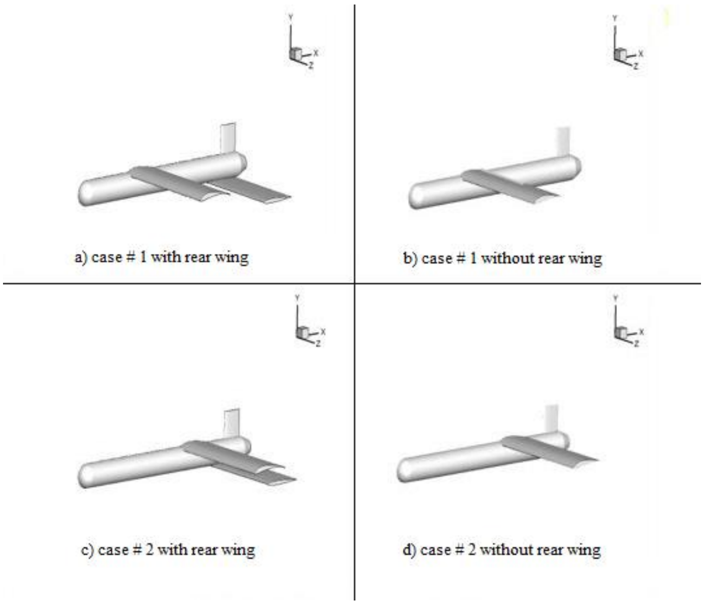

Figure 4.29 With/without rear wing slotted wing effect analysis cases

The CFD analyses are performed for each case to investigate the slotted wing effect in detail. The velocity and vorticity contours, which belong to configurations (a) and (b) in Figure 4.29, are shown in Figure 4.31 and Figure 4.32, respectively. While velocity and vorticity contours of the configurations (c) and (d) in Figure 4.29 are given in Figure 4.33 and Figure 4.34, respectively. Besides, the contours are taken at the midspan wing location illustrated in Figure 4.30.

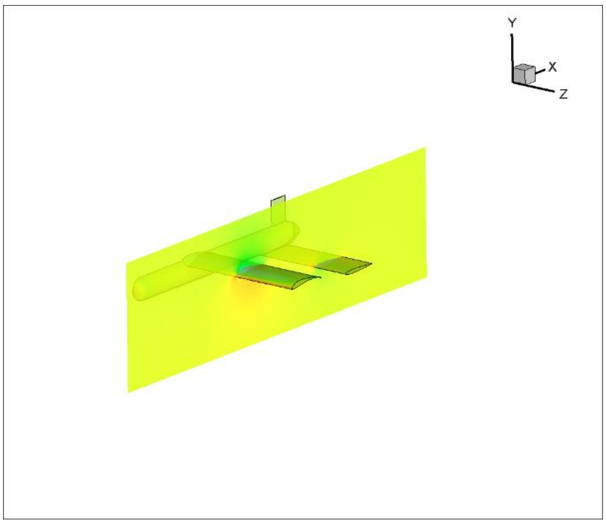

Figure 4.30 Crosssection at the midspan wing location

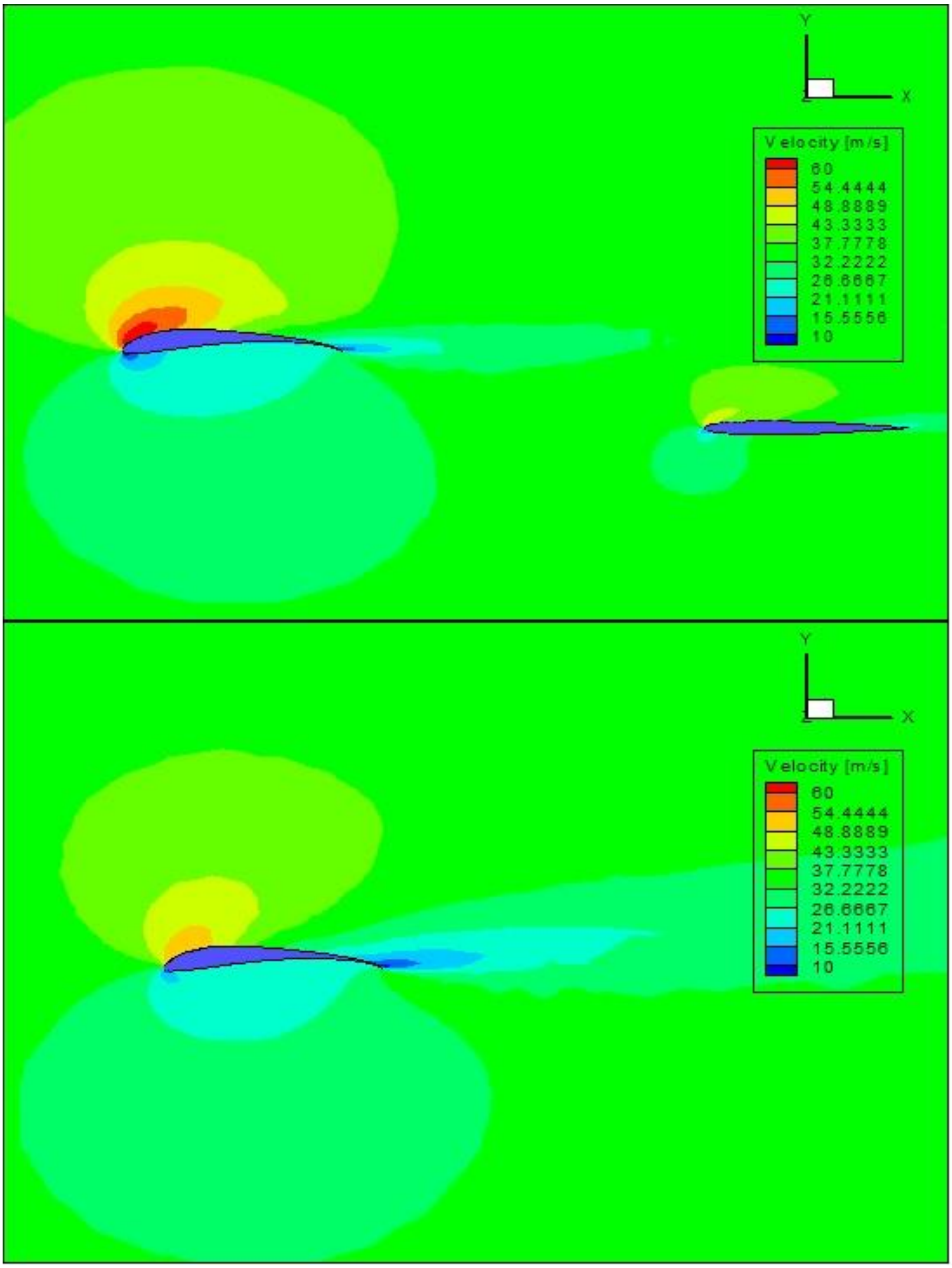

Figure 4.31 Velocity contours with/without rear wing effect in case (a) and (b)

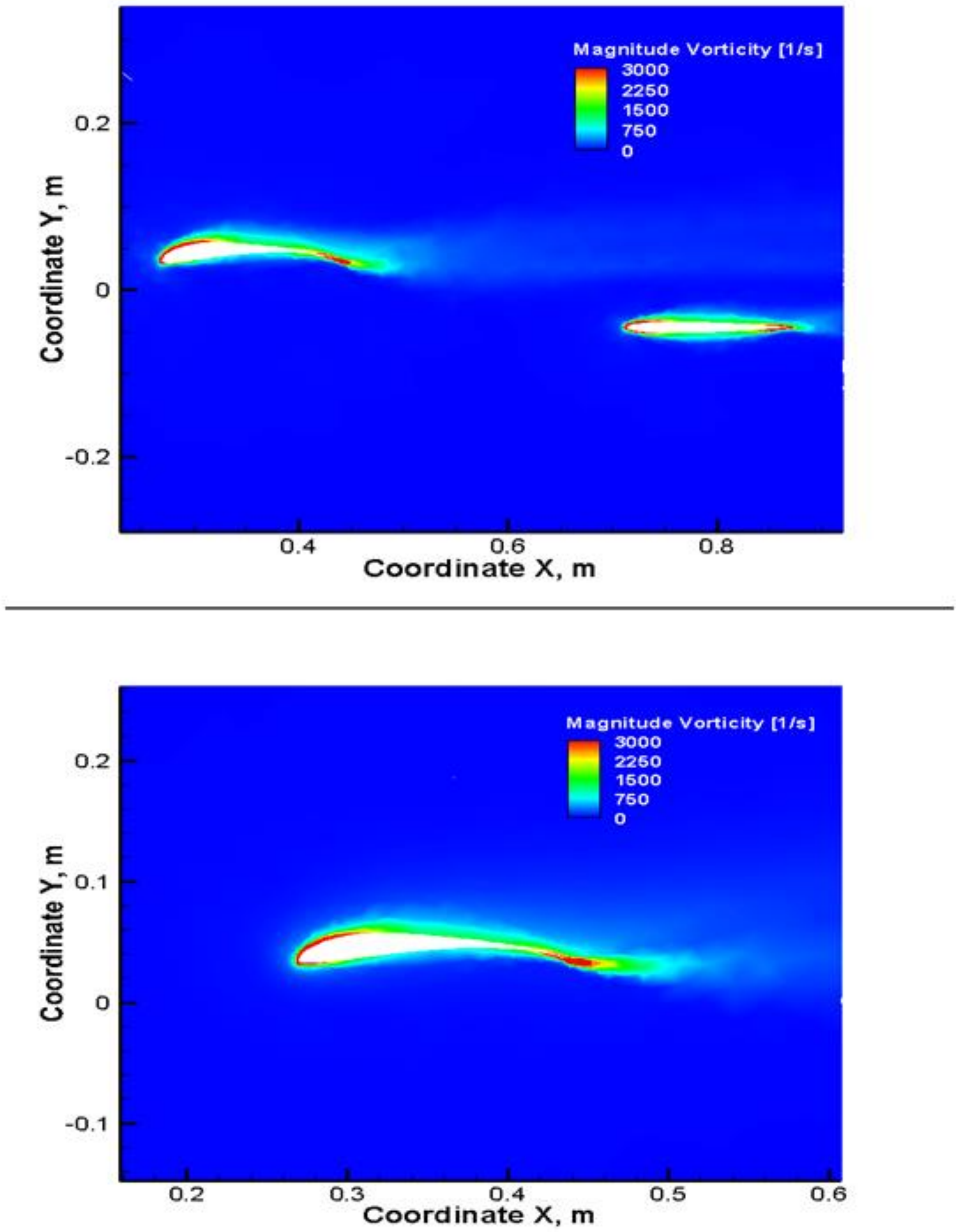

Figure 4.32 Vorticity contours with/without rear wing effect in case (a) and (b)

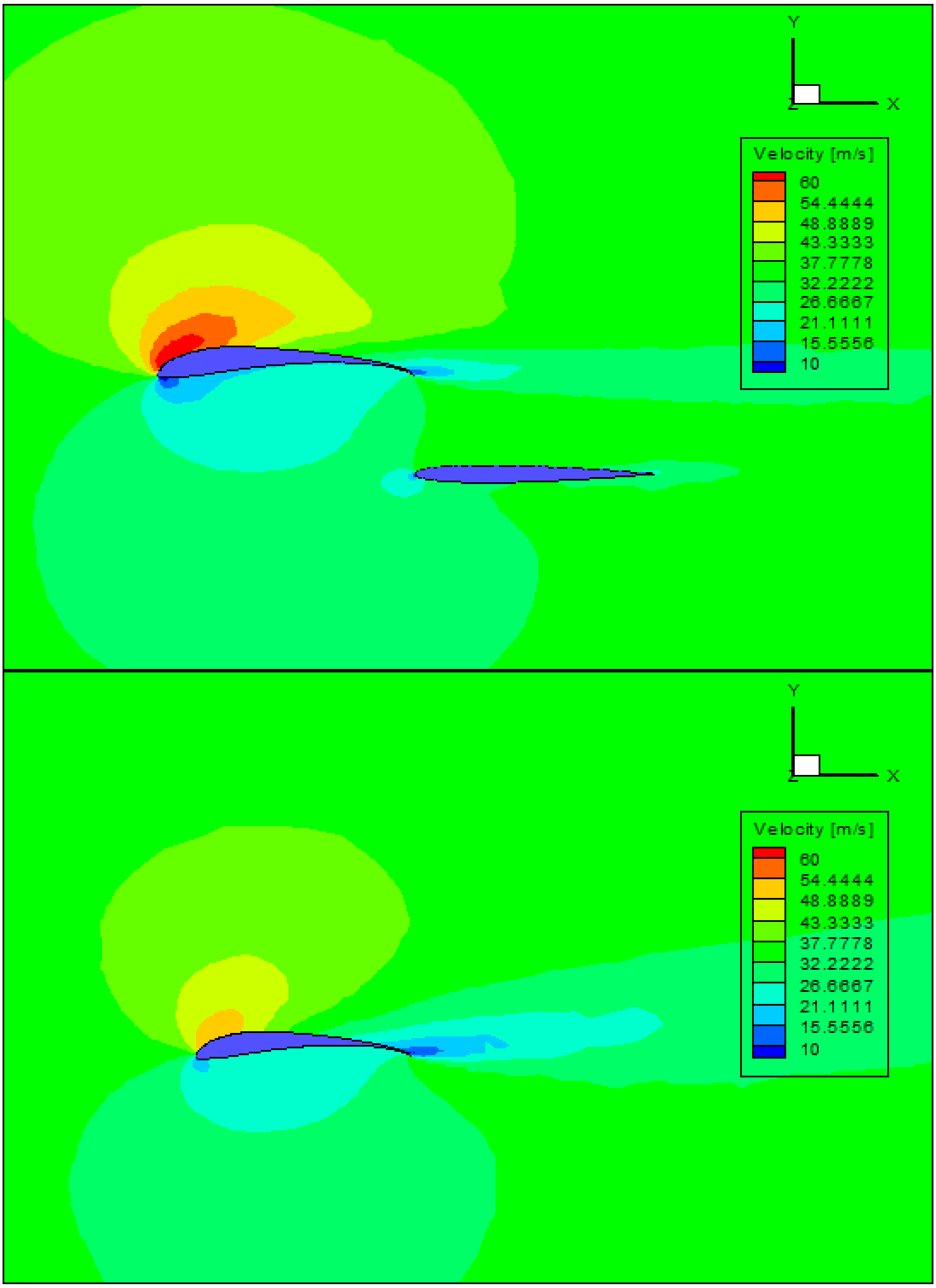

Figure 4.33 Velocity contours with/without rear wing effect in case (c) and (d)

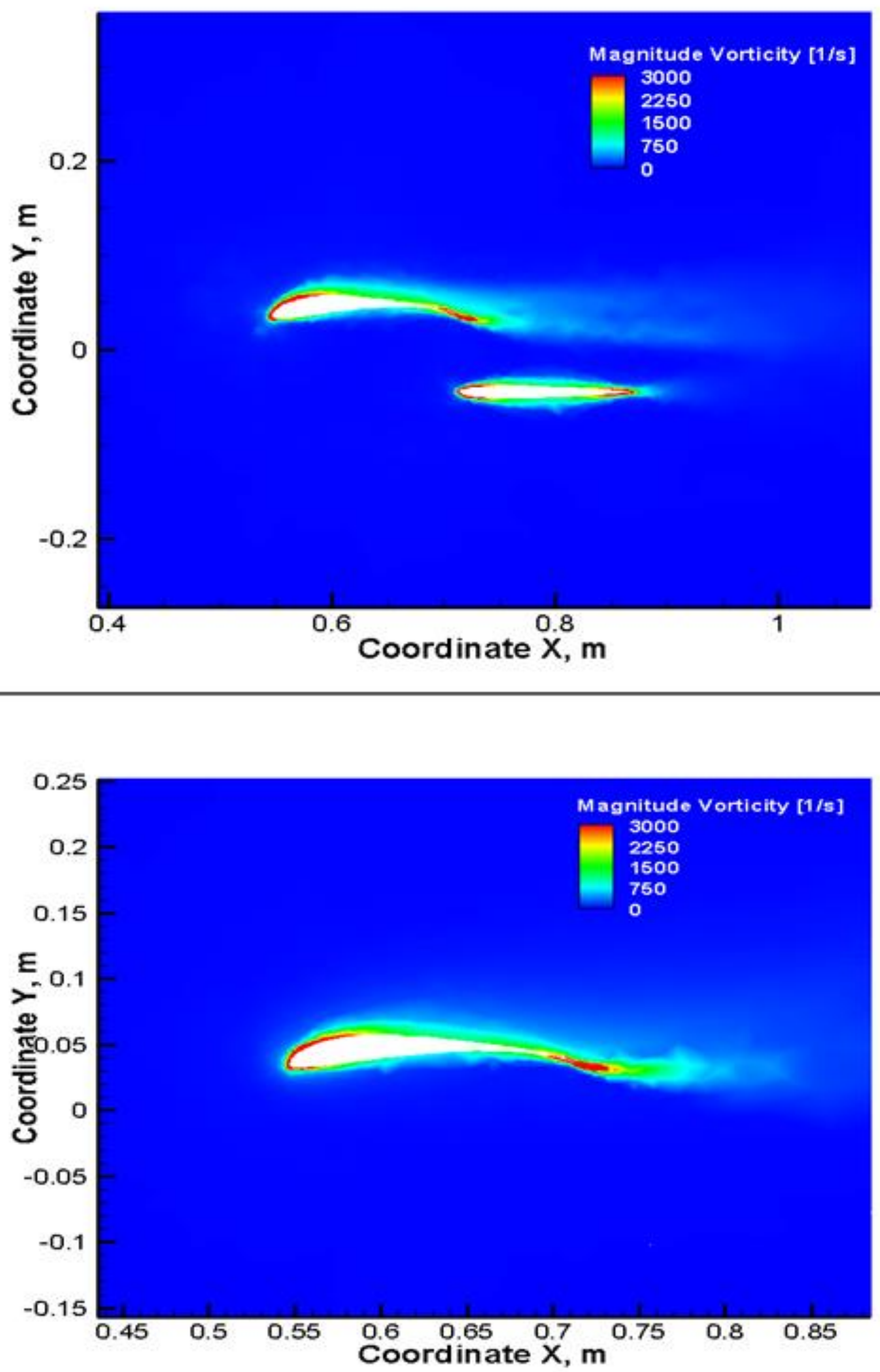

Figure 4.34 Vorticity contours with/without rear wing effect in case (c) and (d)

The air current around the front wing is affected by the circulation of the rear wing which enhances turbulence and delays flow separation caused by the high angle of attack over the front wing as it is seen from Figure 4.31 and Figure 4.33. Furthermore, the magnitude of the vorticity is relatively lower around the trailing edge of the front wing when the rear wing is present in Figure 4.32 and Figure 4.34. This also translates to fact that turbulence is healed and early separation is prevented by the aerodynamic effect of the rear wing on the front one. As the front wing gets closer to the rear wing, the lift improvement advances more especially at high angles of attack.

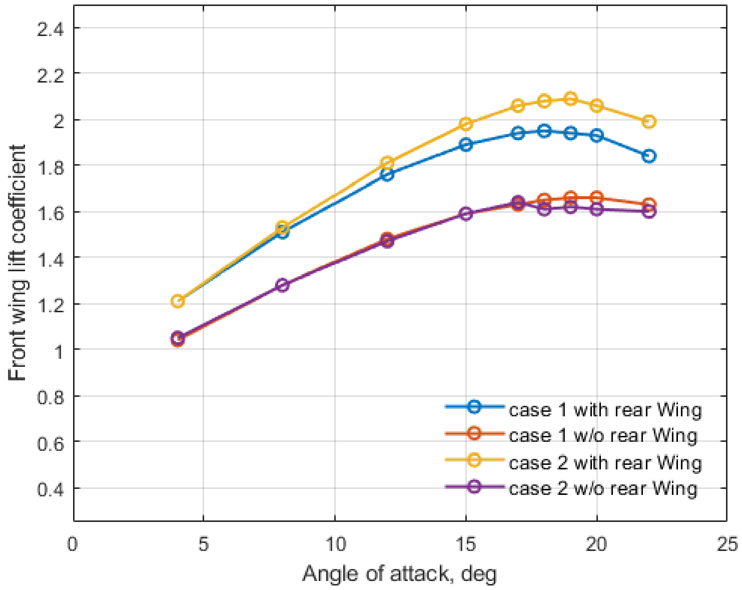

Figure 4.35 Front wing under slotted wing effect

The existence of the rear wing is more obvious in Figure 4.35. The slotted wing effect improves turbulence characteristics over the front wing and wing stays effective for larger deflections. The improvement in turbulence is also reflected in the lift coefficient at the same test condition (same Reynolds number and angle of attack). The relative location of the wings affects the degree of the slotted wing effect, hence, the lift of the wing especially at high angles of attack where flow separation is high over the wing. The closer the wings get to each other; the higher lift coefficient is achieved. Thus, it can be concluded that the slotted wing effect is already effective and present for all the alternative aircraft configurations in Figure 4.26.

4.3.3.3. Aerodynamic Database Generation of the Final Configuration

Aerodynamic database is generated for the selected UAV configuration #4 shown in Figure 4.36 for various control surface deflections and flight speeds.

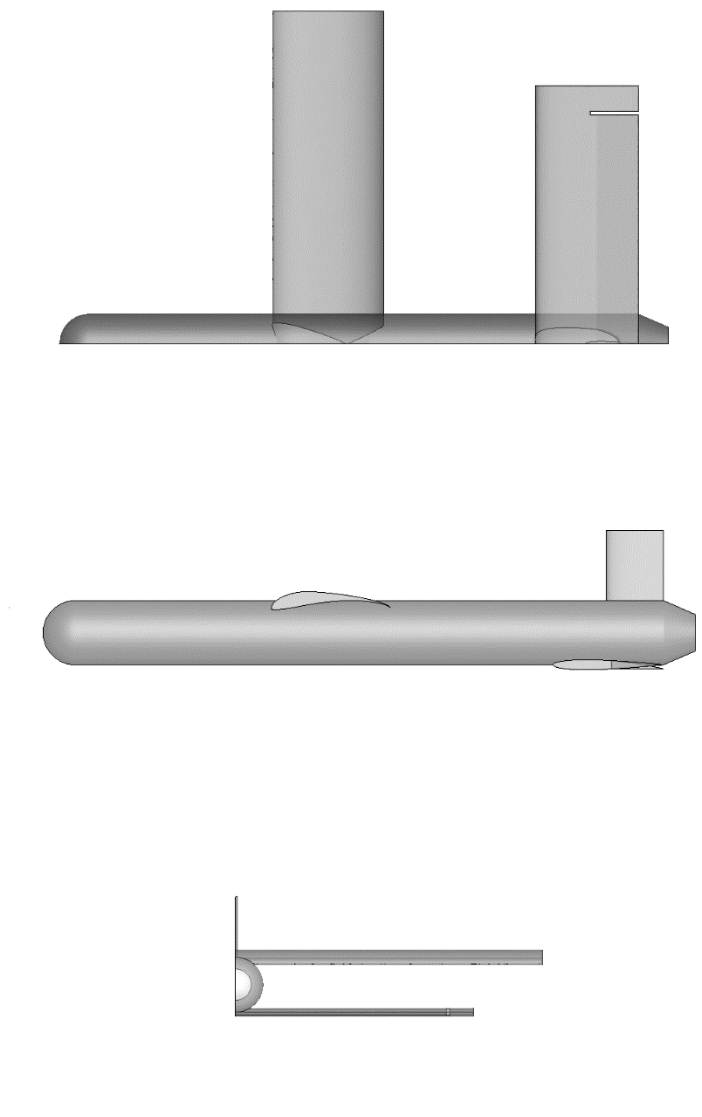

Figure 4.36 Final tandem wing configuration templates

The space of design points of the database is illustrated in Table 4.10.

Table 4.10 Aerodynamic database design points

Flight conditions	
Flight speed, m/s	$V = [17\ 34\ 51]$
Angle of attack, deg	$\alpha = [-4\ 0\ 4\ 8\ 12\ 15\ 17]$
Elevator deflection, deg	$\delta_e = [\ -10 - 5\ 0\ 5\ 10]$

The design of control surfaces is dictated by the control derivatives. Basically, the control derivative is the rate of change of aerodynamic force or moment with respect to change in control surface deflection. The geometry sizing of the elevator is performed to satisfy the requirement of $C_{M_{\delta E}} < -2\ 1/rad$. The typical values for the geometry of control surfaces are provided Sadraey's book and in Table 4.11 as well.

Table 4.11 Typical values for the sizing of the elevator

Control surface	Control surface area/lifting surface area	Control surface span/lifting surface span	Control surface chord/lifting surface chord
Elevator sizing	$S_E/S_h = 0.15 - 0.4$	$b_E/b_h = 0.8 - 1$	$c_E/c_h = 0.2 - 0.4$

The shift in the pitch moment coefficient can be observed through Figure 4.37 for flight speed $V = 34\ m/s$ for various elevator deflections. Previously stated requirement of control effectiveness value is satisfied by achieving control derivative as $C_{M_{\delta E}} \approx -4\ 1/rad$.

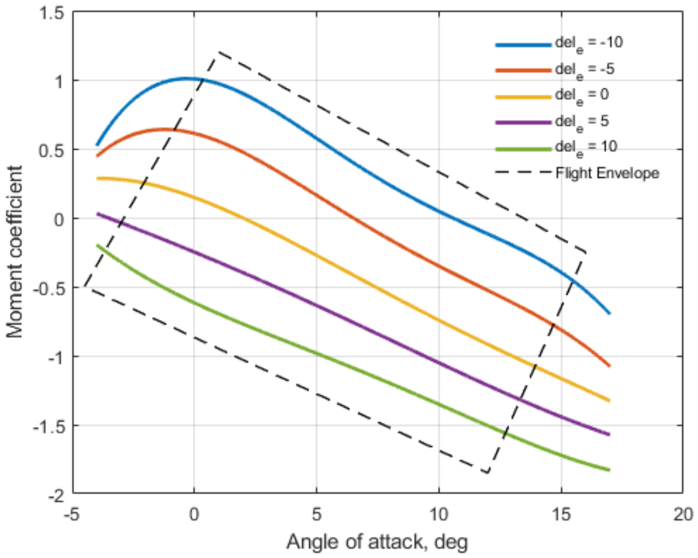

Figure 4.37 The change in moment coefficient at center of gravity with elevator deflection at $V = 34\ m/s$

In Figure 4.37, predicted flight envelope is shown. This can be interpreted as when the elevator is deflected upward (-) pitch up nose moment causes aircraft to fly at positive angles of attack while downward deflection (+) causes pitch down nose moment making aircraft fly at negative angles of attack. By this analogy, aircraft is expected to fly in linear flight envelope except for highly transient maneuvers.

The drawback of the tandem wing design is also shown in the pitching moment diagram above. The aircraft is more prone to be affected by the wake of the forward wing. Control effectiveness at negative angles of attack and negative elevator deflections degrades severely compared to monoplane design as the size of the rear wing is larger in tandem configuration. However, it is ensured that this flight condition is out of the flight envelope under normal conditions.

Furthermore, drag polar at the same flight condition is represented in Figure 4.38 which will form the aerodynamic database later in flight simulation studies.

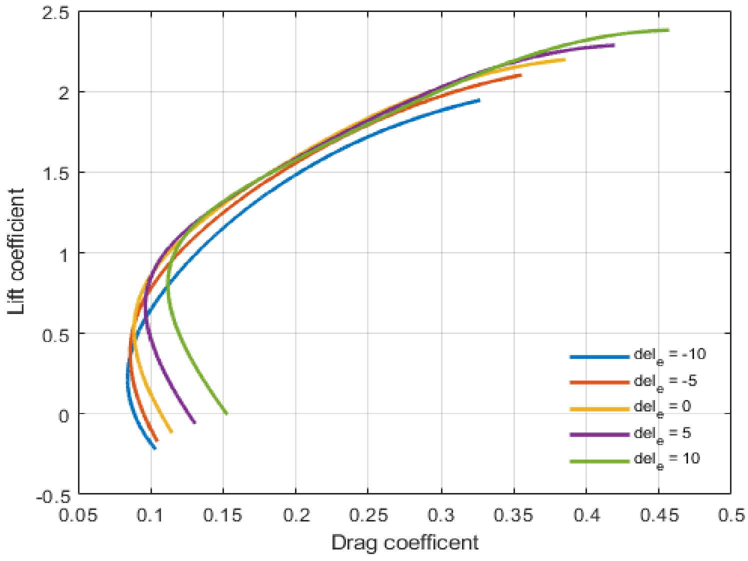

Figure 4.38 The drag polar at $V = 34\ m/s$

CHAPTER 5

CONTROLLER DESIGN & FLIGHT SIMULATION ANALYSIS

5.1. Purpose

The motion of the UAV in six freedom degrees is controlled through an autopilot onboard. Autopilot produces commands for the motor throttle and the deflection of aerodynamic control surfaces in order to perform necessary turns dictated by the guidance algorithm. The stability of the system can also be adjusted by the autopilot design based on the performance requirements (Avcıoğlu, 2000).

The tandem wing UAV, which has been designed aerodynamically, is employed for reconnaissance and surveillance purposes. Thus, designing pitch attitude autopilot for climb and decline; normal acceleration and altitude hold controllers to sustain flight at desired altitude are necessary considering the classical mission profile in Figure 2.1. The attitude hold, normal acceleration, and altitude hold autopilot configurations are discussed in subsequent sections of this chapter. In the end, the designed linear autopilot configurations will be employed in the tandem wing flight simulation which involves nonlinearities in aerodynamics database, atmosphere and gravity models to test the performance of the designed controllers under simulated real life conditions.

5.2. Dynamic Model of the UAV

This research only focuses on the pitching dynamics of aircraft without causing any loss of generality for the applicability of the methods and outcome of the thesis. A brief explanation of all control channels is made for the completeness of the subject.

Since the designed UAV is similar to an aircraft rather than a missile, bank to turn is more applicable than skid to turn type maneuver. Therefore, roll and yaw dynamics of the UAV are coupled and must be handled together to achieve bank to turn or coordinated turn. In coordinated turn aircraft flies without sideslip angle, in other words, there is no lateral acceleration of the aircraft while turning. The aircraft is banked via aileron channel and the appropriate use of the rudder channel ensures that aircraft would not tend to skid to the outside of the turn maneuver. The roll attitude, yaw attitude and lateral acceleration of the aircraft is realized by the inertial navigation system and controlled through control commands from the autopilot.

In the longitudinal plane, the tandem wing UAV shall follow an assigned or predetermined altitude trajectory. The guidance algorithm dictates UAV to climb, altitude hold and descent throughout the flight phases. When the desired altitude is achieved, the guidance algorithm switches autopilot algorithms to altitude hold autopilot from attitude hold. In order to achieve sufficient accuracy, altitude information obtained from the inertial measurement system is corrected through GPS. This altitude correction is beyond the scope of this thesis, though, the design of the controllers is not effected considering both IMU and GPS have fast enough dynamics. The pitch attitude, normal acceleration, and altitude is realized by the inertial navigation system and controlled through the autopilot which will be analyzed in upcoming sections.

5.2.1. Equations of the Motion of the Aircraft

The equations of the motion of the rigid body are acquired using Newton’s second law. The derivation of the equations can be found in Nelson’s book on flight stability (Nelson, 1989). Throughout this study, tandem wing design is considered as a rigid body without aeroelastic effects, flutter, and backlash. Since this study only focuses on the longitudinal dynamics of aircraft, only the force and the moment equations in the longitudinal plane are shown in Eqn. (5.1) and Eqn. (5.2).

$$F_Z + mg\ cos\theta\ cos\phi = m\left(\dot{w} + pv - qu\right) \tag{5.1}$$

$$M = I_y\dot{q} + I_{xz}\left(p^2 - r^2\right) + rq\left(I_x - I_z\right) \tag{5.2}$$

The two dynamic equations given above are nonlinear differential equations. The variables existing in these equations are illustrated in Figure 5.1. The following assumptions are made in order to linearize the equations of the motion.

- Rolling dynamics are the fastest and there is no roll and heading rate of the aircraft, $\phi = 0,\ \mathrm{p} = 0,\ r = 0$.
- UAV is symmetric in XZ plane of body-fixed coordinate system.
- Gravitational acceleration is considered only as disturbance and not considered in the motion equations. Flight simulation analysis will involve gravitational effects and autopilot is still expected to fulfill the mission requirements.
- The x-component of velocity "u" in body-fixed coordinate system is constant.

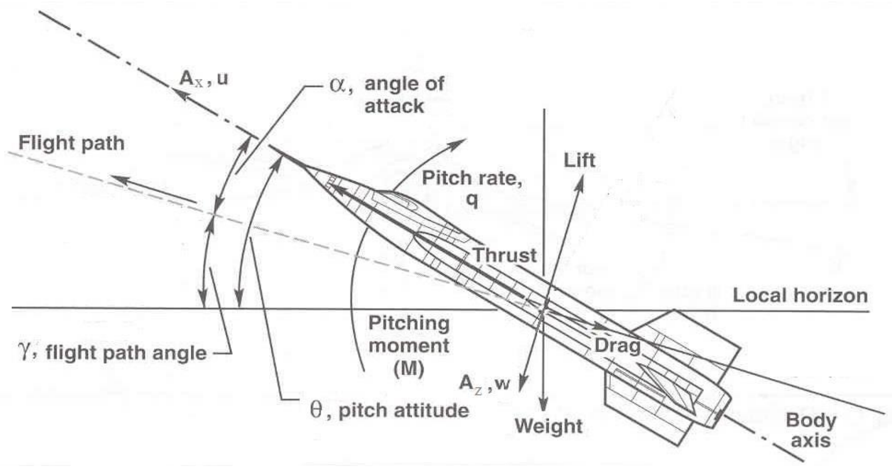

Figure 5.1 Longitudinal plane flight parameters

The Eqn. (5.1) and Eqn. (5.2) equations are simplified under the assumptions previously mentioned as:

$$\dot{w} = \frac{F_z}{m} + qu \tag{5.3}$$

$$\dot{q} = \frac{M}{I_y} \tag{5.4}$$

The small angle and the short period (i.e. constant velocity) assumptions yield:

$$\alpha = \tan^{-1}\left(\frac{w}{u}\right) \approx \frac{w}{u} \tag{5.5}$$

$$\dot{\alpha} = \frac{\dot{w}}{u} \tag{5.6}$$

$$\dot{\alpha} = \frac{F_z}{mu} + q\ . \tag{5.7}$$

The force equation can be expressed in terms of the dominant aerodynamic coefficients on the longitudinal plane as:

$$F_z = Z_\alpha \alpha + Z_q q + Z_\delta \delta + Z_o \tag{5.8}$$

$$\dot{\alpha} = q + \frac{F_z}{mu} = q + \frac{Z_\alpha \alpha + Z_q q + Z_\delta \delta + Z_0}{mu} \tag{5.9}$$

$$\dot{\alpha} = \left(\frac{Z_\alpha}{mu}\right)\alpha + \left(\frac{Z_q}{mu} + 1\right)q + \left(\frac{Z_\delta}{mu}\right)\delta + \frac{Z_0}{mu} \tag{5.10}$$

Moment equation can also be expressed in terms of the dominant aerodynamic coefficients on the longitudinal plane as:

$$M = M_\alpha \alpha + M_q q + M_\delta \delta + M_o \tag{5.11}$$

$$\dot{q} = \frac{M}{I_y} = \frac{M_\alpha \alpha}{I_y} + \frac{M_q q}{I_y} + \frac{M_\delta \delta}{I_y} + \frac{M_0}{I_y} \tag{5.12}$$

The Eqn. (5.10) and Eqn. (5.12) involves shorthand notations of aerodynamic parameters, which already has been determined through CFD analysis in Chapter 4 for the final tandem wing design. These parameters are illustrated in Table 5.1

Table 5.1 The shorthand notation of aerodynamic parameters

$Z_\alpha = q_\infty S C_{Z\alpha}$	$Z_\delta = q_\infty S C_{Z\delta}$	$Z_q = q_\infty S C_{Zq} \frac{l_{ref}}{2V}$
$M_\alpha = q_\infty S l_{ref} C_{M\alpha}$	$M_\delta = q_\infty S l_{ref} C_{M\delta}$	$M_q = q_\infty S l_{ref} C_{Mq} \frac{l_{ref}}{2V}$

where

q_∞ : Freestream dynamic pressure, Pa

S : Reference wing area, m^2

l_{ref} : Reference chord length, m

V : Magnitude of freestream velocity, m/s

In order to express the state equations in terms of normal acceleration following conversion is executed:

$$a_z = \frac{Z}{m} = \frac{Z_\alpha}{m}\alpha + \frac{Z_q}{m}q + \frac{Z_\delta}{m}\delta + \frac{Z_0}{m} \tag{5.13}$$

$$\alpha = \frac{a_z m}{Z_\alpha} - \frac{Z_q q}{Z_\alpha} - \frac{Z_\delta \delta}{Z_\alpha} - \frac{Z_0}{Z_\alpha} \tag{5.14}$$

Inserting Eqn. (5.14) into Eqn. (5.10):

$$\dot{\alpha} = \left(\frac{Z_\alpha}{mu}\right)\left(\frac{a_z m}{Z_\alpha} - \frac{Z_q q}{Z_\alpha} - \frac{Z_\delta \delta}{Z_\alpha} - \frac{Z_0}{Z_\alpha}\right) + \left(\frac{Z_q}{mu} + 1\right)q + \left(\frac{Z_\delta}{mu}\right)\delta + \frac{Z_0}{mu} \tag{5.15}$$

Furthermore, inserting Eqn. (5.14) into Eqn. (5.12):

$$\dot{q} = \frac{M_\alpha}{I_y}\left(\frac{a_z m}{Z_\alpha} - \frac{Z_q q}{Z_\alpha} - \frac{Z_\delta \delta}{Z_\alpha} - \frac{Z_0}{Z_\alpha}\right) + \frac{M_q q}{I_y} + \frac{M_\delta \delta}{I_y} + \frac{M_0}{I_y} \tag{5.16}$$

$$\dot{q} = \left(\frac{M_\alpha m}{I_y Z_\alpha}\right)a_z + \left(\frac{M_q}{I_y} - \frac{M_\alpha Z_q}{I_y Z_\alpha}\right)q + \left(\frac{M_\delta}{I_y} - \frac{M_\alpha Z_\delta}{I_y Z_\alpha}\right)\delta - \frac{M_\alpha Z_0}{I_y Z_\alpha} + \frac{M_0}{I_y} \tag{5.17}$$

Derivative of Eqn. (5.13) with respect to time yields:

$$\dot{a}_z = \frac{Z_\alpha}{m}\dot{\alpha} + \frac{Z_q}{m}\dot{q} + \frac{Z_\delta}{m}\dot{\delta} \tag{5.18}$$

Finally, the substitution of Eqn. (5.15) and Eqn. (5.17) into Eqn. (5.18) yields:

$$\dot{a}_z = \frac{Z_\alpha}{m}\left(\begin{array}{l}\left(\dfrac{Z_\alpha}{mu}\right)\left(\dfrac{a_z m}{Z_\alpha}-\dfrac{Z_q q}{Z_\alpha}-\dfrac{Z_\delta \delta}{Z_\alpha}-\dfrac{Z_0}{Z_\alpha}\right)\\ +\left(\dfrac{Z_q}{mu}+1\right)q+\left(\dfrac{Z_\delta}{mu}\right)\delta+\dfrac{Z_0}{mu}\end{array}\right)+\frac{Z_q}{m}\left(\begin{array}{l}\dfrac{M_\alpha}{I_y}\left(\dfrac{a_z m}{Z_\alpha}-\dfrac{Z_q q}{Z_\alpha}-\dfrac{Z_\delta \delta}{Z_\alpha}-\dfrac{Z_0}{Z_\alpha}\right)\\ +\dfrac{M_q q}{I_y}+\dfrac{M_\delta \delta}{I_y}+\dfrac{M_0}{I_y}\end{array}\right)+\frac{Z_\delta}{m}\dot{\delta}$$

(5.19)

Rearranging the form in Eqn. (5.19), the final form of the normal acceleration equation is obtained as:

$$\dot{a}_z = \left(\begin{array}{l}\dfrac{Z_\alpha}{mu}\\ +\dfrac{Z_q M_\alpha}{I_y Z_\alpha}\end{array}\right)a_z + \left(\begin{array}{l}\dfrac{Z_\alpha}{m}+\dfrac{Z_q M_q}{I_y m}\\ -\dfrac{M_\alpha Z_q{}^2}{m I_y Z_\alpha}\end{array}\right)q + \left(\begin{array}{l}\dfrac{Z_q M_\delta}{m I_y}\\ -\dfrac{Z_q M_\alpha Z_\delta}{m I_y Z_\alpha}\end{array}\right)\delta + \frac{Z_\delta}{m}\dot{\delta} - \frac{Z_q M_\alpha Z_0}{m I_y Z_\alpha} + \frac{M_0 Z_q}{m I_y}$$

(5.20)

5.2.2. The Control Actuator System (CAS) Model

For the autopilot design of the tandem UAV, the control actuator system is modeled as a second-degree transfer function which is a highly preferred model for modeling the actuator systems (Ogata, 2010).

$$\frac{\delta}{\delta_{com}} = \frac{w_n^2}{s^2 + 2\zeta w_n s + w_n^2} \tag{5.21}$$

The inverse Laplace transform of the Eqn. (5.21) yields:

$$\ddot{\delta} = -2\zeta w_n \dot{\delta} - w_n^2 \delta + w_n^2 \delta_{com} \tag{5.22}$$

where

w_n : bandwidth of control actuator

ξ : damping ratio

These two parameters, which affect the system response of the mechanical systems, are considered as below typical values for the purpose of the conceptual design process. As a general design rule, the bandwidth of the CAS shall be 4 to 10 times greater than the aircraft's natural frequency in order to provide efficient stability.

$w_n = 20$ Hz

$\xi = 0.5$

The significant aspect of the actuator is that maneuvering performance of the tandem wing UAV is limited by both the linear aerodynamic region and the CAS position and angular velocity limits. Thus, during the design of autopilot, the limits of CAS must be known and should not be exceeded. The saturation limits of the CAS are assumed as follows:

CAS position limit : 15^{o}

CAS angular velocity limit: 500^{o}/s

There limitations are defined as CAS performance limits and will be imposed on the linear autopilot model and the flight simulation.

5.2.3. State Space Representation of the Dynamic Model of the UAV

In the scope of modern control analysis, previously derived equations are illustrated as state space representation. Eqns. (5.17), (5.20) and (5.22) are illustrated in this matrix form in Eqn. (5.23). The form of state space representation is as $\dot{x} = Ax + Bu$ and the output is defined as $y = Cx + Du$. Thus, the matrices in the output equation must be identified in consideration with the desired output variable and might be different for different autopilot designs even though A and B matrices will stay the

$$
\begin{bmatrix} \dot{a}_z \\ \dot{q} \\ \dot{\delta} \\ \ddot{\delta} \end{bmatrix}
=
\begin{bmatrix}
\dfrac{Z_\alpha}{mu} + \dfrac{M_\alpha Z_q}{I_y Z_\alpha} & \dfrac{Z_\alpha}{m} + \dfrac{M_q Z_q}{I_y m} - \dfrac{M_\alpha Z_q^2}{m I_y Z_\alpha} & -\dfrac{M_\alpha Z_\delta Z_q}{m I_y Z_\alpha} + \dfrac{M_\delta Z_q}{m I_y} & \dfrac{Z_\delta}{m} \\
\dfrac{M_\alpha m}{I_y Z_\alpha} & \dfrac{M_q}{I_y} - \dfrac{M_\alpha Z_q}{I_y Z_\alpha} & \dfrac{M_\delta}{I_y} - \dfrac{M_\alpha Z_\delta}{I_y Z_\alpha} & 0 \\
0 & 0 & 0 & 1 \\
0 & 0 & -\omega_n^2 & -2\zeta\omega_n
\end{bmatrix}
\begin{bmatrix} a_z \\ q \\ \delta \\ \dot{\delta} \end{bmatrix}
+
\begin{bmatrix} 0 \\ 0 \\ 0 \\ \omega_n^2 \end{bmatrix} \delta_e
$$

$$
+ \begin{bmatrix}
-\dfrac{Z_q M_\alpha Z_0}{m I_y Z_\alpha} + \dfrac{M_0 Z_q}{m I_y} \\
-\dfrac{M_\alpha Z_0}{I_y Z_\alpha} + \dfrac{M_0}{I_y} \\
0 \\
0
\end{bmatrix} \tag{5.23}
$$

Note that above state space representation is in the following form:

$$\dot{x} = Ax + Bu$$

5.3. Design of the Controllers

The state space representation found in Eqn. (5.23) will be used to design climb, acceleration and altitude hold autopilots in this section. In addition, a simple velocity hold algorithm will be explained at the end. For the preliminary design phase, disturbance matrix in Eqn. (5.23) will not be included during linear autopilot design.

In this thesis, it is essential that the recommendations of military standards "MIL-STD-1797" are followed for fixed-wing aircraft (MIL-STD-1797, 1997). The standards specify the acceptability of the response of the aerial vehicle to input and atmospheric gusts. The short-period mode is characterized by a damping ratio and natural frequency. For an aerial vehicle at any flight phase, determined values of damping ratio for Level 1 (i.e. very comfortable) are indicated in Table 5.2 whose detail could be found in Sadraey's book (Sadraey, 2013).

Table 5.2 Short period damping ratio specification

Flight Phase	Minimum ξ	Maximum ξ
A	0.35	1.3
B	0.3	2
C	0.35	1.3

Furthermore, stability criteria ensure the robustness of the system when disturbances, modeling uncertainties and system time delays are present. Therefore, controllers are designed in consideration with stability criteria of gain, phase, and delay margins shown in Table 5.3.

Table 5.3 Recommended stability margins

	Stability Criteria
Gain margin	>6 dB
Phase margin	%60-%90
Delay margin	>20 ms

5.3.1. Attitude Hold Controller

The controller configuration in Figure 5.2 will be employed to control the attitude in the pitch plane. This controller uses pitch rate in the inner loop and pitch attitude in the outer loop and thus requires a rate gyro which is involved in the inertial measurement unit.

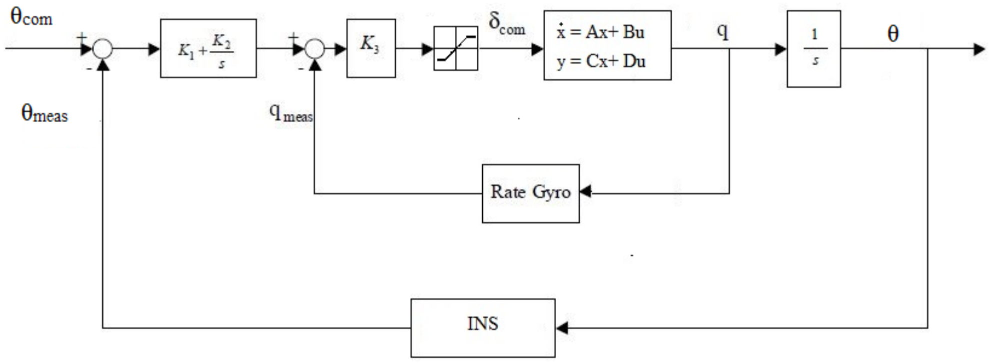

Figure 5.2 Attitude hold autopilot configuration

It performs proportional control in the inner loop as stability augmentation and proportional plus integral control in the outer loop similar to the design in Avcıoğlu's work (Avcıoğlu, 2000). Besides, the deflection of the elevator is restricted to $\delta_e = \pm 15\ deg$ as shown by a saturation block in Figure 5.2.

The selection of the controller gains will be executed for each flight speed and a constant altitude. However, only the design of the controller at the flight condition $V = 34\ m/s$ is going to be explained in detail here for the sake of simplicity. The natural frequency and damping ratio of the airframe without autopilot correction at each design point are given in Table 5.4

Table 5.4 Original characteristics of the airframe

	Design Point 1 $\boldsymbol{V = 17\ m/s}$	**Design Point 2** $\boldsymbol{V = 34\ m/s}$	**Design Point 3** $\boldsymbol{V = 51\ m/s}$
ξ	0.156	0.152	0.151
w_n (rad/s)	8.09	16.30	24.64

The desired pole locations are proposed by autopilot design requirements which are the autopilot natural frequency (outer loop bandwidth) and the damping ratio. The dominant poles close to origin determines the controller response. Therefore, control actuator poles are placed far away from the origin in order not to disturb system response.

Next, inner loop pitch rate gain K_3 is determined to improve damping characteristics of the stability augmentation and the desired damping ratio is $\xi = 0.7$ whilst assuring stability margins in Table 5.3. The inner loop root locus for the pitch attitude hold autopilot is shown in Figure 5.3. The figure illustrates the change in pole locations with respect to inner loop gain.

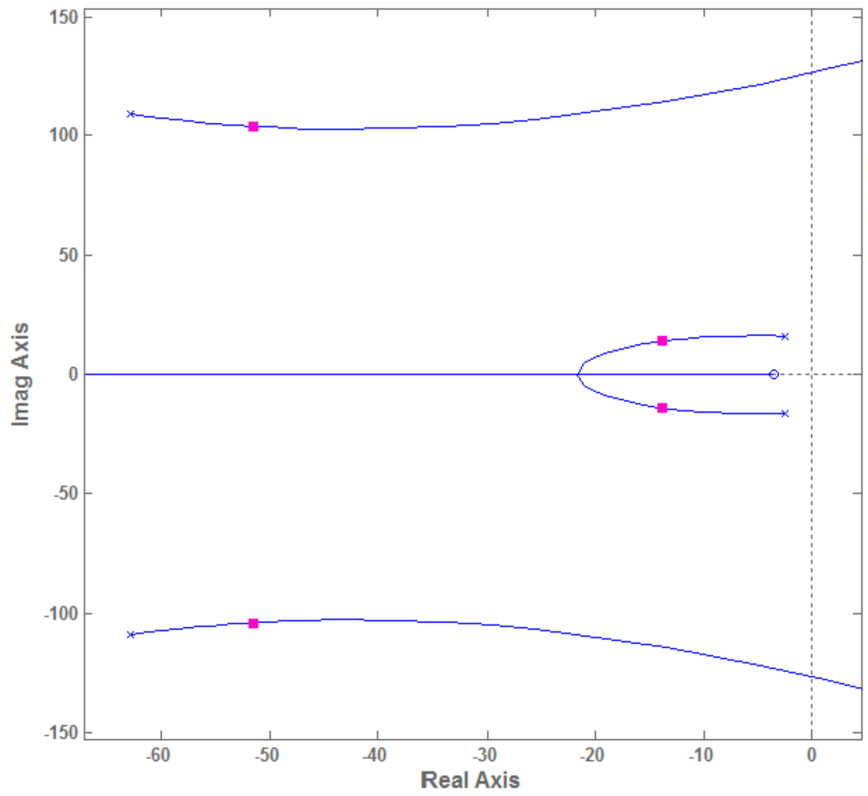

Figure 5.3 Inner loop root locus of the pitch attitude autopilot for design point 2

Then, outer loop proportional and integral gains are determined. While selecting the controller gains, the following requirements will be imposed on system response:

- Maximum percent overshoot < 20%
- Rise time is going to be small as possible whilst assuring stability margin requirements

While designing the outer loop controller proportional plus integral control is preferred even though the system is already Type 1. It is done due to improving system response characteristics. There is one dominant pole without an integral controller which alters system response rather than second-order response. Figure 5.4 illustrates the change in pole locations with respect to outer loop gains with a proportional plus integral controller.

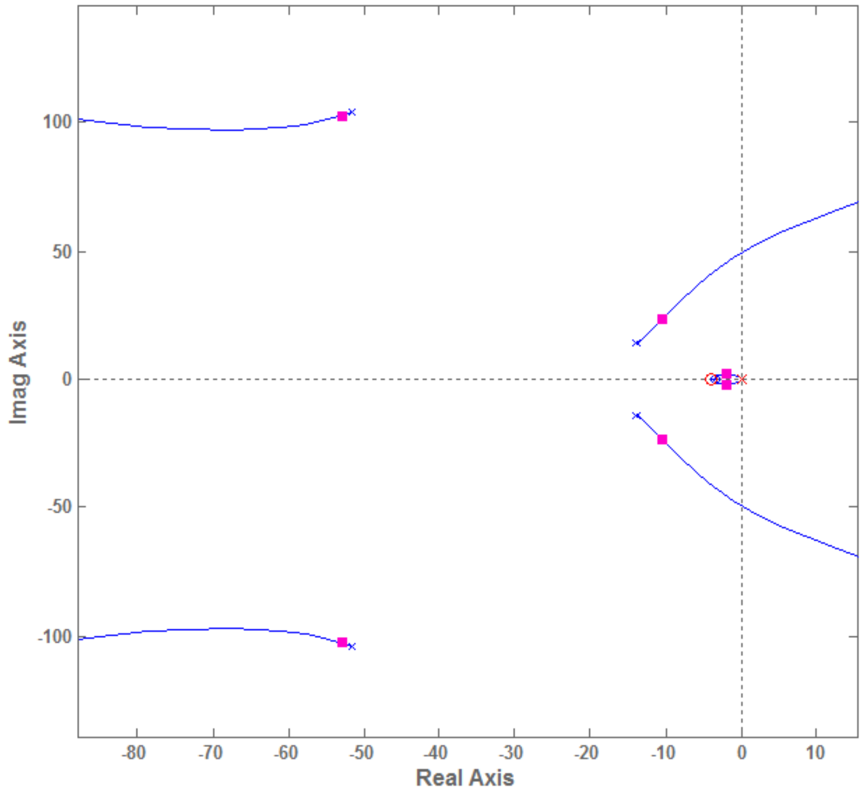

Figure 5.4 Outer loop root locus of the pitch attitude autopilot for design point 2

The response of the pitch hold autopilot obtained for pitch angle step input command at design point 2 is given in Figure 5.5. The time response characteristics such as the rise time, settling time, steady state error can be determined from Figure 5.5.

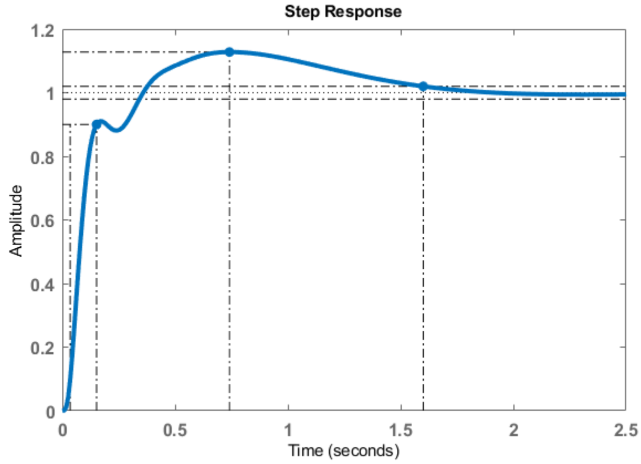

Figure 5.5 Autopilot Response to step pitch angle command at design point 2

The variation of UAV's autopilot natural frequency, damping ratio, stability margins and time response characteristics in the presence of the autopilot for all design points are illustrated in Table 5.5.

Table 5.5 System response and stability characteristics for design points

	Design Point 1	**Design Point 2**	**Design Point 3**
Autopilot natural frequency (rad/s)	1.84	2.81	3.31
Autopilot damping ratio	0.70	0.70	0.70
Rise time (s)	0.26	0.12	0.10
Settling time (s) (%2 criterion)	2.51	1.60	1.36
Maximum overshoot (%)	16.50	12.80	12.20
Gain margin (dB)	23.80	15.60	11.60
Phase margin (deg)	74.90	88.00	97.7
Delay margin (ms)	320	134	111

5.3.2. Normal Acceleration Autopilot

The altitude hold autopilot involves normal acceleration autopilot in the inner loop. The controller configuration in will be employed to control normal acceleration. This controller uses pitch rate and normal acceleration in the inner loop as stability augmentation and normal acceleration in the outer loop. The integral control in the outer loop is necessary to prevent steady-state error in the response.

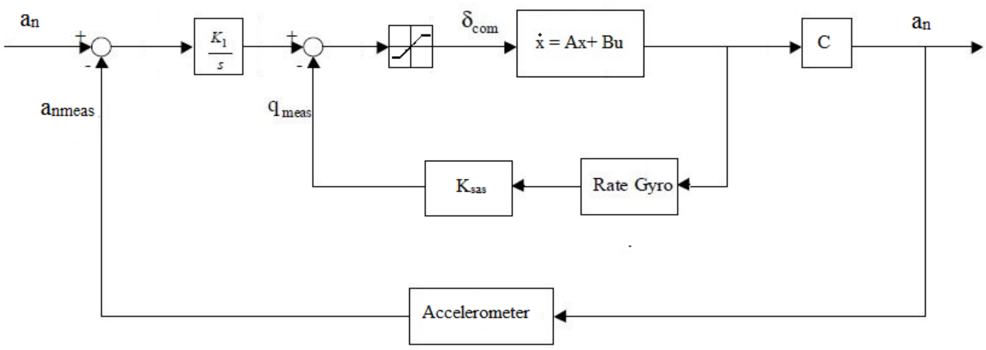

Figure 5.6 Normal acceleration autopilot configuration

The stability augmentation, the inner loop, is designed to provide adequate damping characteristics as usual and the desired damping ratio is $\xi = 0.7$. A significant note here is that there is no position or angular rate information provided by the control actuator system. Therefore, only corresponding gains of normal acceleration and pitch rate are used while objective damping characteristics are assured. The closed loop characteristics of the stability augmentation system (SAS) are given in Table 5.6.

Table 5.6 Closed inner loop characteristic of SAS

	$\boldsymbol{V = 17\ m/s}$	$\boldsymbol{V = 34\ m/s}$	$\boldsymbol{V = 51\ m/s}$
w_n (rad/s)	8.06	16.15	24.06
ξ	0.68	0.70	0.71

The gains of integral controller are also selected based on the stability margins and handling qualities.

5.3.3. Altitude Hold Autopilot

Altitude hold controllers mostly form the outermost loop in the flight control algorithms. Also, the inner loop holds SAS or special autopilot configurations. The altitude hold autopilot configuration in Figure 5.7 will be used to sustain UAV'S altitude. A similar autopilot is also employed to maintain the altitude of the sea skimming missile design in Avcıoğlu's research (Avcıoğlu, 2000).

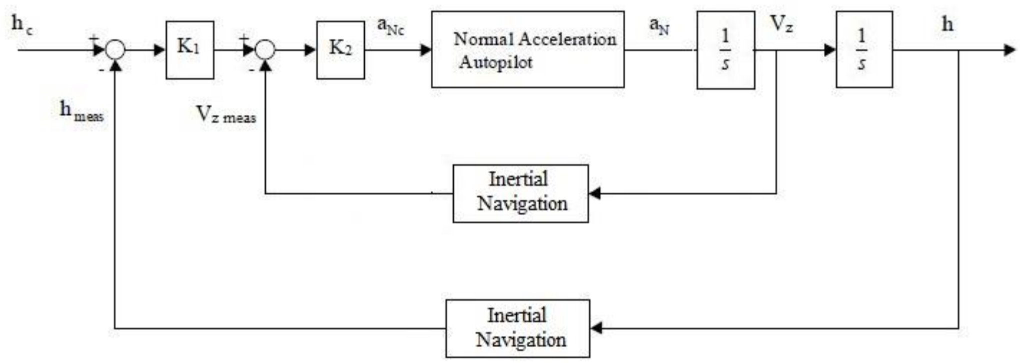

Figure 5.7 Altitude hold autopilot configuration (Avcıoğlu, 2000)

The normal acceleration autopilot is already designed in the previous section and illustrated as closed loop transfer function in Figure 5.7. The demanding part in designing the altitude hold autopilot is to prevent high oscillations in the altitude. It might be the case in the war field that high oscillation in altitude response could cause the loss of the UAV due to detection by the enemies or flying close to ground surface. Therefore, following design requirements will be imposed on the design of the controllers:

- Maximum percent overshoot < 5%
- Rise time minimum as possible while assuring stability margins

After specifying the autopilot design requirements, the controller gains shall be determined via root locus analysis as in Figure 5.8 and Figure 5.9.

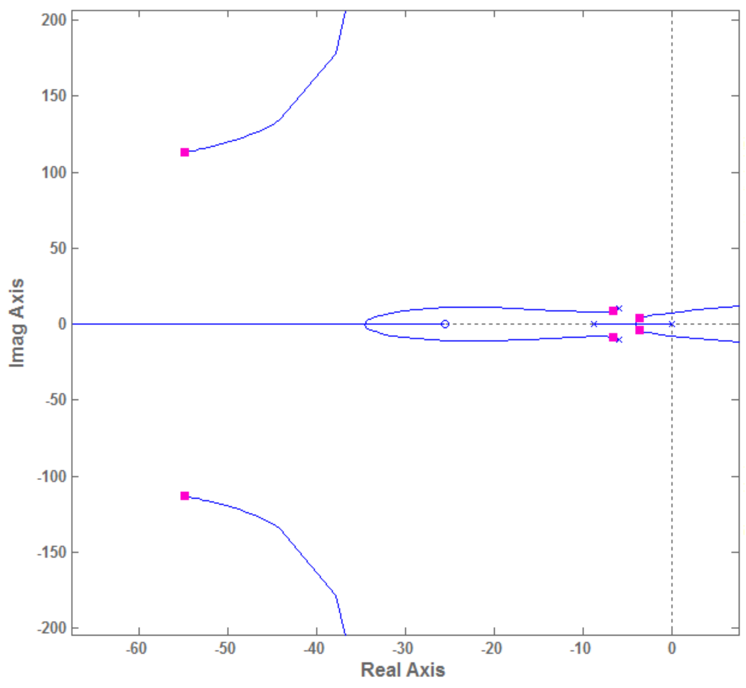

Figure 5.8 Inner loop root locus of the altitude hold autopilot for design point 2

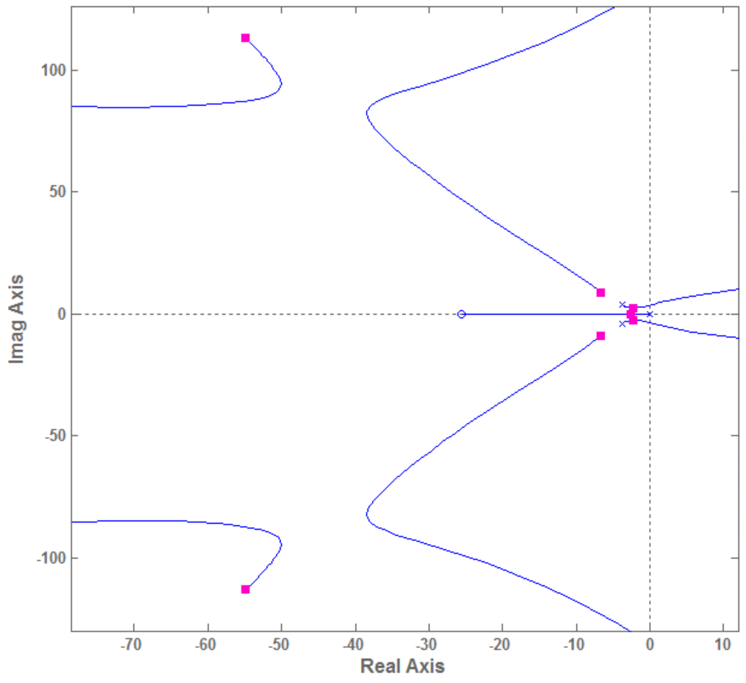

Figure 5.9 Outer loop root locus of the altitude hold autopilot for design point 2

The response of the altitude hold autopilot obtained for 1 m step input command at design point 2 is given in Figure 5.10.

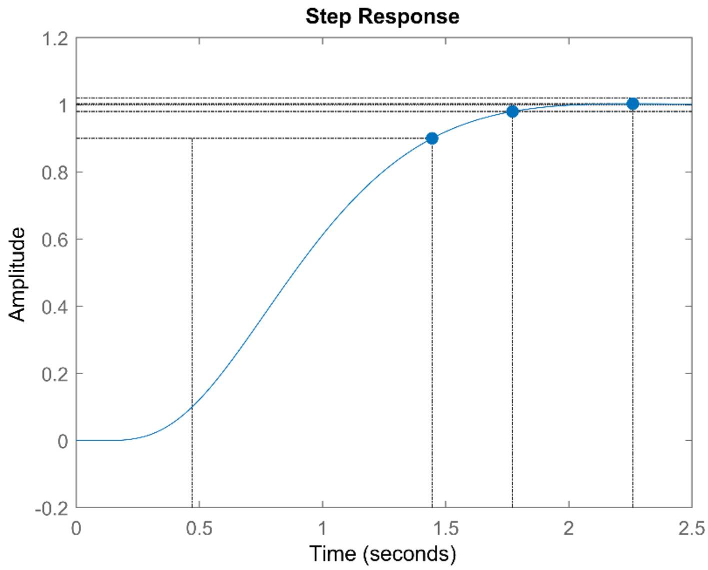

Figure 5.10 Autopilot Response to step altitude command at design point 2

The time response characteristics such as the rise time, settling time, and steady-state error can be determined from Figure 5.10. It is observed from the figure that altitude first decreases in the reverse direction. This reverse behavior is caused by the aerodynamic force generated due to the deflection of the control surface. As soon as the UAV starts to gain acceleration, the reverse aerodynamic force is compensated by the wing-body lift. The variation of UAV’s autopilot natural frequency, damping ratio, stability margins and time response characteristics in the presence of the autopilot for all design points are illustrated in Table 5.7.

Table 5.7 System response and stability characteristics for design points

	Design Point 1	**Design Point 2**	**Design Point 3**
Autopilot natural frequency (rad/s)	1.58	3.32	4.86
Autopilot damping ratio	0.7	0.7	0.7
Rise time (s)	2.93	0.98	0.63
Settling time (s) (%2 criterion)	6.03	1.77	1.14
Maximum overshoot (%)	≈0	≈0	≈0
Gain margin (dB)	13.0	11.2	10.9
Phase margin (deg)	69.6	65.6	64.9
Delay margin (s)	2.91	1.05	0.69

5.3.4. Velocity Control

In order to sustain desired flight speed, simple velocity controller is used. The velocity control configuration in Figure 5.11will be employed.

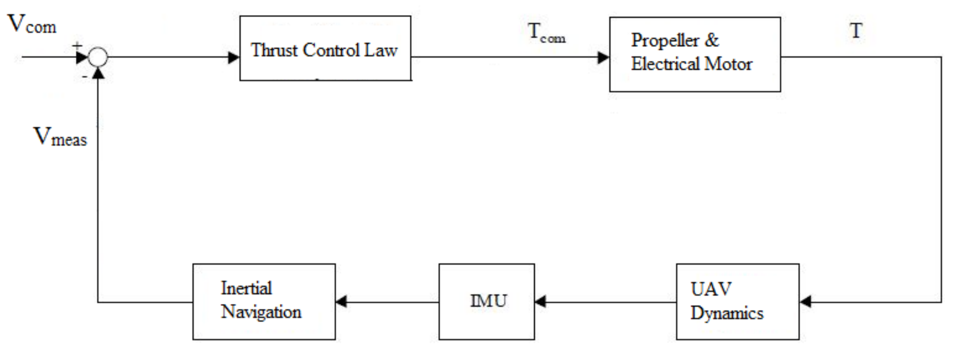

Figure 5.11 Velocity control configuration

For the preliminary design analysis, the electric motor is assumed to be capable of changing thrust at a rate of 5N/s. However, the thrust control command at this rate is only imposed when there is more than 10% error between the velocity command and velocity measured. In between, a quadratic function is used in the following manner:

$$T_{com(i+1)} = T_{com(i)} + K\Delta t \tag{5.24}$$

Where K: $thrust\ increment\ rate$

Thus, thrust increment rate is defined in Eqn. (5.25):

$$\begin{aligned}
&Mach_{meas} * 1.1 < Mach_{des} && \rightarrow K = 5N/s \\
&Mach_{des} * 0.9 < Mach_{meas} < Mach_{des} * 1.1 && \rightarrow K = \text{sign}(\Delta\text{V})\Delta\text{V}^2\, 480,000 \\
&Mach_{des} * 1.1 < Mach_{meas} && \rightarrow K = -5N/s
\end{aligned} \tag{5.25}$$

The reason why a quadratic function is preferred rather than a linear equation is that linear thrust control gain causes high oscillations in the velocity profile. On the other hand, the quadratic function provides a smoother velocity response and less oscillation. In addition, both lower and upper limits are imposed on thrust command considering electric motor’s thrust available value.

5.4. Flight Simulation Analysis

Gain scheduled controller coefficients are embedded in 3 degrees of freedom flight simulation. The simulation involves the nonlinear aerodynamic database from CFD results, an inertial navigation system, flight mechanics, environment, and gravity models. The motion of the UAV is restricted in the longitudinal plane.

Firstly, the performance of the pitch attitude hold autopilot is tested. The scenario tested in the flight simulation model is to command system with step inputs having different magnitudes of pitch angle throughout the flight.

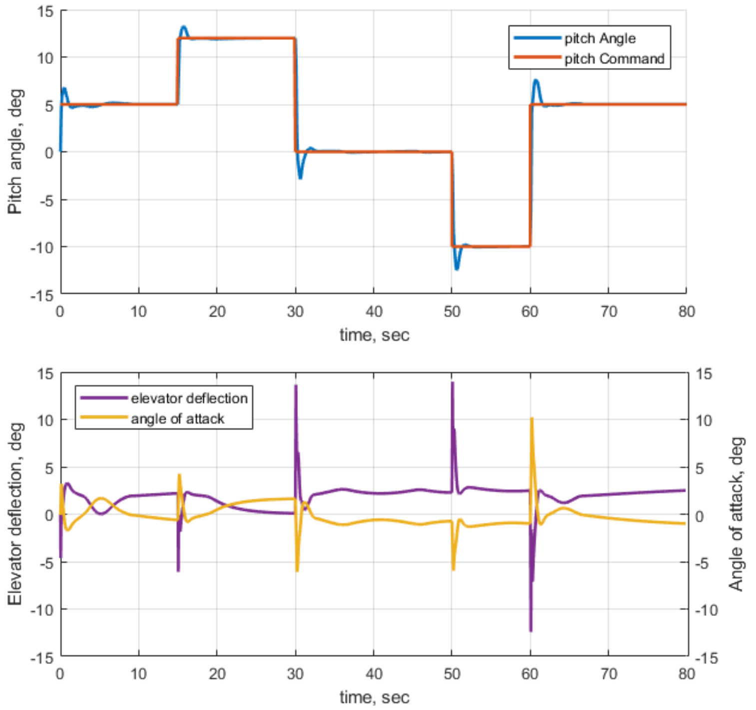

Figure 5.12 Flight simulation command-response plots

It can be proven from Figure 5.12 that the designed autopilot can perform the pitch command successfully. While realizing pitch attitude command, angle of attack and elevator deflections also stay in the linear aerodynamics region. Therefore, it can be stated that the assumptions made during autopilot design studies are validated via flight simulation.

Next, the performance of the altitude hold autopilot is tested in flight simulation. The guidance algorithm switches between attitude hold and altitude hold autopilots upon reaching 5% to the desired altitude. The climb to the desired altitude is realized and restricted by $\theta_{com} = 12\ deg$ command and descent to the desired altitude is performed by $\theta_{com} = -10\ deg$ while deflection of the elevator is restricted to $\delta_e = \pm 15\ deg$. The scenario tested in the flight simulation model is to command system with step inputs having different magnitudes of altitude throughout the flight.

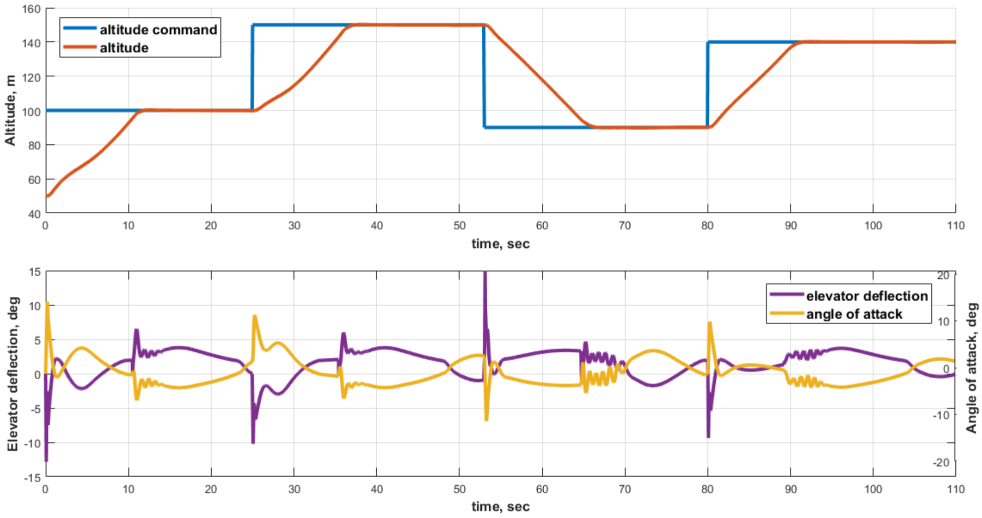

Figure 5.13 Flight simulation command-response plots

Figure 5.13 illustrates that the designed controllers can achieve the given altitude commands within the linear aerodynamics region. The designed tandem wing UAV, in terms of aerodynamics and control systems, can perform mission requirements and assumptions made in the controller design section are validated. It is also proved that aircraft stayed in the linear aerodynamic envelop in its flight regime so that autopilots could perform well. In addition, the history of the pitch attitude while performing above altitude hold trajectories is shown in Figure 5.14.

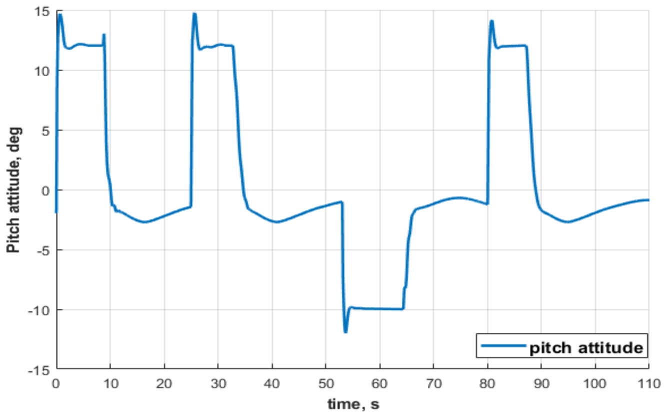

Figure 5.14 The history of pitch attide while performing the mission

CHAPTER 6

MONTE CARLO ANALYSIS

6.1. Introduction

The definition of aircraft stability is of the tendency of an aircraft to return to the original trim conditions if disturbed by an undesired force or moment. Therefore, uncertainties, biases, and atmospheric conditions are randomly assigned and modeled with Monte-Carlo analysis to test the robustness and stability of the designed autopilots and whether designed controllers are still capable of fulfilling mission requirements. Monte Carlo analysis is performed to understand the impact of various uncertainties on the system and to conclude statistical results.

6.2. Monte Carlo Design Space

While the uncertainties are assigned randomly, the normal probability distribution is preferred. In a normal distribution, the events which are true by 68% are considered as 1σ whilst the events which are true by 99.7% are considered as 3σ .In other words, sigma values represent the standard deviation of the mean and the percentages show the band around the mean as shown in Figure 6.1. The uncertainties in the Monte Carlo analysis will be assigned within 3σ.values.

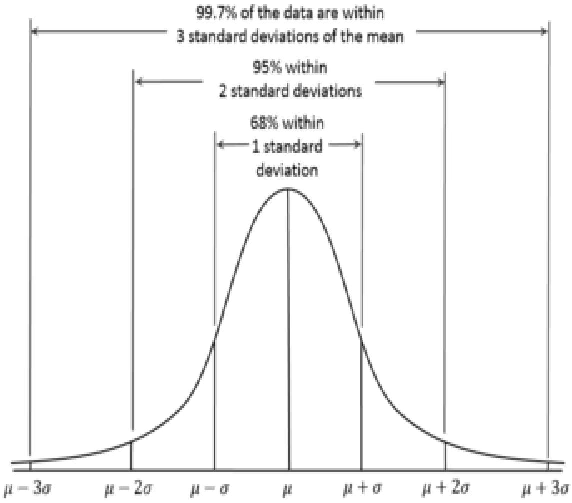

Figure 6.1 Normal probability distribution (no date, Retrieved from Wikipedia)

The uncertainties, bias values, and atmospheric conditions that are tested in Monte Carlo simulation are given in Table 6.1

Table 6.1 Monte Carlo analysis uncertainty space

Variable name	Mean value	3σ value
Wind Velocity, m/s	10	2.5
Wind Direction, deg	45	15
Takeoff weight, kg	4.4	0.1
Cg location, mm	369	50
Aerodynamic uncertainty in C_l, C_d, C_m, %	0	5
Elevator position bias, deg	0	1

6.3. Monte Carlo Simulation Results

After the Monte Carlo design space is defined, 500 Monte Carlo simulation runs are conducted. The resultant trajectories of the Monte Carlo simulation are shown in Figure 6.2. For all simulation runs, the continuous wind starts at the beginning of the flight.

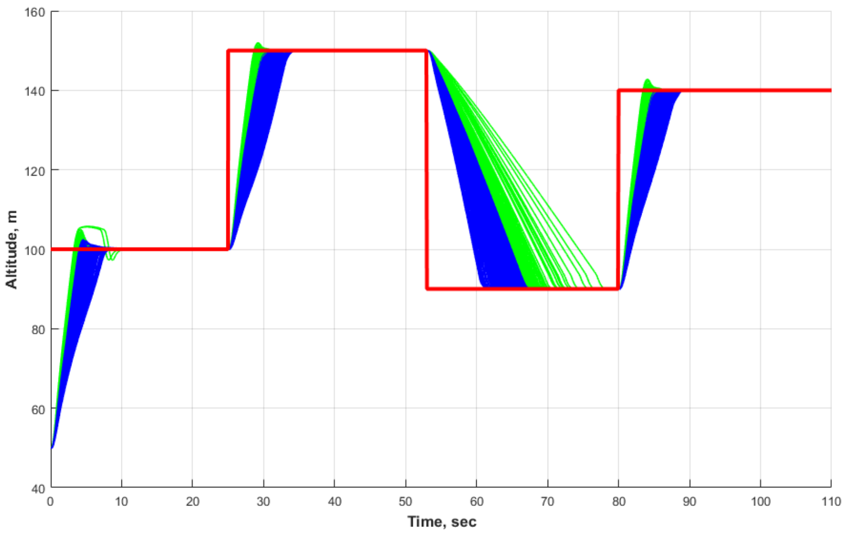

Figure 6.2 Monte Carlo simulation trajectory results

It is observed that UAV can still achieve the mission requirements under disruptive effects. In Figure 6.2, some trajectories are colored in green which corresponds to the worst-case scenarios. These green trajectories correspond to scenarios where wind direction is steeper (close to 60 degrees), the magnitude of the wind is close 12.5 m/s. Thus, the designed UAV system is more vulnerable to atmospheric conditions rather than model uncertainties and system biases. In other words, the performance of the UAV decays with severe wind conditions. During climbing to objective altitude overshoot occurs and decent to certain altitude takes longer time under heavy wind disturbances. On the other hand, the tandem wing UAV can successfully hold the altitude under uncertainties and atmospheric disturbances thanks to its robustness. To wrap up, results are acceptable and the operator of the tandem wing UAV should be aware of the degradation of performance under heavy wind conditions.

CHAPTER 7

CONCLUSIONS & FUTURE WORK

7.1. Conclusions & Future Work

This research illustrates that nonplanar wing configuration, tandem wing design, can meet the mission requirements. The conceptual design process for the monoplane configuration resulted in unsatisfactory conditions. However, tandem wing design could meet the requirements by taking advantage of the slotted wing effect. It is proven that the slotted wing effect affects the interference between two wings in the favor of the aerodynamic performance. The improvement of the lift is found to be around 23% at high angles of attack. This phenomenon is shown to be a worthy alternative solution, where there is a need for high lift due to geometric restrictions.

The dynamic model of UAV and controller design completes the aerodynamic design process. In this research, the connection between two separate disciplines, i.e. aerodynamics and flight control, is emphasized. The aerodynamic configuration is overseen by stability and control characteristics. In Chapter 5, pitch attitude hold and altitude hold controllers are designed. The robustness of the controllers is ensured by gain, phase and, delay margins. Then, the nonlinear aerodynamic database and linear controllers are implemented into flight simulation to test the performance of the design. In Chapter 6, the Monte Carlo analysis reveals that the designed system is more prone to athmospheric disturbances rather than model uncertainities. Degradation of performance occurs under heavy wind conditions.

This research provides a guideline for the conceptual design of a UAV. The aerodynamic and stability/control aspects are shown to be inseparable. Tandem wing design encourages future work in order to understand the effect of the vertical position of two wings and effect of various flight speeds on the slotted wing effect. The structural aspects of the tandem wing design should also be analyzed since this study consider the tandem wing UAV as a rigid body. Wing folding mechanism and wing attachment to fuselage are highly critical due to aeroelastic effects and should be handeled carefully. Furthermore, lateral and directional dynamics of the tandem wing design are also considered as a topic of future research. The controller design for each channel can be performed and six degree of freedom flight simulation can be generated to obtain complete system model.

REFERENCES

Aftab, S., Rafie, A. M., Razak, N., & Ahmad, K. (2016). Turbulence Model Selection for Low Reynolds. *PLOS ONE, 11*(4). doi:10.1371/journal.pone.0153755

Anderson, J. D. (1999). *Aircraft Performance and Design.* Boston: The McGraw-Hill Companies, Inc.

Avcıoğlu, H. T. (2000, September). *A TOOL FOR TRAJECTORY PLANNING AND PERFORMANCE.* Ankara: Middle East Techical University.

Aviation Blog. (2016). *The jets of the future*. https://www.aerotime.aero/aviation.blog/23048-the-future-aircraft. adresinden alındı

Barton, J. D. (2012). Fundamentals of Small Unmanned Aircraft Flight. *John Hopkins Apl Techincal Digest, 31*(2).

Beard, R. W., & McLain, T. W. (2012). *Small unmanned aircraft: Theory and practice.* Princeton, NJ: Princeton University Press.

Brinkworh, B. J. (2016). On the aerodynamics of the Miles Libellula tandem-wing aircraft concept, 1941 – 1947. *Jorunal of Aeronautical History*.

Devore, J. L. (1995). *Probability and statistics for engineering and the science.* Belmont: Duxbury.

Doosttalab, A., Mohammadi, M., Doostalab, M., & Ali., A. (2012). NUMERICAL INVESTIGATION OF AERODYNAMICAL PERFORMANCE OF DAMAGED LOW-REYNOLDS AIRFOILS FOR UAV APPLICATION. *TFAWS.*

Eisenbeiss, H. (2004, November). A MINI UNMANNED AERIAL VEHICLE (UAV): SYSTEM OVERVIEW. *International workshop on PROCESSING AND VISUALIZATION USING HIGH-RESOLUTION IMAGERY*.

Gur, O., & Rosen, A. (2009, July-August). Optimizing Electric Propulsion Systems. *Journal of Aircraft, Vol. 46*(4). doi:10.2514/1.41027

Imam, A., & Bicker, R. (2014). Design and Construction of a Small-scale Rotorcraft UAV System. *International Journal of Engineering Science and Innovative Technology, 3*(1).

Kroo, I. (2005). Nonplanar Wing Concepts for Increased Aircraft Efficency . *VKI lecture serios on Innovative Configurations and Advanced Concepts for Futre Civil Aircraft*.

Landolfo, G. (2008). *Aerodynamc and Structural Design of a Small Nonplanar Wing UAV.* Ohio: University of Dayton.

Linden, D., & Reddy, T. B. (2002). *Handbook of Batteries.* New York: McGraw-Hill.

Mignet, H. (1934). *LE SPORT DE L'AIR.* Paris, Taffin-Lefort.

MIL-STD-1797. (1997). *Flying Qualites of Piloted Aircraft.* Washington, DC.: Department of Defense.

Nelson, C. R. (1989). *Flight Stability and Automatic Control.* USA: McGraw-Hill, Inc.

Ogata, K. (2010). *Modern Control Engineering.* New Jersey: Pearson Education, Inc.

Ostowari, C., & Naik, D. (1985). *Post-Stall Wind Tunnel.* Colorado: Rockwell International Corp.

Padmaraja, Y. (2003). *Brushless DC Motor Fundamentals.* U.S.A: Microchip Technology Incorparated.

Raymer, D. P. (1992). *Aircraft Design: A Conceptual Approach* (Second Edition b.). Washington, DC: American Institute of Aeronautics and Astronautics.

Sadraey, M. H. (2013). *Aircrafy Design a Systems Engineering Approach.* Chichester: John Wiley & Sons.

Selig, M. S., & Guglielmo, J. J. (1997). High-Lift Low Reynolds Number Airfoil Design. *Journal of Aircraft, 34*(1).

Skrzypietz, T. (2012). *Unmanned Aircraft Systems for Civilian Missions.* Brandenburg Institute for Society and Security.

Slater, A. E. (1962). *Sailplane and Gliding.* London, England: British Gliding Association.

Song, X.-w., Zhang, M.-x., & Lin, P.-z. (2017). Skin Friction Reduction Characteristics of Nonsmooth. *Hindawi Mathematical Problems in Engineering*.

Torun, E. (1999, April). UAV Requirements and Design Consideration. *Advances in Vehicle Systems Concepts and Integration*.

APPENDICES

A. Aerodynamic Coefficients of the Alternative Tandem Wing Configurations

Numerical analysis is performed for the UAV having rear wing $AR = 6$ and $AR = 7$ for various angle of attack values. The plots of drag coefficient, lift coefficient and pitching moment coefficient at the center of gravity of the aircraft for 6 different aircraft configurations with respect to Table 4.2 having rear wing $AR = 6$ are shown in A 1, A 2, and A 3, respectively.

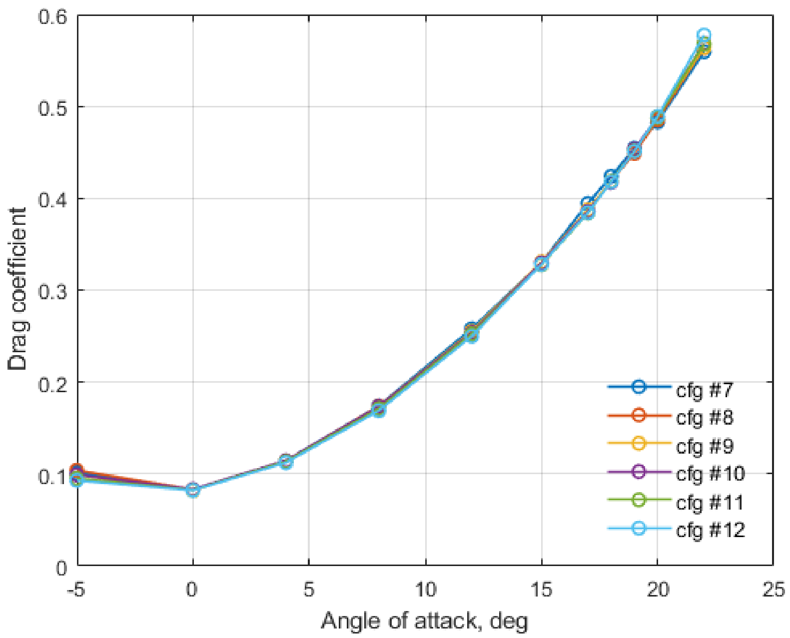

A 1 Drag coefficients for 6 different UAV having rear wing AR = 6

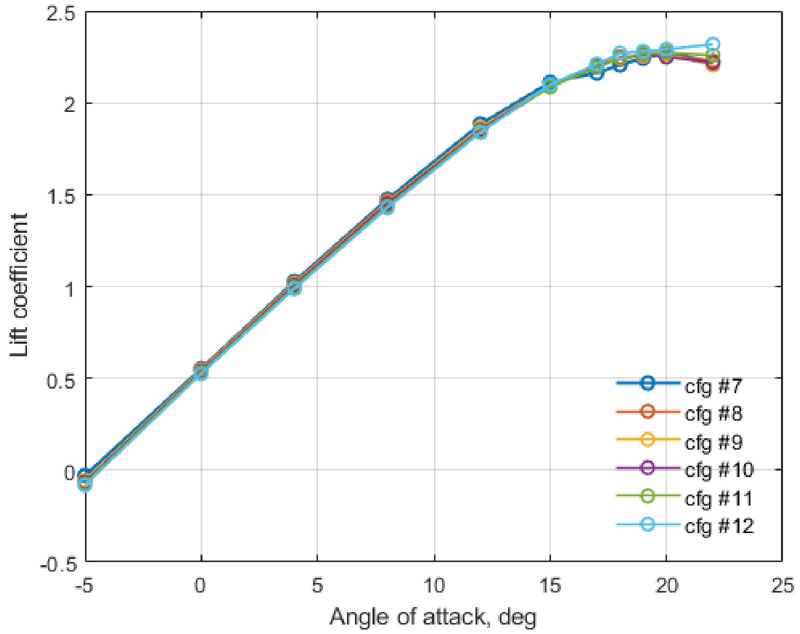

A 2 Lift coefficients for 6 different UAV having rear wing AR = 6

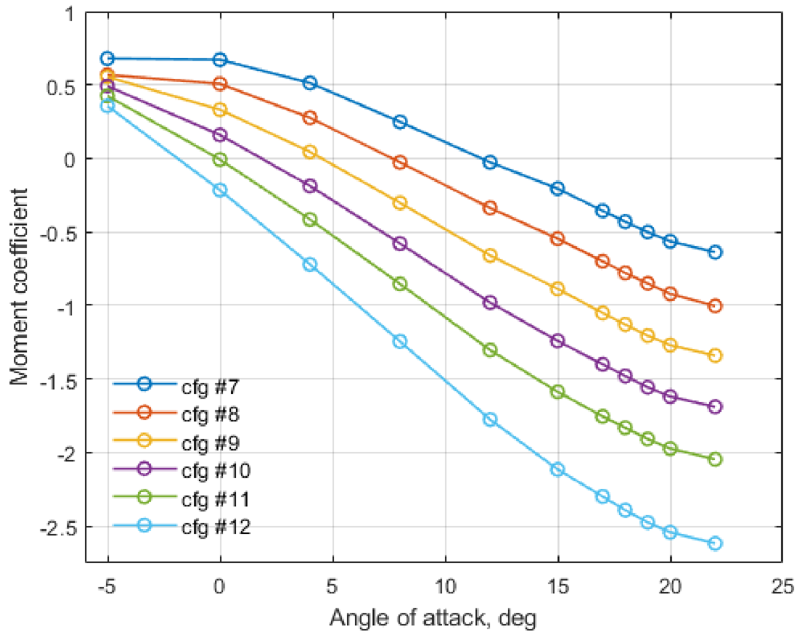

A 3 Moment coefficients for 6 different UAV at center of gravity having rear wing AR =6

The plots of drag coefficient, lift coefficient and pitching moment coefficient at the center of gravity of the aircraft for 6 different aircraft with respect to Table 4.2 configurations having rear wing $AR = 7$ are shown in A 4, A 5, and A 6, respectively.

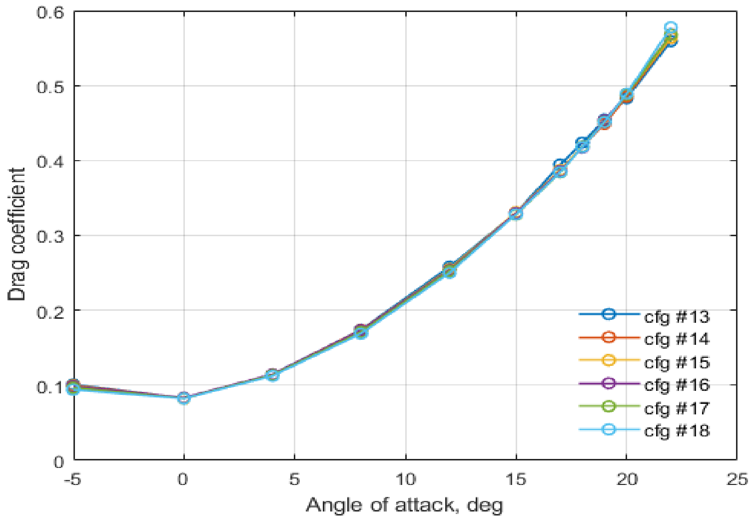

A 4 Drag coefficients for 6 different UAV having rear wing AR = 7

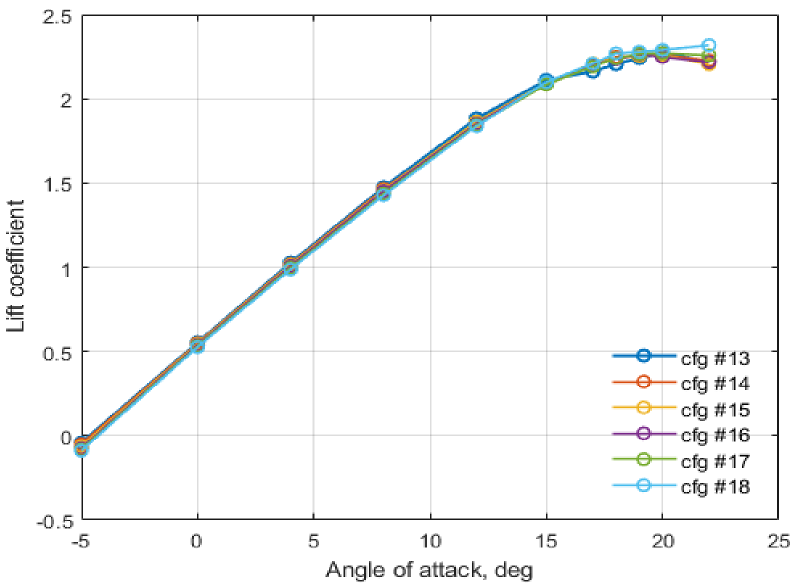

A 5 Lift coefficients for 6 different UAV having rear wing AR = 7

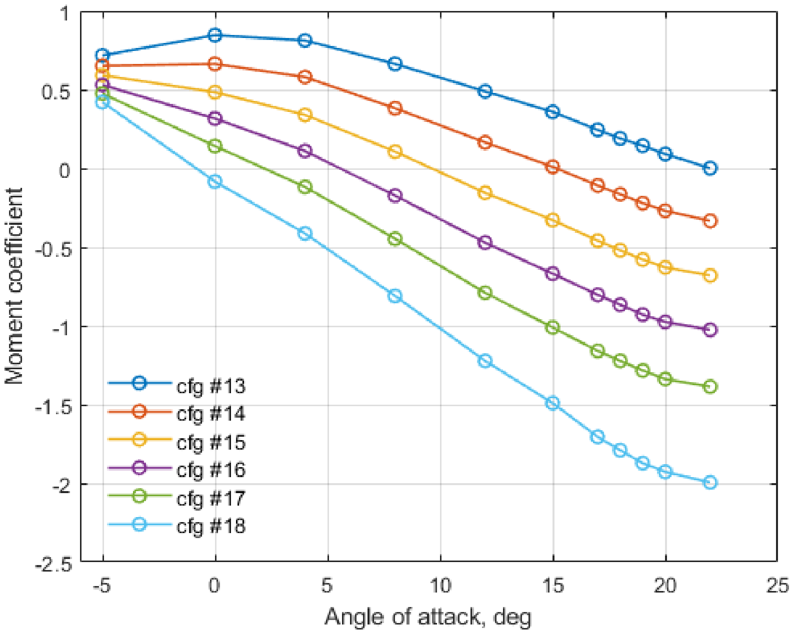

A 6 Moment coefficients for 6 different UAV at center of gravity having rear wing AR = 7